LOCKHEED

MISSILES & SPACE COMPANY, INC • SUNNYVALE, CALIFORNIA

SYSTEMS LEVEL FEASIBILITY STUDY FOR THE DETECTION OF EXTRA-SOLAR PLANETS

Volume 1

INFRARED INTERFEROMETER

(IRIS)

LMSC-D676424

June 1979

Prepared for the

NATIONAL AERONAUTICS AND SPACE ADMINISTRATION
Ames Research Center
Under Contrace NAS2-10030

LOCKHEED PALO ALTO RESEARCH LABORATORY
LOCKHEED MISSILES & SPACE COMPANY, INC
A SUBSIDIARY OF LOCKHEED AIRCRAFT CORPORATION

FOREWORD

This report is submitted by Lockheed Missiles and Space Company, Inc. to the National Aeronautics and Space Administration, Ames Research Laboratories, Mountain View, California, as partial fulfillment of Contract NAS2-10030, "Systems Level Feasibility Study For the Detection of Extra-Solar Planets". The report is submitted in two volumes:

Volume 1: Spinning Interferometer (IRIS) known as the Stanford Concept

Volume 2: Apodized Telescope (APOTS) known as the Hewlett-Packard Concept

PRECEDING PAGE BLANK NOT FILMED

ABSTRACT

A sensor system for the direct detection of extra-solar planets from an earth orbit is evaluated: a spinning, infrared interferometer (IRIS). It is shuttle-deployed, free-flying, requires no on-orbit assembly and no re-servicing over a design-life of five years.

The sensor concept and the mission objectives are reviewed, and the performance characteristics of a baseline sensor for standard observation conditions are derived. Key performance requirements are examined and technology hurdles identified. A baseline sensor design is given and the enabling technology discussed. Cost and weight estimates are performed; and a schedule for an IRIS program including technology development and assessment of risk are given. Finally, the sensor is compared with the apodized visual telescope sensor (APOTS) proposed for the same mission.

The major conclusions are: that with moderate to strong technology advances, particularly in the fields of long-life cryogenics, dynamical control, mirror manufacturing, and optical alignment, the detection of a Jupiter-like planet around a Sunlike star at a distance of 30 light-years is feasible, with a 3-meter aperture and an observation time of 1 hour. By contrast, major and possibly unlikely breakthroughs in mirror technology are required for APOTS to match this performance.

TABLE OF CONTENTS

TABLE OF CONTENTS (CONTD)

TABLES

LIST OF FIGURES

List of Often Used Symbols

(Meaning unless otherwise specified in text)

B	stellar brightness
b	interferometer baseline (aperture separation)
c	speed of light
D	diameter of primary mirrors
d	distance to star
F	spectral irradiance (photons/m^2. sec.μm)
h	Planck's constant
I	spectral radiance (photons/m^2. sec.μm.Sr)
J_m	Bessel function of integer order m
J'_m	first derivative of J_m
J''_m	second derivative of J_m
K	degrees Kelvin
k	Boltzmann 's constant
M	absolute magnitude
m	apparent magnitude index
P	probability
p	subscript: planet
Q	number of time bins per interferometer period τ
q	order of time bin $(1 \leq q \leq Q)$
R	radius
s	subscript: star
T	temperature optical transmission
t	time
z	subscript: zodiacal light
α	orientation angle of interferometer baseline
δ	planet's orbit radius
Δ	total position error

List of Often Used Symbols (Cont'd)

$\Delta\phi$	error in ϕ
ϵ	emissivity
θ	star-planet angular separation
λ	wavelength
μ	micro- (10^{-6})
ρ	photon rate to Airy disk (photons/sec μm)
σ	standard deviation surface roughness
τ	period of rotation of interferometer
ϕ	azimuthal coordinate (of planet)
φ	$[\exp(hc/\lambda kT) - 1]^{-1}$
χ	defined in text
ω	angular frequency of rotation of interferometer $(=2\pi/\tau)$

ACQ	acquisition
ACS	attitude control systems
CDR	critical design review
ELS	eastern launch site (Cape Canavaral)
FDR	final design review
G/e	graphite-epoxy
IR	infrared
IUS	interim upper stage
ℓ He	liquid helium
LV	launch vehicle
MLI	multi-layered insulation
N.A.	not applicable
OA	optical axis
OTA	optical telescope assembly
PDR	preliminary design review
RFQ	request for acquisition
ROM	rough order of magnitude

List of Often Used Symbols (Cont'd)

SAA	South Atlantic anomaly
SC	spacecraft
S/N	signal-to-noise ratio
SSM	systems service module
ST	space telescope
ULE	ultra low expansion material
SCS	stallite control system

1. Introduction

1.1 Background

The question of whether or not our Solar System is unique, i.e. whether or not there are planets orbiting other stars, is of great interest to astronomers and philosophers alike. It has important bearings on questions about the origin of life (whose existence, to our present knowledge, is confined to this planet), about the solar system (whose origin is still hidden from us) and about the presence of other intelligence in the universe. The last is, for reasons of varying worth, one of the most thought-provoking questions of all.

The nearest stars are more than 4 light-years distant, which is more than 10^5 times the diameter of the earth's orbit. Any planet of theirs would be exceedingly faint and close to them, as seen from us. Consequently, it is very difficult to detect extra-solar planets. C. Huygens wrote in 1696:

".. the nature of the stars and the sun is the same ..... what is to prevent us from thinking that each of these stars has planets of its own ..... (but) it is utterly impossible that we should see (them) ... by reason of their faint luminosities and because all their orbits would appear to join with their sun in one and the same bright point." (Emphasis by this author) Huygens was understandably pessimistic, in view of the relatively primitive state of the astronomical instrumentation of his day. Today we believe, and it is shown in this report, that extrasolar planets of sufficiently close and bright stars can be detected directly. But the necessary technical and operational effort, let alone the cost, would have surely amazed Huygens!

Clearly, Huygens had <u>direct</u> detection of extrasolar planets in mind, that is: observing a planet by means of resolving its faint image from the bright parent star image. This report in fact concerns the feasibility of one approach to that problem. But another method of detection exists, and it has already been applied in the past from the ground, which is called <u>indirect detection</u>: that is, observing the parent star for small irregularities in its position and velocity in a fixed celestrial frame of reference, which could be due to the gravitational interaction with a planet of its own. This method requires the comparisons of precise position measurements (astrometry) of radial velocity measurements of the candidate star, with a careful analysis of those factors or

phenomena which introduce irregularities but have no connection to the star at all. Past searches for extra-solar planets of nearby stars have yielded inconclusive results. Some of the difficulties encountered in such searches are: comparing different photographic plates, finding proper reference systems, and eliminating the effects of the earth's atmosphere and motion on the observations. Nevertheless, these stars should be re-examined.

With direct methods one faces this problem: to resolve an extremely faint source (planet) in close angular separation from a bright source (parent star) against a strong background (zodiacal light). The solution of this problem requires instruments of ultra-high sensitivity, spatial resolution, background discrimination and pointing control. They must have large apertures and be space-based to eliminate the disturbing effects of the earth's atmosphere.

Direct and indirect methods are promising if re-examined in the light of recent advances in relevant technology areas. Therefore, as apart of its long-range program of searching for extra-terrestrial intelligence, NASA has formulated a definitive approach to detecting extra-solar planets. That approach, which is expected to yield conclusive results by the end of this century, was developed in several NASA-sponsored workshops and is outlined in Table 1-1.

This resport discusses a space-based direct detection system, in particular its performance characteristics, technology requirements, baseline design, cost and schedule. The system is an earth-orbiting infrared interferometer (IRIS). Also known as the Stanford Concept, it was proposed by Dr. R. N. Bracewell of Stanford University in collaboration with Dr. D. C. Black of NASA-Ames and Dr. R. McPhie of the University of Waterloo, Canada. As a result of a NASA-Ames Stanford University joint study effort, a report was published on the sensor under Contract NAC2-OR745-716. We shall make use of the major results in that study.

IRIS is compared to a second sensor system (discussed in Vol. 2 of this report): an apodized, visual telescope (APOTS) known as the Hewlett-Packard concept.

Table 1-1

STRATEGY FOR SEARCHING FOR EXTRA-SOLAR PLANETS

1. Objective:
   - PHASE I
     - A. Develop technology and undertake search for planets around stars within 30 parsecs (100 light-years).
     - B. Determine statistics of planetary systems.
   - PHASE II
     - C. Determine physical characteristics of specific systems.

2. Approach: Phase I provides a high-confidence data base for Phase II.
   - A. Ground-based radial velocity and astrometric observations of stars within 30 parsecs.
   - B. Design, build, launch and operate a direct detection system for a five-year mission.
   - C. Design, build, launch and operate a space-based astrometric interferometer.

3. Expected accomplishments:
   - A. Indirect methods: Mass, orbital parameters of planets.
   - B. Direct methods: Temperature, orbital period, orbital radius.

4. Immediate activities:
   - A. Ground-based observations.
   - B. Feasibility studies of space-based detection.

References:

"Rationale and a Preliminary Long-Range Strategy for Searching for Extra-Solar Planets", NASA-Ames Research Center, August 1977.

"Report of the Planetary Detection Workshops to the Office of Space Science of the National Aeronautics and Space Administration" (prepared by Jesse L. Greenstein and David C. Black).

The key study directives were, to assume

1) delivery of the sensor system to operational orbit by Shuttle (plus auxiliary engine, if necessary) using full STS capacity and requiring no assembly in space;

2) a five-year experiment life without re-servicing; and

3) optimization of the sensor system for the detection of a "standard" extra-solar planet, i.e. detection of Jupiter in the Jupiter-Sun system from a distance of 32 light-years.

1.2 Description of Instrument

IRIS is a two-element shearing interferometer operating at a primary wavelength of λ_1=26 μm, which is optimized for the detection of a standard extra-solar planet. Its main optical elements are two parallel, afocal telescopes with a D=3 m, f/3, off-axis parabolic primary mirror and a smaller secondary mirror in a Gregorian configuration. The telscope axes are separated by a fixed distance b=13 m, the interferometer baseline.

Since in the infrared the images (Airy disks) of an extra-solar planet and its parent star overlap, detection of the planet can only be accomplished by interferometric nulling of the star. This is done by pointing the optical axis (OA) of IRIS on the star and combining the two images (wavefronts) from the two telescopes (interferometer legs) 180° out of phase. The planet is off-axis, and the planet signal on the detector which has the stellar image nulled, depends on the planet location (θ, ϕ) in the reference frame of the sensor. By rotating IRIS about the OA at an angular frequency ω, the planet signal is modulated at a frequency 2ω, while the diffuse sky background gives a steady, though large, DC signal. Rotation is thus a form of chopping whereby distinction between signal and noise is possible.

The harmonic content of the AC signal contains the desired information about the planet's location and infrared brightness. Planet detection is identical to the detection of a weak radar signal submerged in white noise, and the signal-to-noise ratio for planet detection, using one or more of the (independent) channels - the various harmonics - is derived from simple radar theory.

IRIS is an IR telescope with a very high spatial resolution and detection sensitivity. Within its wavelength range of operation, it can therefore be used to study astronomical IR objects which require these capabilities. Examples would be: protostars, circumstellar shells of young and old stars, multiple systems (including binary stars and planetary systems), galactic and extra-galactic sources and their structures, and the galactic nucleus. Such studies could be done at an angular resolution and with a photon collection efficiency more than an order of magnitude better than SIRTF (Space Infrared Telescope Facility). Since it is rotating, free-flying and with a long design life, it is also superior and more versatile than the proposed Shuttle infrared interferometer.

1.3 Summary of Results

We take detection of an extra-solar planet to mean: establishing the presence of a point-like object near a star, with a brightness and angular separation appropriate for a planet. The confidence level of detection is set by accepting a 1% missed detection rate and a 10% false alarm rate.

The standard planet-star model is defined as Jupiter and the Sun as seen from a standard distance of 10 parsecs (32 light-years). To model the planetary infrared radiation, a black-body spectrum at 125 K is assumed. The proposed wavelength of observation is 26±2 μm, a compromise between signal-to-noise ratio and detector efficiency. A secondary wavelength, 18±2 μm, is proposed for temperature determination, which along with orbit determination, will help ascertain that the discovered object is indeed a planet and not a second faint star.

Interferometric suppression of the stellar flux reduces the large star-planet infrared photon flux ratio (10^5) to levels such that zodiacal light is the major contributor to background. Rotation of the sensor about its optical axis, which is pointed on the star, modulates the planet signal while the background is constant. An interferometric baseline (aperture separation) of 13 m is chosen with consideration for 1) maximizing the S/N ratio (thereby minimizing the observation time) for the standard planet, 2) the overall size limits set by shuttle payload bay dimensions, and 3) minimum demands on baseline control. The observation time for the standard planet is one hour for proposed 3 m diameter primary apertures. The sensitivity of the observation time to moderate variations of the system and sensor parameters is studied. One interesting result is that IRIS is very sensitive to planet orbit radius. IRIS detection range, if defined by a 100 hour limit to the observation time for a planet, is about 30 parsecs.

IRIS has a well-defined design space enabling the above discussed background limited performance. Moderate to strong progress in thermal, dynamics and optical control is required. Careful design of the focal plane assembly is required. The detectors will be extrinsic photo-conductors (Si:XX, Ge:XX) with MOSFET followers and involving unconventionally large load resistors. Cryogenic cooling of the detectors below 11 K is required, and although liquid

Helium is preferred because of well-developed technology, alternatives such as solid Hydrogen should be investigated. To reduce thermal emission below the minimum background, the primary optics must be cooled below 30 K. A solid Neon cryogenic system is proposed. The required technology exists but is unproven for the required 5-year life time. Besides stray light from the main structure onto the primary mirrors, from dust and cloud contaminants, the suppression of infrared radiation from the optical path environment (particularly the tubes surrounding the collimated beam) needs attention in a design. Cleaning methods of the optics of particulates and condensates on-orbit must be developed or adapted from other programs.

IRIS performance depends also critically on the accurate nulling of the parent star. Precise optical alignment, particularly baseline length control, is required. The affordable error for the optical path difference between the two interferometer legs is $\lambda/3000$ (90 Å). Visible interferometry on the parent star, using the accurately figured central portions of the mirrors, will be applied to this problem to achieve the tolerances. The IRIS pointing requirements are less demanding (similar or below Space Telescope requirements).

As a large and moderately flexible structure, IRIS is subjected to torques and bending stresses of various origins. These present a major challenge to a structural design. The methodology and technology to meet the challenge exist, but extensive dynamical, structural and thermal analysis will be required. For example, stability augmentation may be necessary, but the question cannot be decided on without extensive modeling of the IRIS spacecraft structure.

Beryllium mirrors are proposed, because of their excellent mechanical and optical quality at cryogenic temperatures. The Beryllium technology is under development. Scalability to large sizes needs to be proven, and the surface treatment and figure control of IRIS mirrors will require special attention.

Our conceptual design of an IRIS satellite has an all graphite-epoxy structure fitting Shuttle payload size limits. The system has two 3 m diameter primary Beryllium mirrors and Beryllium secondaries, in an off-axis Gregorian configuration. The secondaries are deployed by separate trusses (towers)

which remain folded inside the shuttle bay. The system weight is 13,900 kg including 3,400 kg cryogen and 4,100 kg propellant (ACS and fuel for propulsion engine). IRIS will be delivered by special engine from Shuttle hand-off to an operational baseline circular orbit of 550 km altitude, 28.5° inclination. The orbit is chosen as a compromise between requirements for long life, low atmospheric and radiation interference, and shadow viewing requirements.

The ROM cost of one sensor system is $300M and does not include major developments of facilities. Estimates of the time scale and cost of major technology developments are given. They are incorporated in our suggested schedule for the development of an IRIS program. The overall time table for the program is: 2 years for technology development, 9 years total to launch.

Comparing IRIS to a feasible APOTS sensor, we find that IRIS is more sensitive by a factor 100 in observation time for the standard planet, and has a greater range (factor 2). The full realization of IRIS concept requires no fundamental technical breakthroughs, in contrast to APOTS. IRIS is heavier (factor 2) and a more complex system and will present greater design challenges than APOTS.

Further development of long-life cryogenic systems and mirror technology seem to be the two most pressing recommendations from our study of the two sensors.

2. Baseline System and Sensor Parameters

2.1 Justification

To establish the performance criteria and characteristics of the sensor system and to determine the enabling technology, we assume a simple target: a star with a single planet which in an abstract way represent our solar system. On a design level, the impact on sensor performance by a multiple planet system must be studied carefully. See App. E in Report NCA2-OR745-716. Obviously a system, like IRIS, which does not directly image but reconstructs the object space by harmonic analysis of the detector signal, is at a disadvantage for multiple systems.

The sensor performance must be optimized for the standard planet in the absence of any knowledge about extra-solar planets. In an actual observation

Table 2-1

A. STANDARD PLANET

Radius, R_p		7.0×10^7 m
Solid angle subtended at 10 parsecs, Ω_p		1.6×10^{-19} sterad
Star-planet angular separation, θ	maximum	2.5 rad
	average	2.0 rad
Orbit radius,		5.2 AU = 7.8×10^{11} m
Orbit period		12 years
Effective temperature at 26 μm, T_p		125 K
Spectral irradiance at 26 μm, F_p		2.5 photons/m^2.sec.μm

B. STANDARD PARENT STAR

Radius, R_s	7.0×10^8 m
Distance from earth, d	10 parsecs (32 light years)
Solid angle subtended at 10 parsecs, Ω_s	1.6×10^{-17} sterad
Magnitude (bolometric)	4.75
Temperature, T_s	5800 K
Spectral irradiance at 26 μm, F_s	2.1×10^5 photons/m^2.sec.μm

the performance may be quite poor if the planet-star system is unlike the standard. E.g., one can imagine hot, early type planets enshrouded in dust and gas. Since in such cases the assumed relationships between star and planet brightness, size, distance, etc. do not hold the IRIS performance characteristics derived in Section 3 may be quite different.

2.2 Baseline Planet and Star

The standard IRIS target (baseline system) is the Sun and Jupiter as seen from a distance of 10 parsecs (32 light-years).* Relevant parameters are given in Table 2-1. The system may be viewed from any angle, hence the average, not maximum, angular separation must be taken as standard. It is 2.0 μrad (0.41 sec) (see Appendix B).

We assume that the planet's apparent brightness does not vary with its phase of illumination. This is in contrast to APOTS where planet brightness changes strongly with phase and where the average and maximum planet brightness are quite different. The planet's infrared brightness is calculated from an effective temperature of 125°K at our suggested detection wavelength (26 μm). Judging from the literature, the third digit in the temperature figure is uncertain. Fig. 2-1 gives the spectrum at 125°K and at other temperatures.

For the star (sun) we assume a spectral brightness temperature of 5800°K, although our Sun is actually cooler at 26 μm. The difference in the photon flux is, however, insignificant (Fig. 2-2).

The thermal radiation of the planet peaks near 30 μm, whereas the visual radiation, reflected sun (parent-star) light, peaks at ~0.6 μm (Fig. 2-3). The two maxima, of course, represent wavelength candidates for planet detection. However, the actual wavelength of operation must be chosen with due consideration for other factors as well: for example, the background-limited S/N ratio, and the quantum efficiency of available detectors.

---

* If we take stars within 10 parsec from the Sun and brighter than, say 5th magnitude to be primary candidates for a planet search, we find only about a dozen of such stars. The number does not increase very rapidly with increasing magnitude (Appendix A), and therefore the total number of likely targets is small.

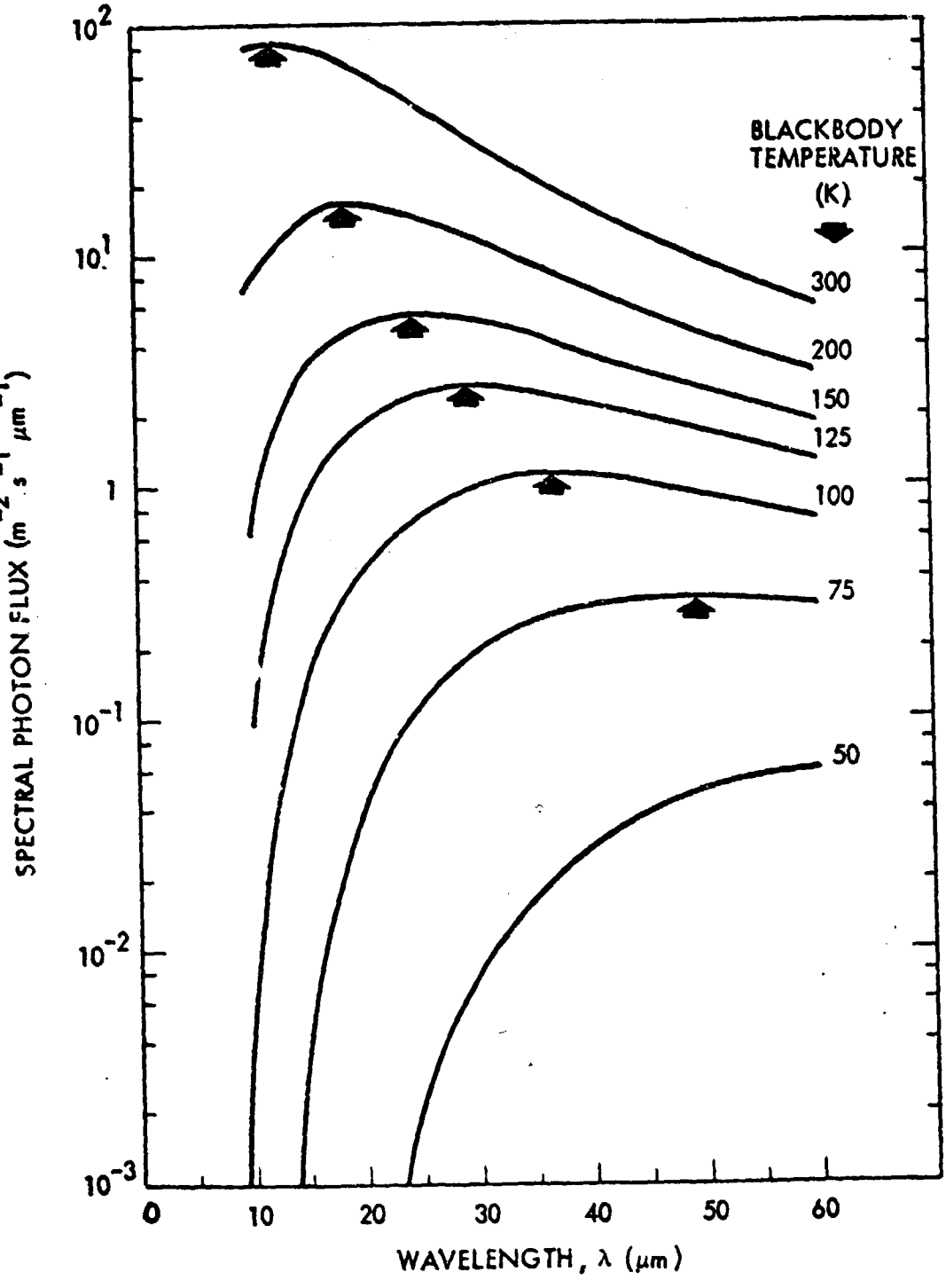

Fig. 2-1 Thermal Radiation Spectrum of Jupiter Size Planet At a Distance of 10 Parsecs

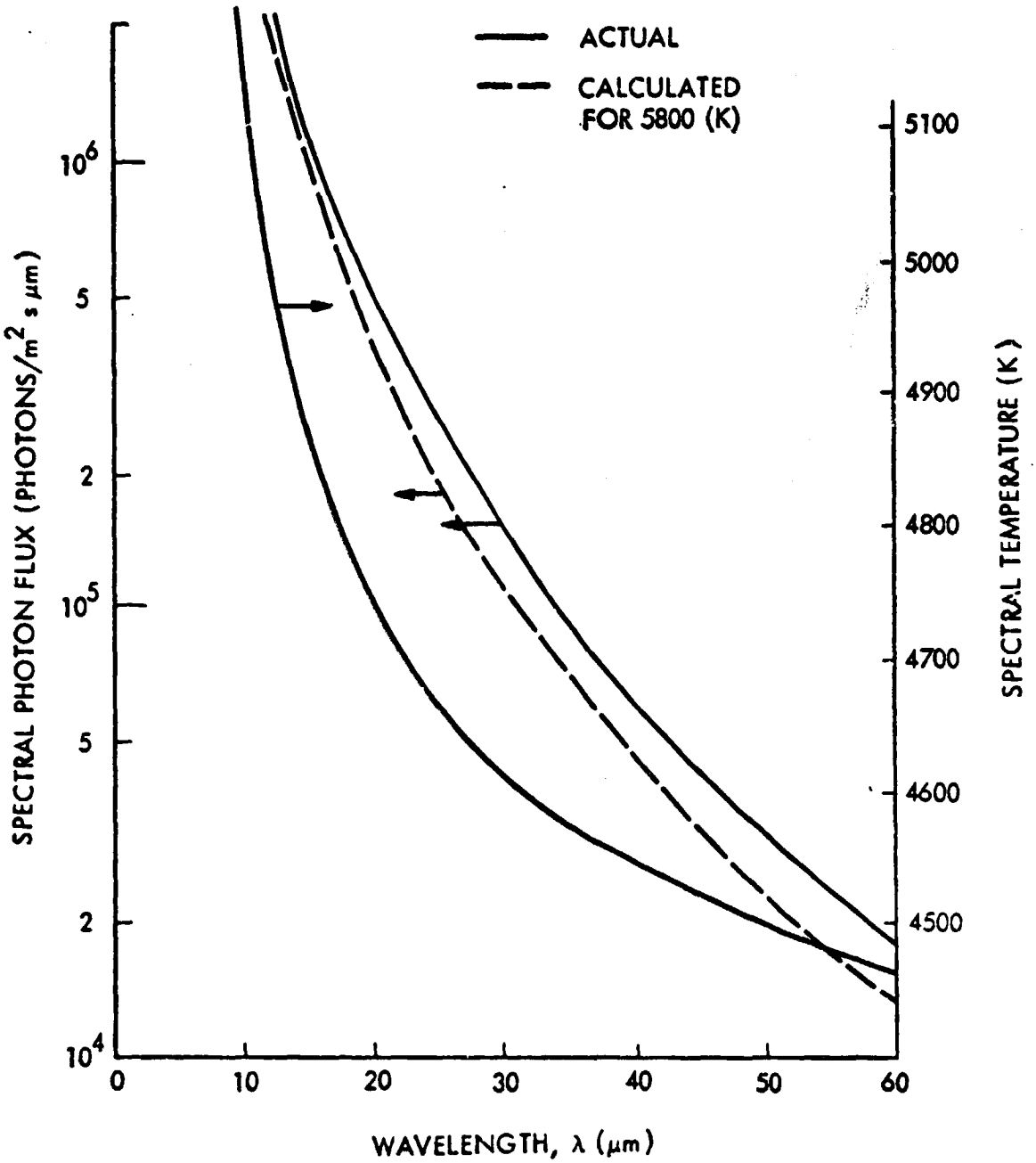

Fig. 2-2 Solar Radiation Spectrum at 10 Parsecs

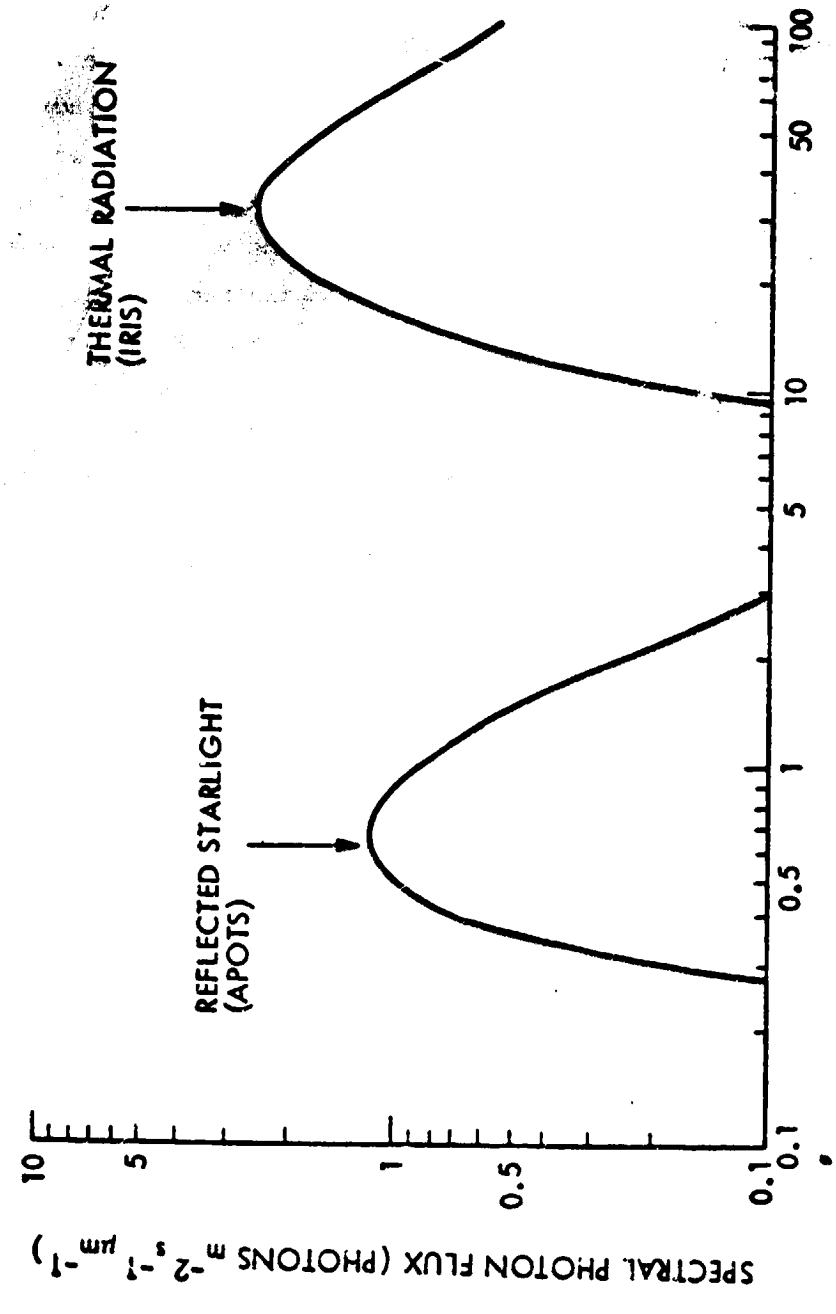

Fig. 2-3 Radiation Spectrum of Standard Planet

2.3 The Infrared Zodiacal Light

In the infrard (IR), the zodiacal light (ZL) is thermal radiation from interplanetary dust which is more or less concentrated toward the ecliptic plane. It is very much brighter than in the visible where it is sunlight scattered by the same dust. The IR ZL is the dominant background in IRIS observations. By contrast, for APOTS the main background is diffracted and scattered light of the parent star. The ZL cannot be interferometrically nulled like the parent star and it can only be eliminated by sending the sensor out of the ecliptic plane or far away from the Sun. Knowledge of the ZL is therefore crucial to an accurate evaluation of IRIS performance. Unfortunately, the observational data, shown in Fig.2-4, are sparse in terms of both, wavelength and spatial coverage. Furthermore, they are earth-shine contaminated and therefore represent an upper limit. By contrast, the spatial distribution of the visible zodiacal light is well established. In particular, it is faintest at the ecliptic poles where it is about a factor 3 less than at 90° elongation angle from the sun in the ecliptic plane.

The infrared ZL data were taken mainly in the ecliptic plane, at elongations near 90°. If the spatial distribution were the same as in the visible, we would assume that the minimum zodiacal light occurs at the eliptic poles and is a factor ~ 3 less than at 90° in the ecliptic plane. If the IR ZL data are thus evaluated, one obtains a maximum model of the infrared ZL, shown as the upper curve in Fig. 2-5. Evidence has however been cited which seems to indicate the ZL is much less at the poles. A ZL model which has widely been accepted on that basis is given in the COBE report. The model makes a gray-body fit to the data at 10 μm, with a temperature of 300 °K and an emissivity which is inversely proportional to the wavelength:

$$T_z = 300\ ^{\circ}K$$
$$\epsilon(\lambda) = 1.2\times10^{-7}/\lambda \qquad (2\text{-}1)$$

where λ is in μm. The radiance, in units of photons/m^2.sec.sr. m. can then

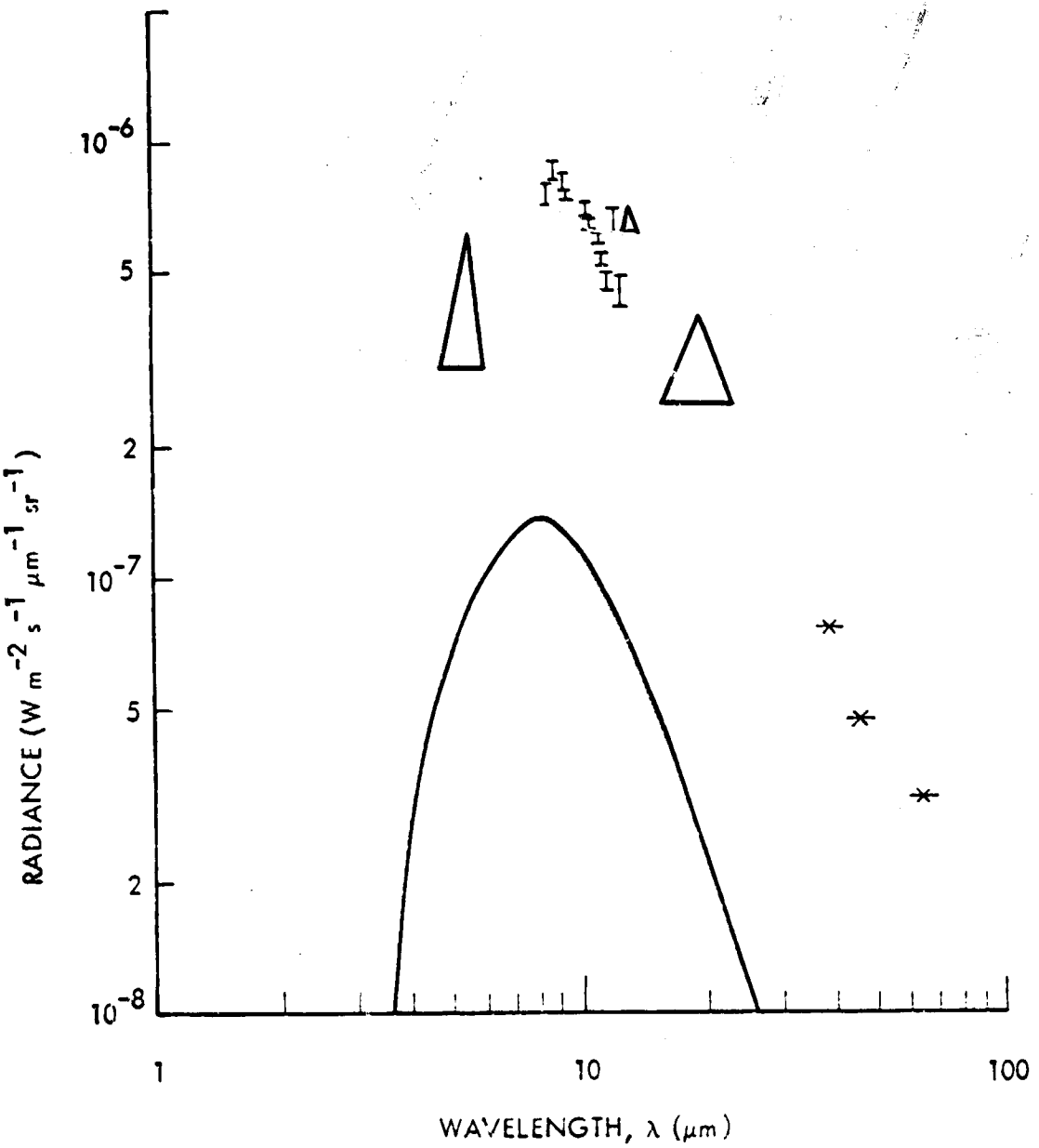

Fig. 2-4 Infrared Zodiacal Light

Δ, I, ✱ Near-Ecliptic Measurements (Adapted From COBE Interim Report, 1977)

——— 300 K Grey-Body Fit at Ecliptic Poles

be written in the form

$$I_z = \frac{7.2\times10^{19}}{\lambda^5}\ \frac{1}{e^{48/\lambda}-1} \qquad (2\text{-}2)$$

where λ is in μm.

The rate of photons to the Airy disk of the planet is

$$P_z = I_z\left(\frac{1.22\lambda}{D}\right)^2\pi\cdot\frac{\pi D^2}{4} = 3.7\lambda^2 I_z \qquad (2\text{-}3)$$

The rate is shown in Fig. 2-5 for both models (MAXIMUM and MINIMUM). The rates differ substantially at the long wavelengths, and by about a factor 10 at 26 μm, which is the suggested operational wavelength for IRIS for the detection of the standard planet. In what follows we shall adopt the more widely accepted COBE model given by Eq. (2-2) and suggest that it may be somewhat low (factor 2.5) so that the calculated observation times for IRIS may possibly optimistic by a factor 2.5.

2.4 Detection Wavelength

If we assume that the star is effectively nulled (Sec 3-1) and that the zodiacal light is the remaining background (atmospheric radiation negligible; radiation from optics and focal plane adequately suppressed by active and passive cooling), the detector signal-to-noise ratio, S/N, will be proportional to

$$\frac{\text{planet photons to detector}}{\sqrt{\text{zodiacal light photons to detector}}}$$

This ratio is plotted as a function of wavelength in Fig. 2-6 for the two zodiacal light models: minimum and maximum (both referring to the ecliptic pole brightness). The respective S/N ratios peak somewhere between 25 and 40 μm, and therefore the exact choice of the observation wavelength window depends on the efficiency of available detectors. In fact, in view of the uncertainty about the IR zodiacal light, the choice should be heavily influenced by the detectors. The principal choices are extrinsic photoconductors since

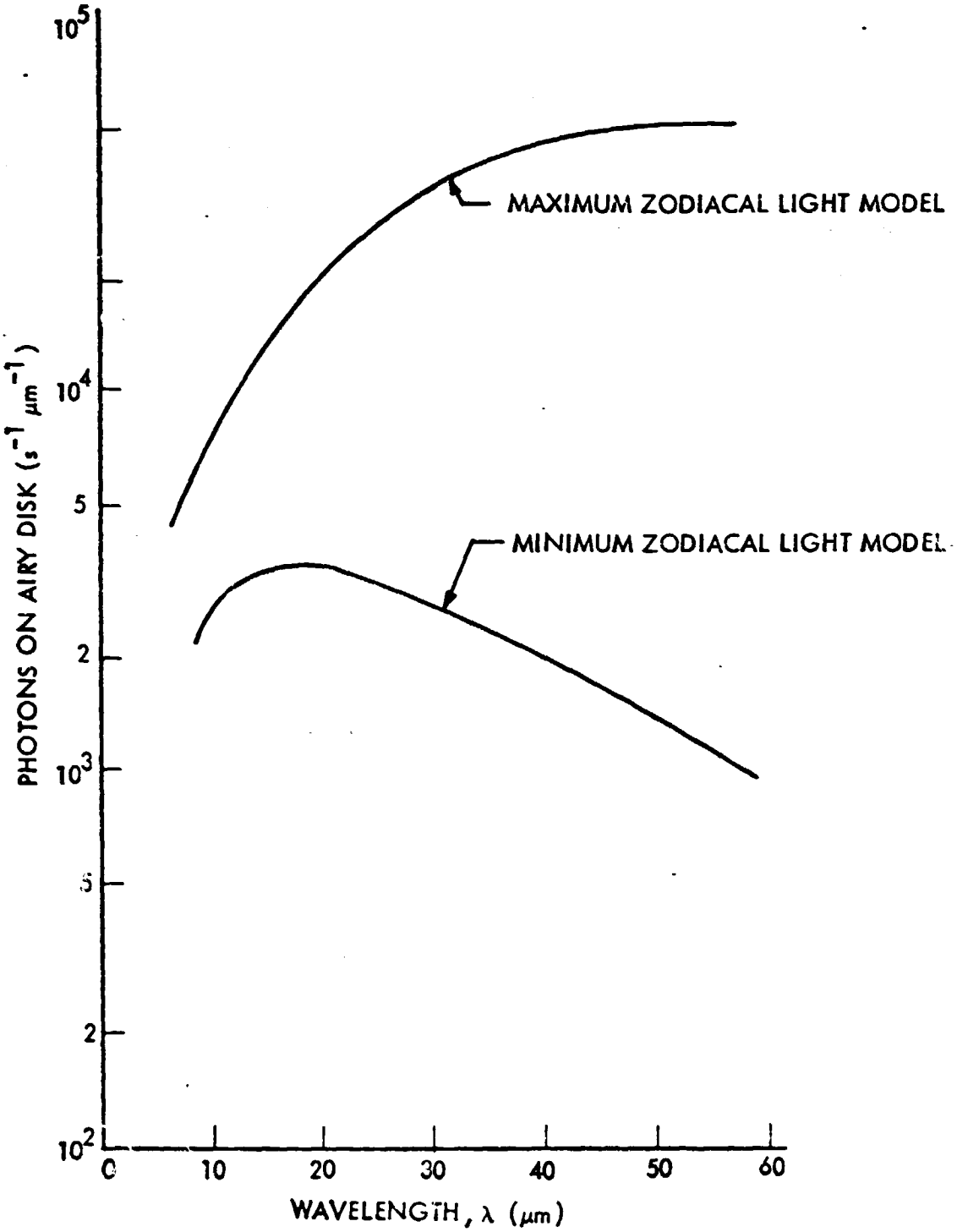

Fig. 2-5 Extreme Zodiacal Light Models at Ecliptic Pole

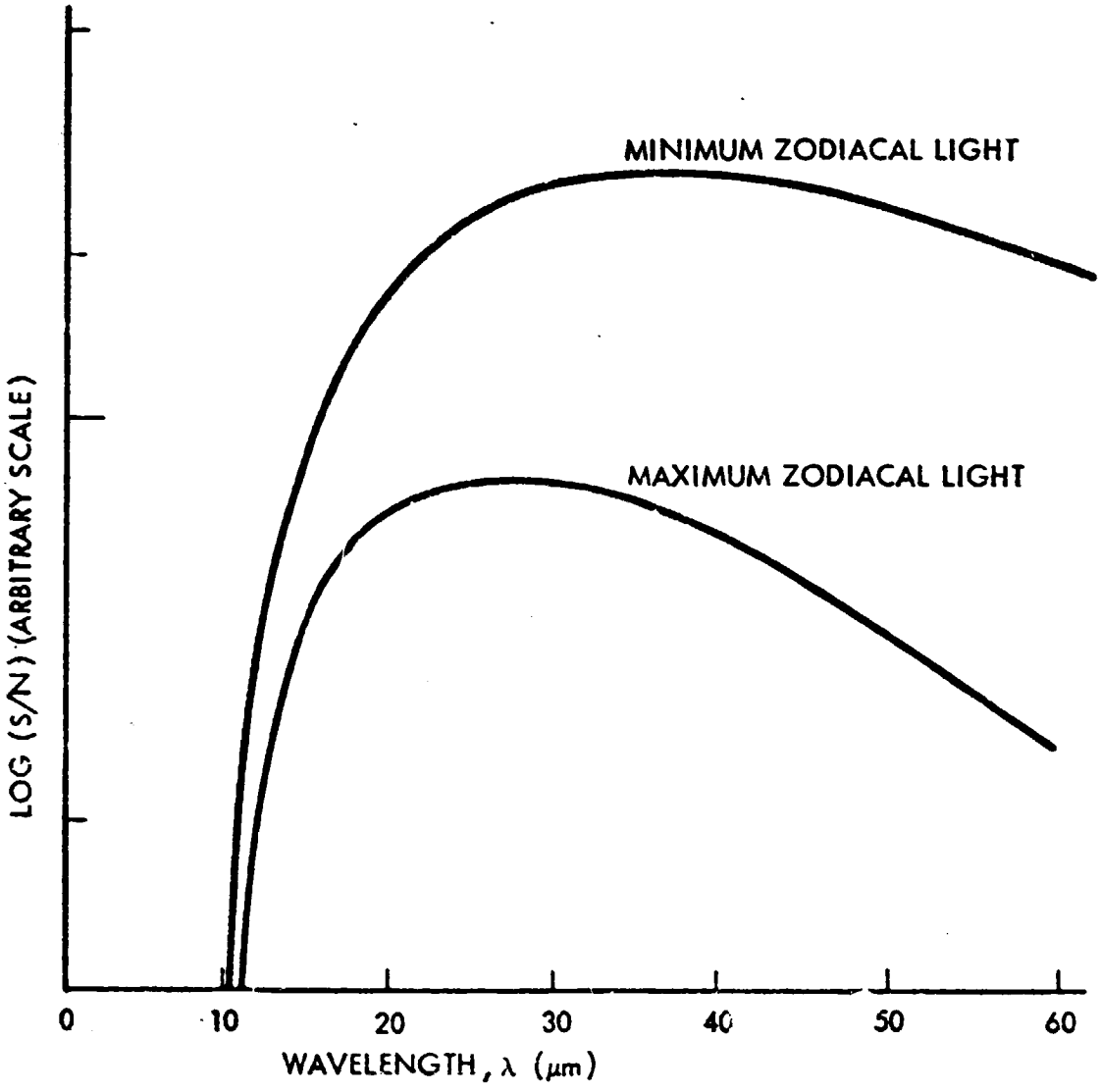

Fig. 2-6 SImplified Siganl-to-Noise Ratio

other detectors lack the necessary sensitivity for this experiment. Of these, Ge:Cu and Si:Sb cut of near or below 30 m. Ge:Cu which is better developed than Si:Sb, cuts off at 28 to 29 m. We therefore accept 28±2 m as the standard observation wavelength interval.

2.5 Secondary Wavelength of Observation

One purpose of two-or multi-color observations would be to establish the temperature of the discovered object and thereby help determine if indeed it is a planet. Let us consider the simplest case of one second wavelength and determine its optimum value from simple considerations, which perhaps could be refined in a later study.

We adopt the simple criterion that the error in the temperature calculated from observations at two wavelengths, λ_1 and λ_2 only, should be a minimum. The temperature is determined from the ratio r of the photon fluxes

$$r = \frac{\lambda_2^4}{\lambda_1^4} \cdot \frac{e^{hc/\lambda_1 kT} - 1}{e^{hc/\lambda_2 kT} - 1} \tag{2-4}$$

The fractional errors of r and T are related by

$$\frac{\Delta T}{T} \approx \frac{\Delta r}{r} \cdot \left[\frac{x_1}{1 - e^{-x_1}} - \frac{x_2}{1 - e^{-x_2}} \right]^{-1} \tag{2-5}$$

where

$$x = hc/\lambda kT.$$

If $(S/N)_1$ is the signal-to-noise ratio of the detectors at λ_1, $(S/N)_2$ at λ_2, then we may write

$$\frac{\Delta r}{r} \approx \sqrt{(S/N)_1^{-2} + (S/N)_2^{-2}} \tag{2-6}$$

and thereby calculate $\Delta T/T$ as a function of λ_1 and λ_2. The results are shown in Fig. 2-7 for the standard planet and for the case of a planet at 150 K or 100 K temperature. (In all cases we assume λ_1=26 μm) The ordinate in the figure is linear (arbitrary scale). $\Delta T/T$ is large for a short wavelength because of a poor S/N ratio, and it has a minimum value at λ_2=15 μm for the standard planet (T=135 K). In order to include the possibility (certainly real!) of planetary temperatures slightly different (especially colder) from the standard, we suggest a secondary wavelength of λ_2=18 μm.

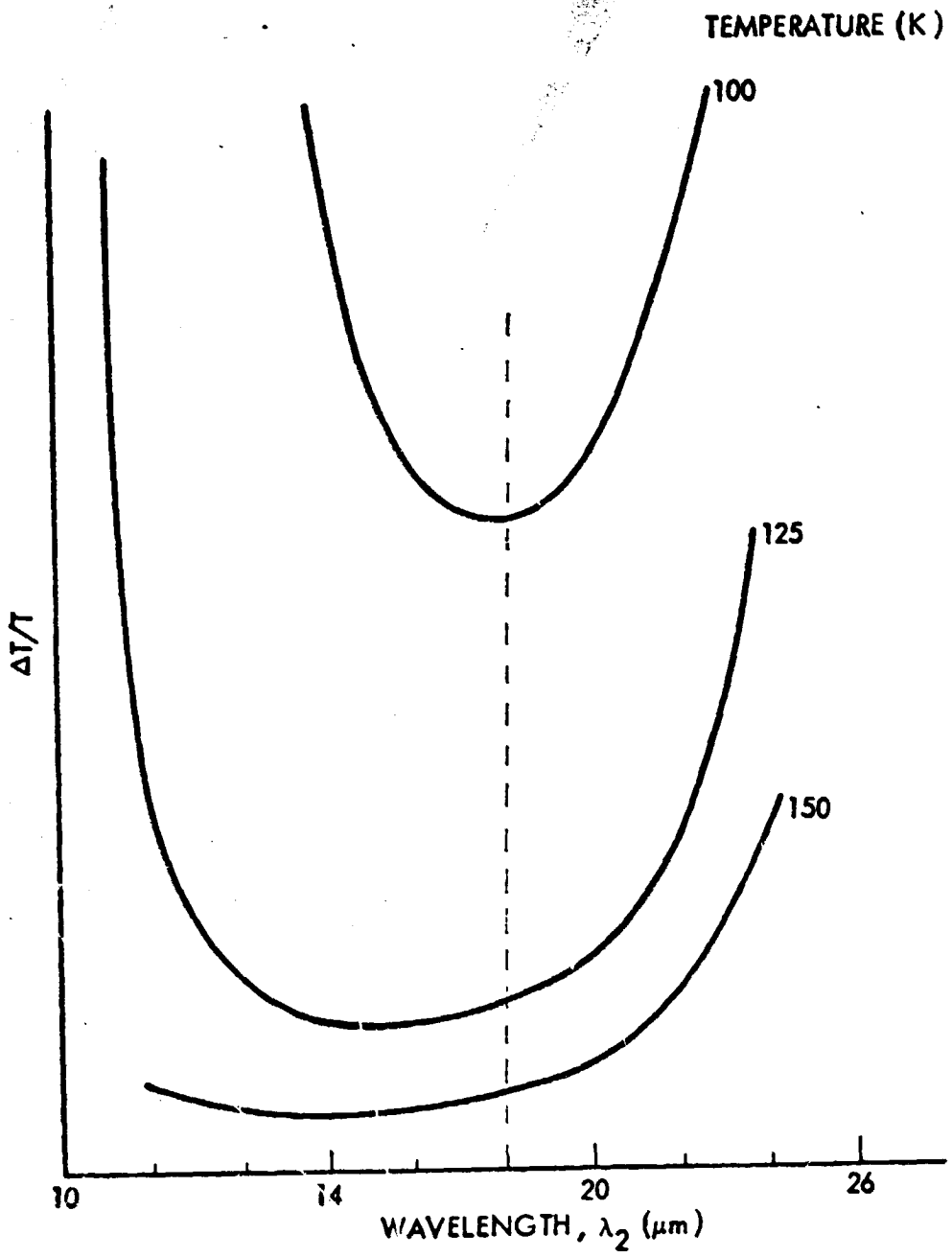

Fig. 2-. Relative Error in Two-Color Temperature Determination (λ_1 = 26 μm)

2.6 Telescope Aperture

Choice of the primary aperture is strongly influenced by desire for a large photon flux, which increases as the diameter D^2, but it must be comprised by considerations for ease and cost of manufacturing and figure control, the impact on system weight and complexity (particularly on the cryogenics, in this case) and, of course, the limits set by the Shuttle payload pay.

Current facilities for the manufacturing of high-quality mirrors set a limit of about 4 m diameter; so do Shuttle payload bay dimensions (4.3 m maximum width). Larger mirrors must be manufactured in segments and the segments are stored during launch in folded form. They are deployed after delivery to the operational orbit and must then be phased accurately. The obvious difficulties and risks of such a procedure draw us away from very large apertures for this application.

The IRIS mirrors are cooled actively to <30 K (see Sec. 4-2) and the demand on cryogen is approximately proportional to D^{γ}, where $\gamma \leq 2$. We find that for a 3 m aperture diameter (i.e., two 3 m primary mirrors), 1/4 of IRIS weight is the cryogen system. We also find that the technical challenge of manufacturing and figuring moderately large apertures for this application is impressive and has a substantial risk.

Finally, we must assume equal aperture diameters for IRIS and APOTS (discussed in vol 2 of this report) in order to be able to compare their performances. We find that APOTS faces great difficulties in mirror technology.

Due to the above considerations we suggest a standard aperture of 3 m. We shall determine how the sensor performances vary with diameter. In case of IRIS, the variation is simple: the observation time is proportional to D^{-4}.

Since development of technology and fabrication, on-orbit cooling and cleaning of such large mirrors are technology issues, it appears reasonable to investigate if reducing the diameter would be beneficial to the program.

Fig. 2-8 shows some of the interrelation between D and other systems parameters. The following relationships are assumed:

1. Observation time per star $\propto D^{-4}$ (Sec 3-6)
2. Cost of mirrors $\propto D^{2 \text{ to } 3}$
3. Cryogen requirements $\propto D^{2 \text{ to } 3}$

The cryogen requirements (sNe) for a five-year mission were calculated from the estimated heat load on the mirrors, which is primarily thermal conduction through the mirror supports and thermal radiation (from the MLI and from vapor cooled heat shields inside the primary mirror baffle tubes). The two contributions, conduction and radiation, were equal. Another 20% of heat load was added for miscellaneous (including unknown or unexpected) heat leaks. The heat load by radiation is proportional to D^2, that by conduction, proportional to $D^{2 \text{ to } 3}$: D^3 if it is assumed that the number of mirror supports is proportional to mirror weight and that (weight $\propto D^3$); and D^2 if the mirror thickness does not vary proportional to D or the total contact area of supports is proportional to the mirror area instead. Thus

$$\text{heat load} = Q = Q_{D=3m} \cdot \frac{1}{2}\left[\left(\frac{D}{3}\right)^2 + \left(\frac{D}{3}\right)^{2 \text{ to } 3}\right] \qquad (2\text{-}7)$$

(D in m). Suppose D=2 m, then the heat load would be roughly a factor 0.4 less than for D=3 m, and for a fixed mission duration (5 years) 60% less cryogen (SNe) would be required, a total weight savings of ~2100 kg (cryogen and tankage). Apart from an associated savings of cryogen and tankage cost, there are 20% savings of propellant (orbit transfer), and savings in weight and cost of structure associated with the primary mirrors (as well as the mirrors themselves). There is also an impact on the weight distribution and thus on the inertia ellipsoid of IRIS which must be considered for its implications for the dynamics of IRIS. For example, the moment of inertia about the spin axis will be reduced due to loss of weight of structure, mirror, cryogen and systems mass (the baseline separation and the primary-secondary mirror separation presumably still being the same as for 3 m primary mirrors).

Fig. 2-8

MIRROR DIAMETER TRADES

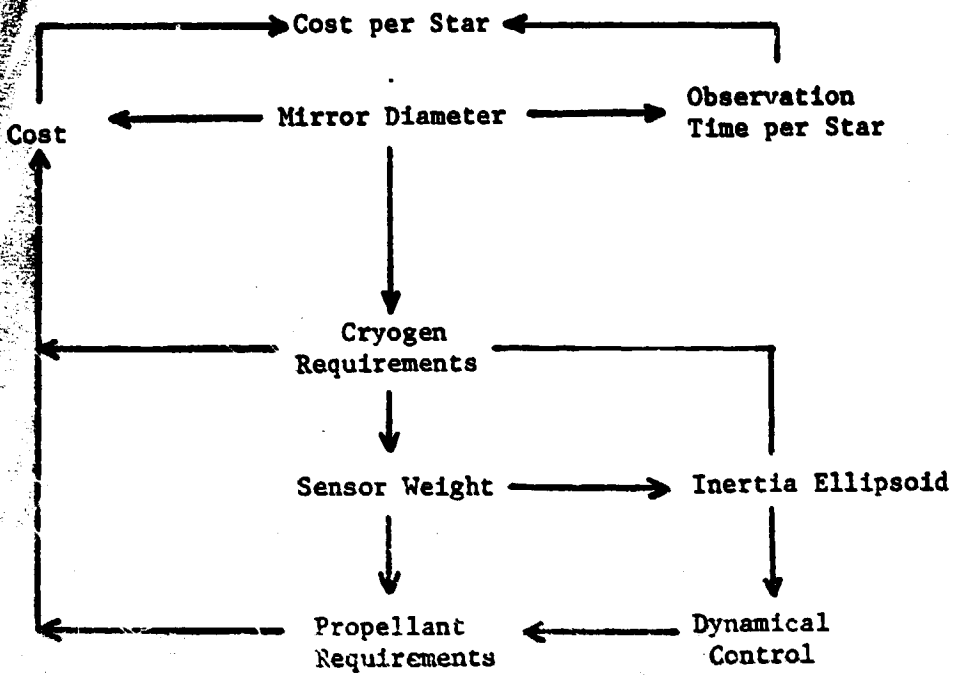

From a mission objectives point-of-view, the total number of stars surveyed for a given effort, i.e the cost per star, is of utmost importance. Since the observation time per star (necessary for detection of a planet) decreases with diameter, in proportion to D^{-4}, while the cost (associated with fuel, cryogen, system and support) increases less rapidly, the cost/star increases with decreasing diameter of the primaries, possibly as rapidly as D^{-3} since the cost of cryogen, mirrors, and fuel is not a large fraction of total systems development cost. In conclusion then, we do not consider reducing the primary mirror diameter to be advantageous.

2.7 Baseline Observation Conditions

We now summarize the results of the previous sections to define a standard observation condition.

The spectral photon flux of the zodiacal light to the Airy disk of the planet at 26 μm is

$$\rho_z = 3.7 \lambda^2 I_z = 2300/\text{sec}/\mu\text{m}. \quad (2\text{-}8)$$

The planetary photon flux is

$$\rho_p = \frac{2c}{\lambda^4} \cdot \frac{\Omega_p}{e^{hc/\lambda k T_p} - 1} \cdot \frac{\pi D^2}{4} \cdot 0.84 = 15/\text{sec}/\mu\text{m} \quad (2\text{-}9)$$

The stellar flux is

$$\rho_s = \frac{2c}{\lambda^4} \cdot \frac{\Omega_s}{e^{hc/\lambda k T_s} - 1} \cdot \frac{\pi D^2}{4} \cdot 0.84 = 1.2 \times 10^6/\text{sec}/\mu\text{m} \quad (2\text{-}10)$$

The star-to-planet photon flux ratio is ~75,000 - the same order of magnitude as for the APOTS sensor, which operates in the visible. In case of APOTS, however, the planet image falls into the diffraction rings of the star while for IRIS the two images practically overlap (see Fig. 2-9). APOTS and IRIS therefore naturally demand different techniques to resolve the planet from the parent star image. Note that the planet-to-zodiacal light photon flux ratio is proportional to D^2, hence the observation time is roughly proportional to D^{-4}.

The standard observation conditions are summarized in Fig. 2-10.

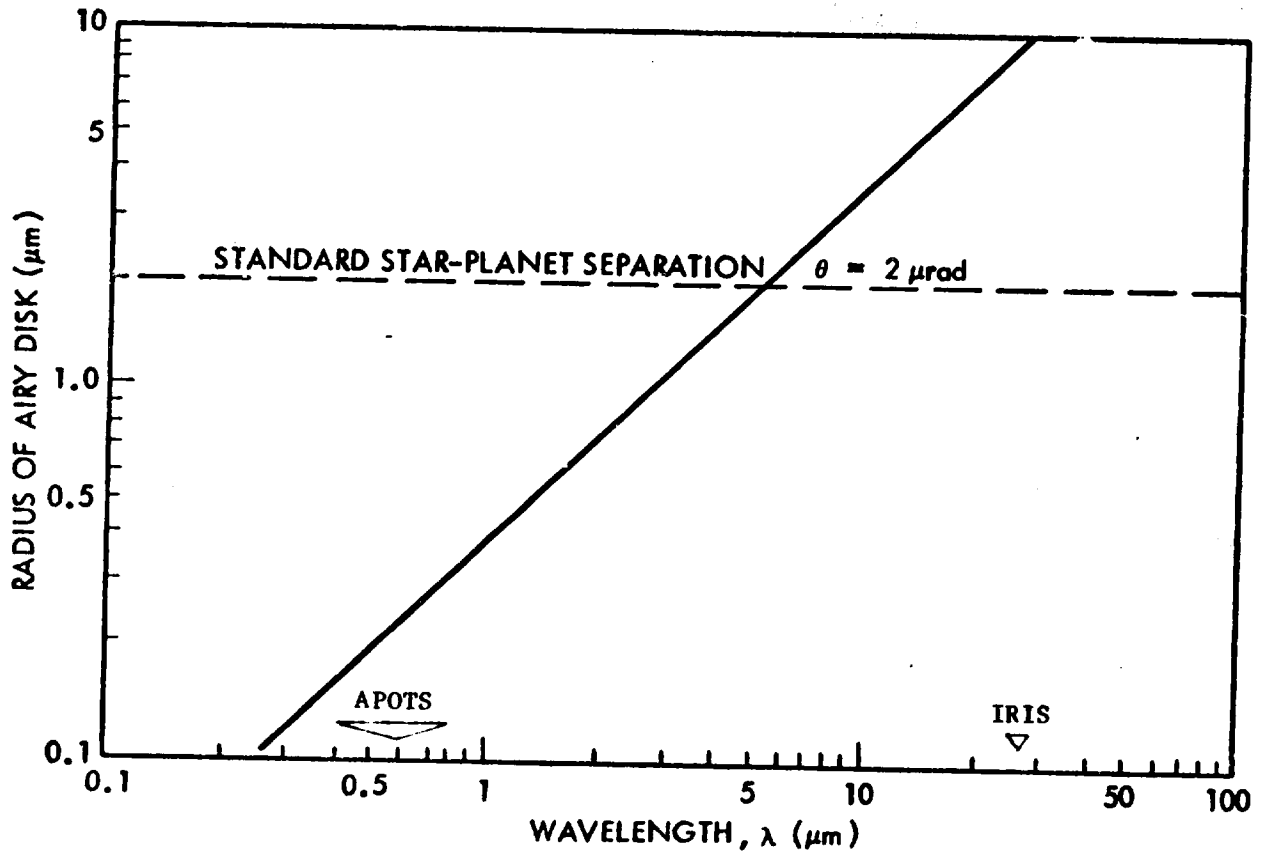

Fig. 2-9 Size of Airy Disk

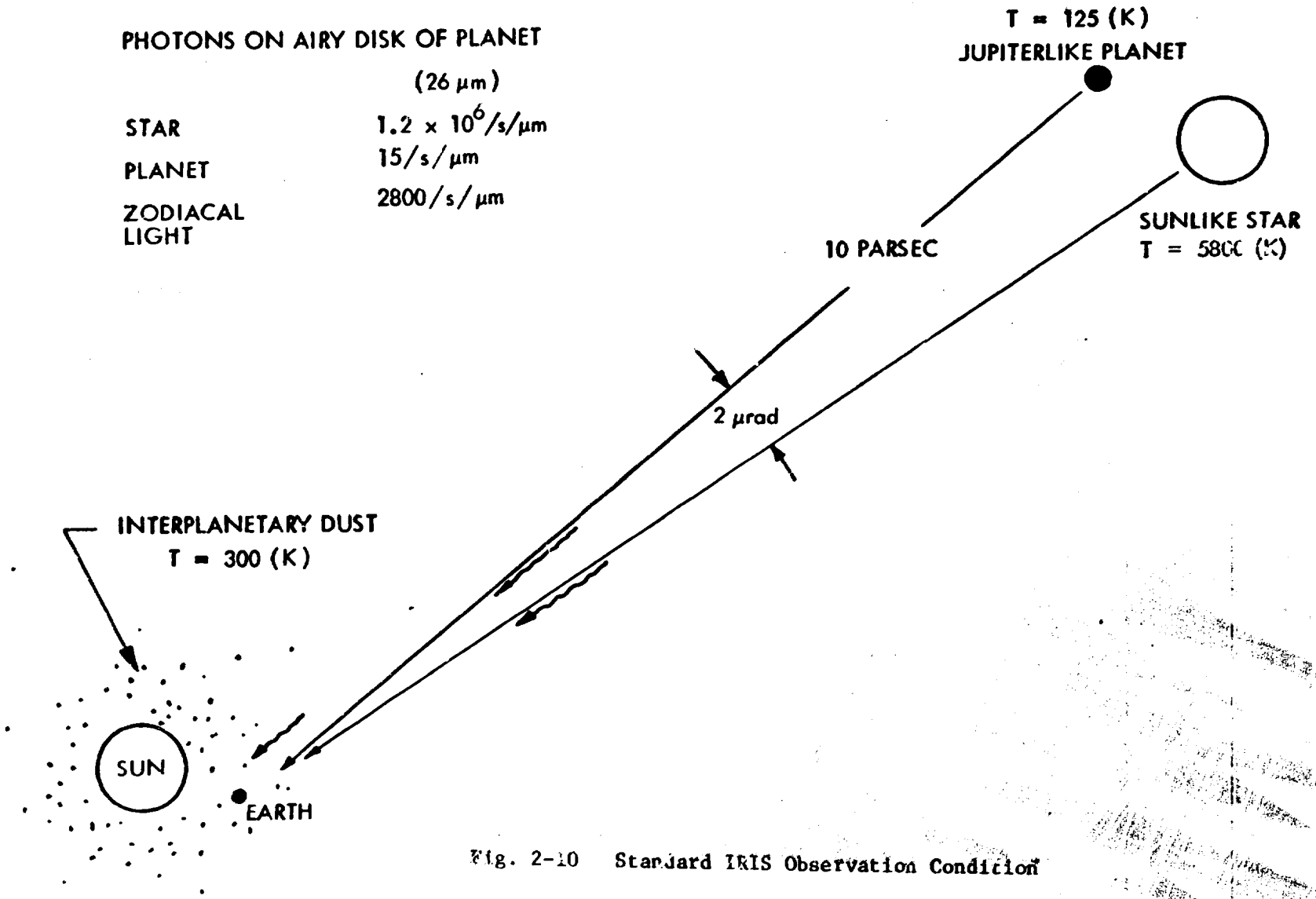

Fig. 2-10 Standard IRIS Observation Condition

3. Sensor Operating Principles and Performance Characteristics

3.1 Physical Principles of Spinning Interferometer

In the infrared (IR) one faces two tasks for the detection of extrasolar planets: 1) to resolve the planet from the star image; 2) to discriminate against the constant background (zodiacal light), and 3) to confirm that the discovered object is indeed a planet and not a background star or other point-like IR source. Some of the questions on 3) are dealt with in Sec. 3-5. We now address 1) and 2).

Since the stellar and planetary images overlap in the IR, apodization, which could separate them in the visible, cannot in the IR. Instead, one must interferometrically null the star. This is accomplished by dividing the stellar wavefront into two equal parts which are combined later with a phase difference of 180 degrees. Details of this method are discussed in the original study of the infrared interferometer, Report NCA2-OR745-716. We shall review the main ideas.

IRIS consists of two similar parallel telescopes separated by a fixed distance b, the interferometer baseline. An extra mirror in one of the legs reverses the image in that leg so that the wavefronts are superimposed: left edge on left edge, right edge on right edge, etc. Otherwise, the baseline b would vary from center to edge of each mirror. Consult Fig. 3-1 and Sec 5.

The collimated wavefronts from each telescope are combined on a 50% dielectric beamsplitter which introduces a 90° phase difference between the combined reflected and transmitted wavefronts (Fig.3-1). An additional 90° phase shift is added so that for an object on the interferometer axis, the wavefront from one of the beamsplitter outputs (the null port) is eliminated and all of the received on axis energy exits the beamsplitter from the second output (the antinull port). Pointing the interferometer at a star will thus result in nulling out the stellar photons.

The planet, however, is slightly off axis, and due to the path length differences to the interferometer will not necessarily be nulled. In fact, for a source point at (θ, ϕ) relative to interferometer axis (θ defines the

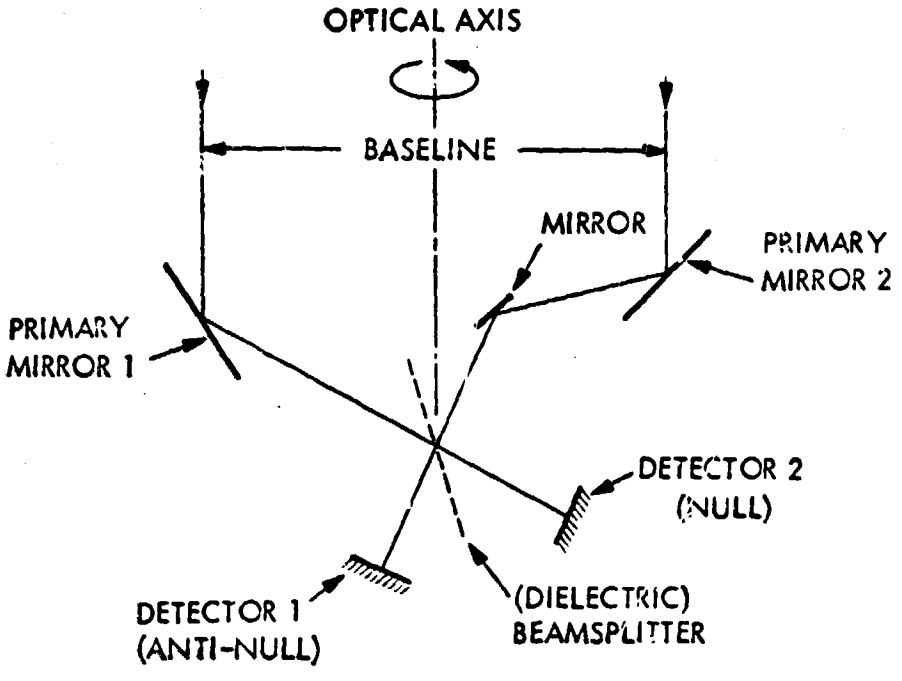

Fig. 3-1 IRIS Operational Principle

radial distance θ, ϕ defines the orientation), the signal on the "null" detector is proportional to

$$\sin^2\left[\frac{\pi b\theta}{\lambda}\cos(\alpha-\phi)\right]$$

where α the orientation angle of the IRIS baseline (body axis) (Fig. 3-2). When the interferometer is rotated about the axis $\theta=0$ at the rate w, we have $\alpha=wt$, and the signal from the point source at (θ,ϕ) is modulated at the basic frequency (2w). For points on-axis, and for extended sources, the signal is constant. Rotation therefore discriminates between the planet on the one hand and the star whose finite-size disk gives a small residual DC signal, about 10^{-6} of the unsuppressed value and the zodiacal light on the other. Thermal emission by the optics also gives only a DC signal.

The suppressed stellar signal is proportional to

$$\iint \sin^2\left(\frac{\pi b\theta}{\lambda}\cos\phi\right) d\Omega_s$$

whereas unsuppressed it is proportional to Ω_s, which is the solid angle subtended by the star at earth (1.6×10^{-17} sterad for the standard star).

Therefore, the interferometric suppression factor is

$$S.F. = \frac{1}{\Omega_s}\iint \sin^2\left[\frac{\pi b\theta}{\lambda}\cos\phi\right] d\Omega_s$$

$$\approx \frac{\pi}{\Omega_s}\left(\frac{\pi b}{\lambda}\right)^2\int \theta^3 d\theta = \frac{\pi}{4}\left(\frac{b}{\lambda}\right)^2\Omega_s$$

where θ_s is the stellar angular radius and $\Omega_s=\pi\theta_s^2$. For b=13 m (choice explained in Sec 3-5), λ=26 μm, S.F.=2.7×10^{-6}. This factor is larger than that calculated by Bracewell, Black and McPhie (pg. 27) because their baseline is shorter and their wavelength is longer.

An example of a modulated planet signal is shown in Fig. 3-3. The interferometer essentially places a grid of varying transmission on the sky, with maxima (antinulls, A) and minima (nulls, N). The parent star is placed onto a N by pointing the interferometer axis on the star. As a result of the rotation of the interferometer, the planet passes in a circle around the star, traversing nulls and antinulls at unequal time intervals. (Fig. 3-3 left) The planet signal is Fourier analyzed in terms of the harmonics of (2w): 2w, 4w, 6w and so on. The relative strengths of the harmonics depend on the exact location of the planet and can, therefore, be used to calculate the location.

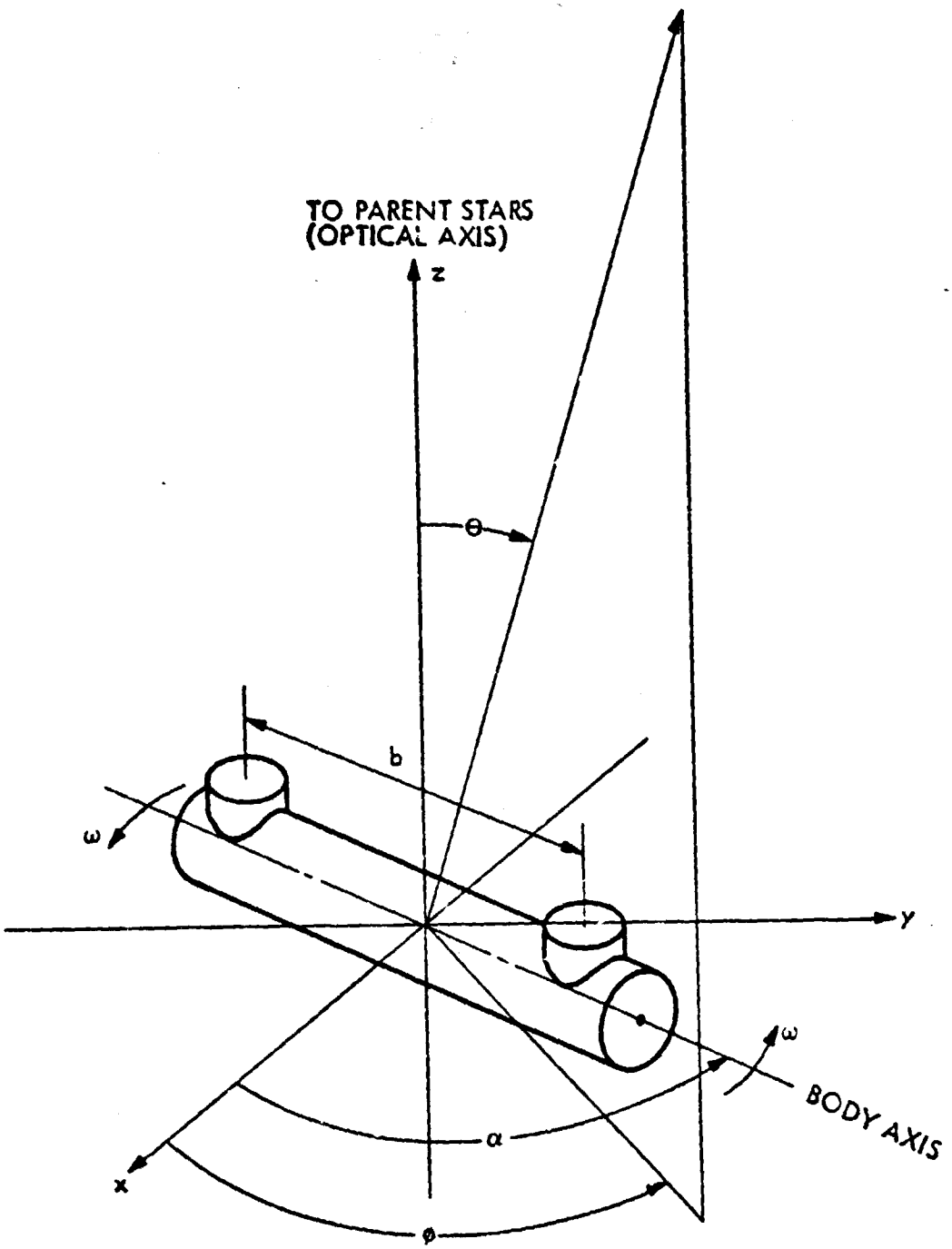

Fig. 3-2 IRIS Coordinates

(Adapted from NCA2-OR745-716)

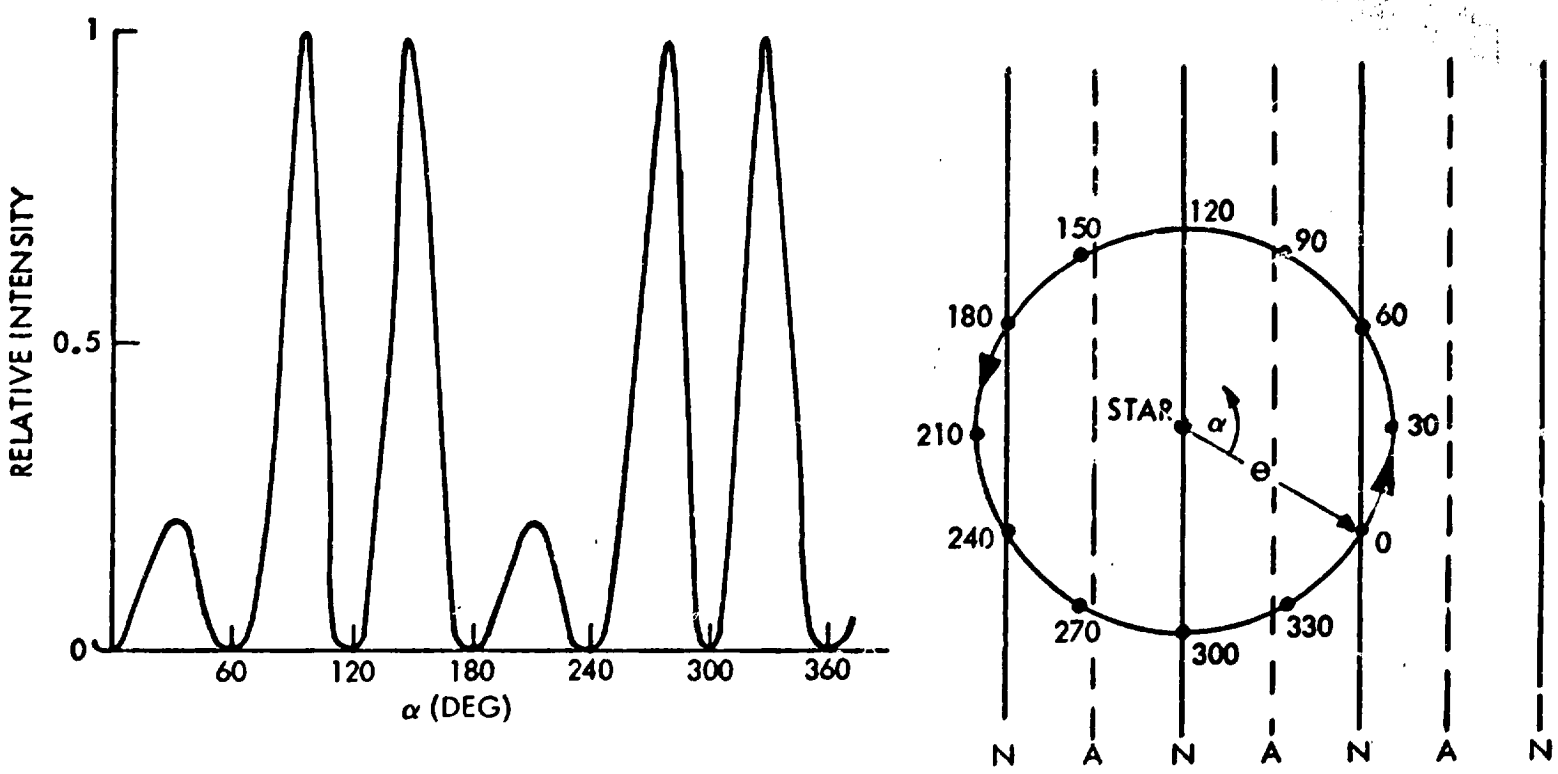

Fig. 3-3 Signal on Null Detector

(Adapted from NCA2-OR745-716)

From Fig. 3-3 it is obvious that the measured position angle, ϕ, of the planet is uncertain by 180°. Suggestions for removing the uncertainty are made in Sec. 5.2.4. The removal incurs a loss in signal-to-noise and is therefore not pursued further at this time.

3.2 Analysis of Sensor Signal

The planet signal on the null detector (star nulled) is proportional to

$$\sin^2\left[\frac{\pi b\theta}{\lambda}\cos(\alpha-\phi)\right] = \frac{1}{2}\left[1-J_0\left(\frac{2\pi b\theta}{\lambda}\right)\right]+\sum(-1)^{m+1}J_{2m}\left(\frac{2\pi b\theta}{\lambda}\right)\cos\left[2m(\alpha-\phi)\right] \tag{3-1}$$

where J_m is the Bessel function of order m.

The signal contains a constant term (D.C)

$$\frac{1}{2}\left[1-J_0\left(\frac{2\pi b\theta}{\lambda}\right)\right]$$

and the time varying terms or harmonics

$$(-1)^{m+1}J_{2m}\left(\frac{2\pi b\theta}{\lambda}\right)\cos\left[2m(\alpha-\phi)\right]$$

Only even harmonics exist.

We note that, $J_\nu(z)\propto z^\nu$, $z\ll 1$. Therefore, for sources very close to the interferometer axis (θ small), the signal will be found in the lower harmonics. Small pointing errors of the interferometer will produce a large second harmonic signal from the parent star which will be indistinguishable from that produced by a planet. Therefore, we must either ignore the second harmonic signal component or accurately compensate for interferometer pointing errors.

The relative magnitudes of the various planetary harmonics - if there is a planet - are of course not known a priori. However, for the standard planet we know θ and thus can calculate the ratio of the various harmonics. The interferometer baseline is chosen so that a strong fourth harmonic signal (unaffected by pointing error) will be produced by the standard planet. Conveniently, the b=13m baseline interferometer will just fit the shuttle compartment.

The interferometer can be designed with a pointing error compensation loop. If this is successfully accomplished, the usable second harmonic signal will provide a higher S/N ratio (than if only the fourth harmonic were used) and will increase interferometer sensitivity on planets so close to the parent star that their signal is nearly all second harmonic.

3.3 Signal-to-Noise Ratio

The harmonic analysis of the planet signal is accomplished by dividing the planet signal into Q equal time bins per rotation period, τ. If $\bar{n}_{q,p}$ is the average number of planet photons received by the q-th bin in one rotation period, then

$$\bar{n}_{q,p} = \int_{(q-1/2)\tau/Q}^{(q+1/2)\tau/Q} \overline{(dn/dt)}\, dt \qquad (3\text{-}2)$$

$$= \frac{1}{2}\frac{\tau\rho_p}{Q}\left[1 - J_0(x)\right] + \frac{\tau\rho_p}{Q}\sum_{m=1}^{\infty} J_{2m}(x)\cdot \mathrm{sinc}\left(\frac{2\pi m}{Q}\right)\cdot (-1)^{m-1}\cdot \cos\left[2m\left(\frac{2\pi q}{Q}\right) - \phi'\right]$$

where

$$x = \frac{2\pi b\theta}{\lambda} \qquad (3\text{-}3)$$

During the same time, τ, the zodiacal light (plus unnulled DC star signal and optics thermal emission) gives

$$\bar{n}_{q,z} = \tau\rho_z/Q \qquad (3\text{-}4)$$

photons in that bin. Let ρ_p be the rate of planetary photons incident to the null detector, and ρ_z the corresponding zodiacal rate. Forming the discrete transforms:

$$\overline{C_{2m}} = \frac{1}{Q}\sum \bar{n}_{q,p}\cos\left[2m\frac{2\pi q}{Q}\right]\ ;\quad \overline{S_{2m}} = \frac{1}{Q}\sum \bar{n}_{q,p}\sin\left[2m\frac{2\pi q}{Q}\right] \qquad (3\text{-}5)$$

and substituting for $\bar{n}_{q,p}$ gives

$$\overline{C_{2m}} = -\frac{\tau}{2}\frac{\rho_p}{Q}(-1)^m J_{2m}\left(\frac{2\pi b\theta}{\lambda}\right)\mathrm{sinc}\left(\frac{2\pi m}{Q}\right)\cos(2m\phi) \qquad (3\text{-}6)$$

$$\overline{S_{2m}} = -\frac{\tau}{2}\frac{\rho_p}{Q}(-1)^m J_{2m}\left(\frac{2\pi b\theta}{\lambda}\right)\mathrm{sinc}\left(\frac{2\pi m}{Q}\right)\sin(2m\phi) \qquad (3\text{-}7)$$

$$A_{2m} = \sqrt{\bar{C}_{2m}^2 + \bar{S}_{2m}^2} = \frac{\tau}{2}\frac{\rho_p}{Q}\left| J_{2m}\left(\frac{2\pi b\theta}{\lambda}\right) \mathrm{sinc}\left(\frac{2\pi m}{Q}\right)\right| \quad (3\text{-}8)$$

The signal-to-noise ratio is

$$(S/N)_{2m} = \sqrt{\bar{C}_{2m}^2/\sigma_{C_{2m}}^2 + \bar{S}_{2m}^2/\sigma_{S_{2m}}^2} = A_{2m}/\sigma_{C_{2m}} \quad (3\text{-}9)$$

where

$$\sigma_{C_{2m}}^2 = \sigma_{S_{2m}}^2 = \sigma_{2m}^2 = \frac{1}{Q^2}\left[\sum_{(q)} (n_{q,2} - \bar{n}_{q,2}) \cos\left(2m\frac{2\pi q}{Q}\right)\right]^2 \quad (3\text{-}10)$$

Assuming the n_q Poisson distributed,

$$\sigma_{2m}^2 = \frac{1}{Q^2}\sum_{(q)} \bar{n}_{q,2}\cos^2\left(2m\frac{2\pi q}{Q}\right) = \tau\rho_z/2Q^2 \quad (3\text{-}11)$$

Thus

$$(S/N)_{2m} = \frac{\rho_p}{\sqrt{2\rho_z}}\left|J_{2m}\left(\frac{2\pi b\theta}{\lambda}\right)\mathrm{sinc}\left(\frac{2\pi m}{Q}\right)\right|\cdot\sqrt{t} \quad (3\text{-}12)$$

where t is the observation (sensor integration) time. R_p is equal to the rate of planet photons into both sensor apertures whereas R_z is that of zodiacal photons to one aperture only, because zodiacal light photons are equally divided between the two ports, and only 50% go to the null port. Therefore

$$\rho_p = 2\frac{\pi D^2}{4} F_p \tau\eta f\Delta\lambda; \qquad \rho_z = \frac{\pi D^2}{4} I_z \Delta\Omega\cdot\tau\eta\varepsilon\Delta\lambda \quad (3\text{-}13)$$

where F_p is the irradiance by the planet and I_z the radiance by the zodiacal light, η the quantum efficiency averaged over the bandwidth $\Delta\lambda$, ε a factor allowing for noise associated with processing the signal, $\Delta\Omega$ the detector solid angle, and f the fraction of planetary photons travelling to the focal plane and contained in $\Delta\Omega$. The thermal noise factor is

$$1 + \left[e^{hc/\lambda kT_s} - 1\right]^{-1} \approx 1.2 \quad (3\text{-}14)$$

there is a factor 2 for electron-hole recombination noise; and we shall allow a factor 2 to allow for residual noise (for instance, thermal radiation from optics, stray light, etc.) Thus $\varepsilon = 2\times2\times1.2 = 4.8$. Now

$$f/\Delta\Omega \approx \frac{1}{\sqrt{\pi}} D/\lambda \quad (3\text{-}15)$$

Thus we have

$$(S/N)_{2m} \approx \frac{2\,\frac{\pi D^2}{4} F_p \left| J_{2m}\left(\frac{2\pi b\theta}{\lambda}\right) \mathrm{sinc}\left(\frac{2\pi m}{Q}\right)\right| \sqrt{T\eta t \cdot \Delta\lambda}}{\sqrt{2 \cdot \frac{\pi D^2}{4} I_z \cdot \pi \cdot \left(\frac{\lambda}{D}\right)^2 \cdot 4.8}} \tag{3-16}$$

For the standard planet

$$\begin{cases} F_p = 2.5 \text{ / sec/}\mu\text{m/m}^2 \\ I_z = 1.1 \times 10^{12} \text{/sec/}\mu\text{m/m}^2\text{/sr} \\ \lambda = 26\ \mu\text{m} \\ \Delta\lambda = 4\ \mu\text{m} \end{cases} \tag{3-17}$$

We find

$$(S/N)_{2m} = 0.059\, D^2 \left| J_{2m}\left(\frac{2\pi b\theta}{\lambda}\right) \mathrm{sinc}\left(\frac{2\pi m}{Q}\right)\right| \sqrt{T\eta t} \tag{3-18}$$

where D in meters and t in seconds. Various values of sinc(2 m/Q) are given in Table 3-1. The Bessel functions J_2, J_4 and J_6 are plotted in Fig. 3-4 .

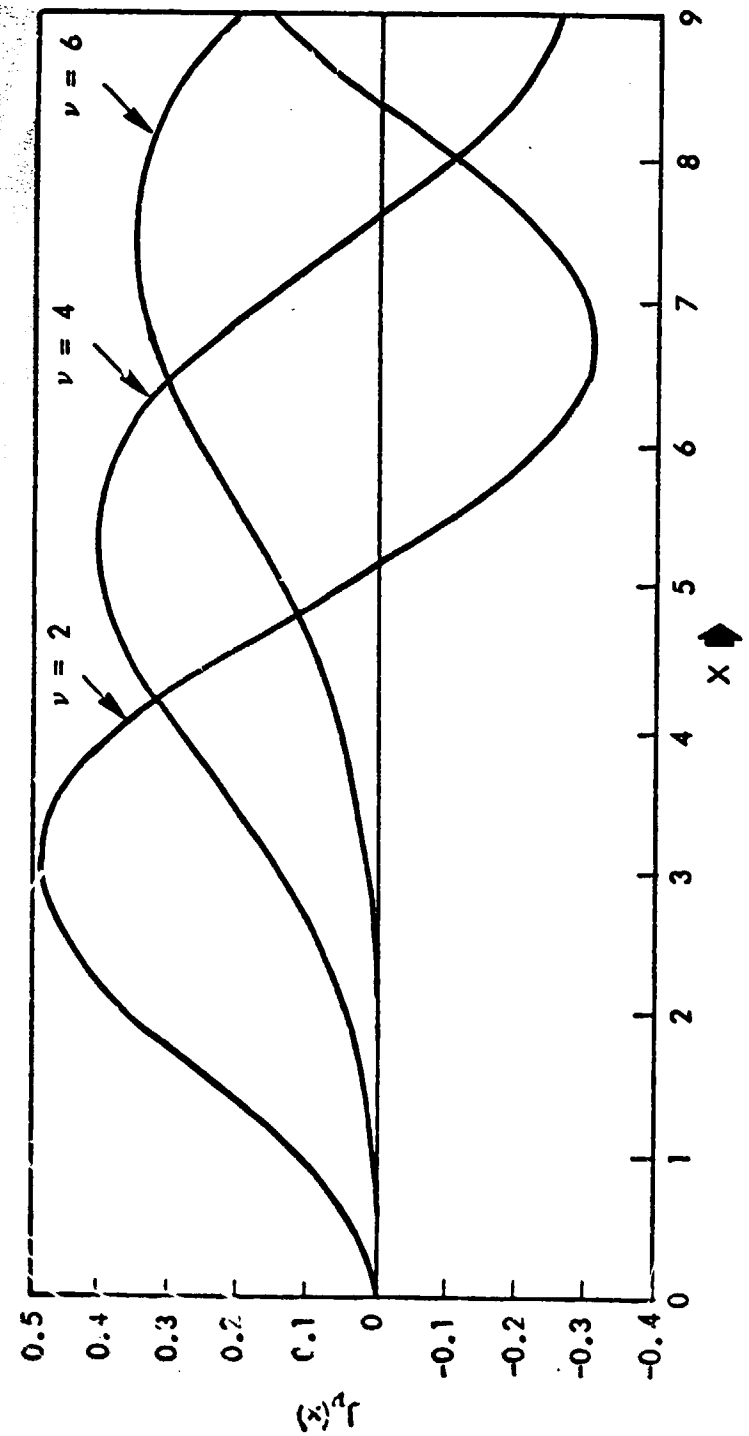

Fig. 3-4 Some Bessel Functions

Table 3-1

VALUES OF sinc $(2\pi m/Q)$

	m = 2	4	6	8
Q = 4	0	0	0	0
8	.64	0	-.21	0
16	.90	.64	.30	0
32	.97	.90	.78	.64
64	.99	.97	.94	.90

3.4 Detection: Definition and Criteria

We take detection to mean: determining the presence of a point-like object near a candidate star, with an angular separation from that star and a spectral brightness appropriate for a planet. Clearly, following detection, additional evidence must be obtained to show that the object is indeed a planet and not another object unrelated to the star. IRIS can obtain the evidence either by tracing the object's path relative to the star and calculating an orbit or by measuring the object's temperature. Either method is not foolproof but can be taken in support of the other. As examples: the orbit determination in a given case may not be accurate enough to distinguish between a curve and a straight line (see Sec. 3-8); the temperature of the planet (assuming it is indeed a planet) may be unrelated to the distance from its parent star, while we assumed temperature $\propto$ (distance)$^{-\frac{1}{2}}$.

In a limited sense, IRIS has an advantage over APOTS in two respects: (1) it can measure temperature, while APOTS cannot; (2) the infrared brightness of the planet does not change (noticeably) with orbit phase (except if the planet is blocked by the star disk), whereas brightness in the visible does, and very much so. The brightness of the planet when it moves toward the front of the star is much reduced, the separation also; and thus the detection probability even more so. We refer to the relevant section in the APOTS report (Vol. II). On the other hand, the variation with phase can be considered an advantage because it can be taken as hard-to-dismiss evidence for the object's being a planet.

We postulate that detection occurs when the S/N ratio in any sensor channel (each harmonic can be considered a separate channel) exceeds a set threshold determined by the fixed observation time interval. The threshold is determined by the required detection confidence, which, in turn, is set by assumed values of the missed detection and false alarm rates. A reasonable false alarm rate is allowed since the sensor can look again. The number of primary targets (e.g. stars within 10 parsecs and magnitude less than 6) is relatively small, and time is not a critical parameter in this experiment. By contrast, the number of missed detections should be small since a few missed detections in a limited

sample will skew the calculated planetary statistics and may result in program failure: after all, it is one mission objective of IRIS to accumulate preliminary planet statistics.

The false alarm probability P_{FA} per observation interval is set at 10% (i.e., this requires three extra "looks" for every 30 stars). The probability of missed detection, P_{MD}, is 1%. The signal in an IRIS sensor channel is the amplitude of the planetary harmonic, A_{2m}, where

$$A_{2m}^2 = C_{2m}^2 + S_{2m}^2 \tag{3-19}$$

We shall for the moment drop the cumbersome subscript 2m. Suppose the C and S are normally distributed, with the same variance and different averages,

$$f(C) = \frac{1}{\sqrt{2\pi}\sigma} e^{-(C-\bar{C})^2/2\sigma^2} \tag{3-20a}$$

and

$$f(S) = \frac{1}{\sqrt{2\pi}\sigma} e^{-(S-\bar{S})^2/2\sigma^2} \tag{3-20b}$$

The distribution function of A is

$$F(A) = \frac{1}{2\pi\sigma^2} \iint e^{-\frac{(C-\bar{C})^2+(S-\bar{S})^2}{2\sigma^2}} dC\,dS \tag{3-21}$$

$$= \frac{1}{\sigma^2} \int_0^A e^{-\frac{r^2+\rho^2}{2\sigma^2}} I_0\left(\frac{r\rho}{\sigma^2}\right) r\,dr$$

where I_0 represents the modified Bessel function of order zero. Letting

$$x = r/\sigma \tag{3-22}$$

and

$$y = \rho/\sigma = (S/N) \tag{3-23}$$

we write

$$F(A) = \int_0^{A/\sigma} e^{-\frac{x^2+y^2}{2}} I_0(xy)\, x\,dx \tag{3-24}$$

Now, $F(A) = P_{MD}$, and

$$P_{FA} = \int_{A/\sigma}^{\infty} e^{-x^2/2}\, x\,dx = e^{-A^2/2\sigma^2} \tag{3-25}$$

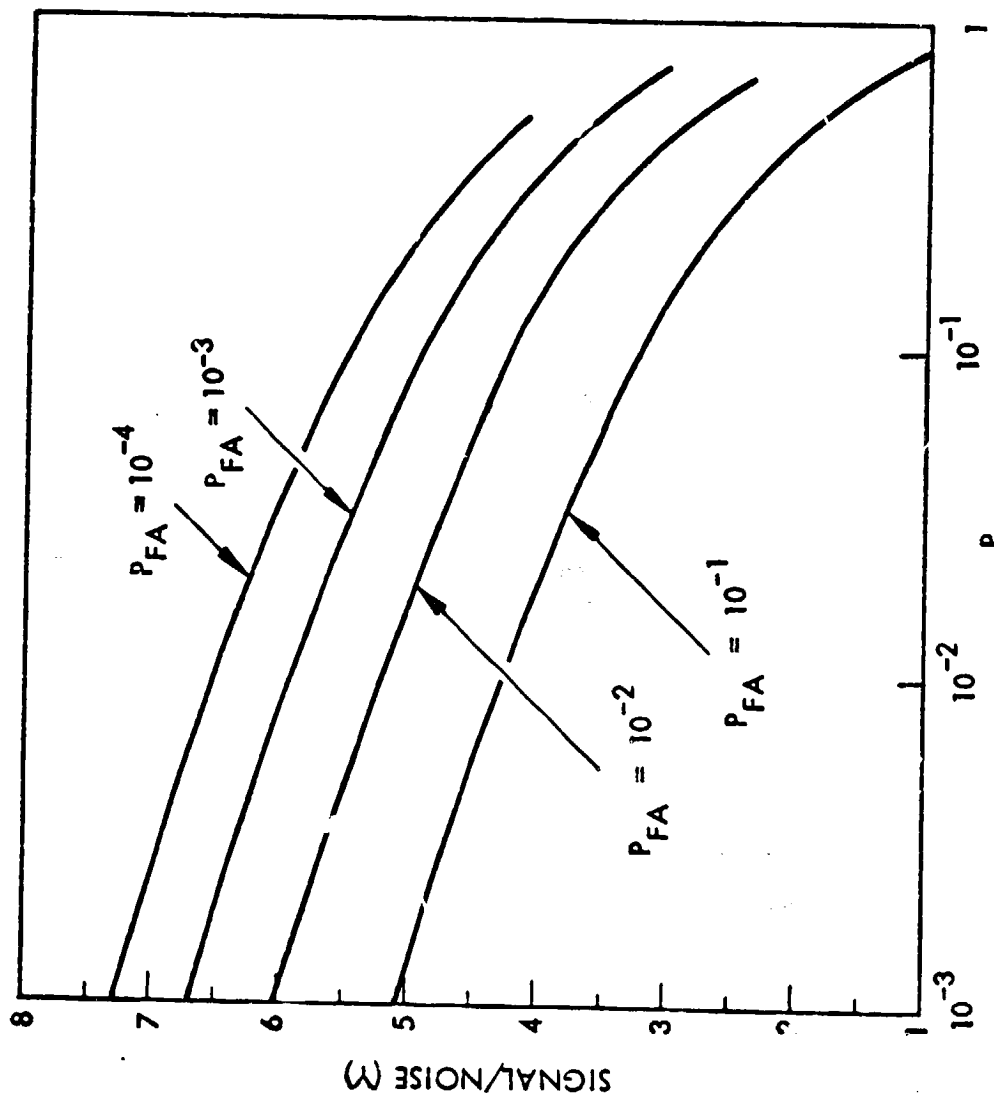

Fig. 3-5 Interrelations: Signal-To-Noise Ratio, Probabilities of False Alarm and Missed Detection

Now, y is equivalent to S/N. Fig. 3-5 shows how the required value of S/N depends on the values of P_{FA} and P_{MD}. (In our case, we find S/N = 4.3.)

If two channels are used simultaneously, for example the 2nd and 4th harmonic signal components, then we have

$$P_{MD} = P_{MD1} \cdot P_{MD2} \tag{3-26}$$

and

$$P_{FA} = P_{FA1} + P_{FA2} - P_{FA1} P_{FA2} \tag{3-27}$$

For $P_{FA} = 0.1$

$$P_{FA1} = P_{FA2} \simeq 0.051 \tag{3-28}$$

Furthermore

$$P_{MD} = 0.01 = \int_0^{\sqrt{2\ln(1/0.051)}} x\,dx\, I_0(xy_1)\, e^{-\frac{x^2+y_1^2}{2}} \cdot \int_0^{\sqrt{2\ln(1/0.051)}} x\,dx\, I_0(xy_2)\, e^{-\frac{x^2+y_2^2}{2}} \tag{3-29}$$

Fig. 3-6 shows how y, and y_2 are related for fixed values of $P_{FA} = 0.1$ and $P_{MD} = 0.01$. If N channels are used simultaneously,

$$P_{MD} = \prod_{i=1}^{N} \left\{ \int_0^{\sqrt{2\ln(N/P_{FA})}} x\,dx\, e^{-\frac{x^2+y_i^2}{2}} I_0(xy_i) \right. \tag{3-30}$$

planet detection is equivalent to the detection of weak radar echoes submerged in noise. This allows us to use the radar equations in the manner above, to estimate the false alarm and missed detection probabilities in one or more channels. These channels, which are the various harmonics, are considered to be independent since it is not possible to predict their relative strengths without knowing a priori the planet-star separation (θ).

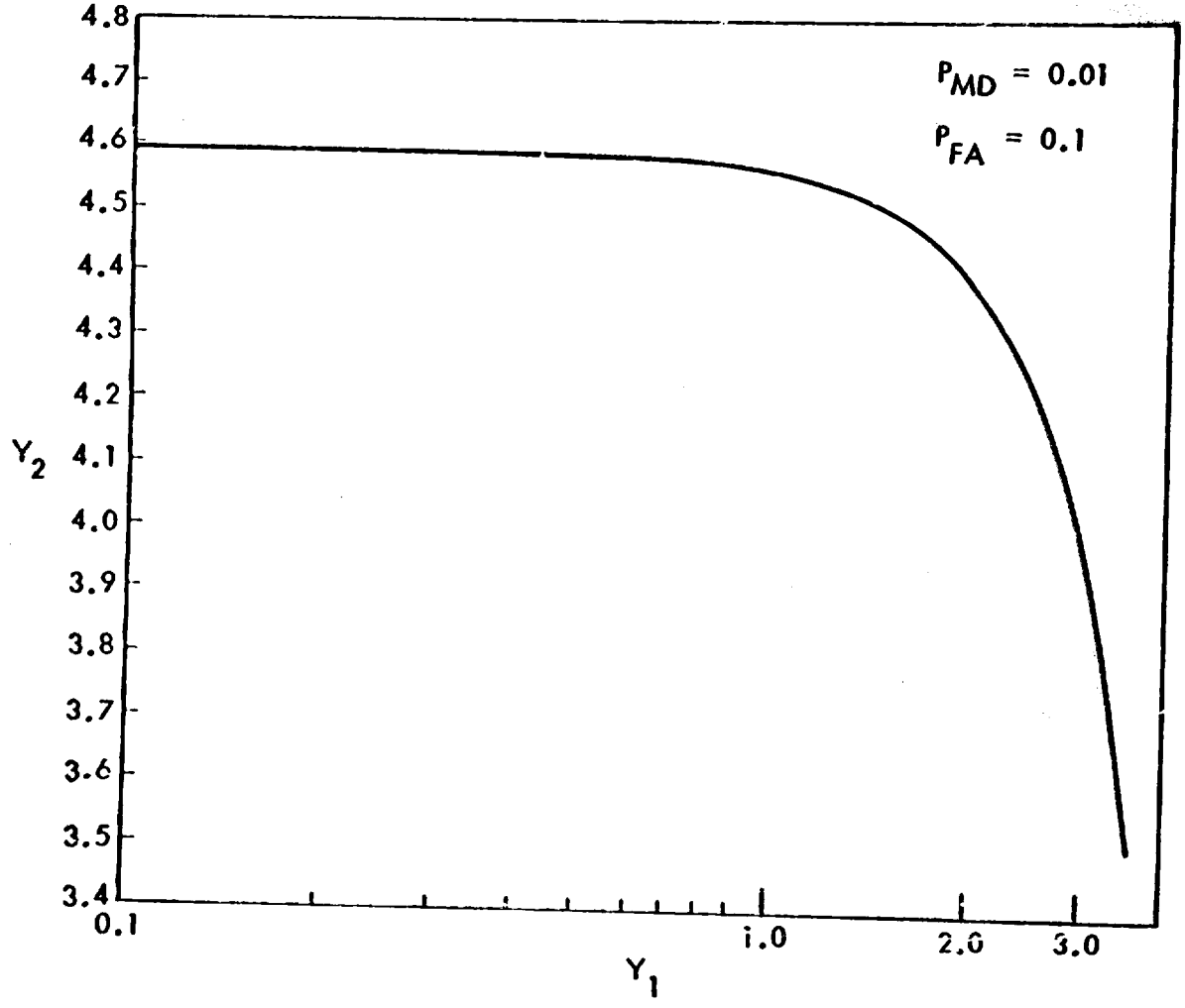

Fig. 3-6 Signal-to-Noise Relations for 2-Channel Detection

3.5 Choice of Interferometer Baseline

The observation time necessary for the detection of the standard planet using a single channel, the 2m-th harmonic of the planet signal, can be written in the normalized form

$$t_{2m}(\text{sec}) = 2.9\times10^{2}\,[T\eta]^{-1}(S/N)^{2}_{2m}\,\chi_{2m}\,D^{-4} \qquad (3\text{-}31)$$

where D is in meters and where

$$\chi_{2m} = \left|J_{2m}\left(\frac{2\pi b\theta}{\lambda}\right)\text{sinc}\left(\frac{2m\pi}{Q}\right)\right|^{-2} \qquad (3\text{-}32)$$

We assume that at least three channels will be used and will carry through the analysis for that case (there is no reason why not many harmonics can be used, except the required value of Q and the signal processing demands become greater and greater, with rapidly diminishing advantages). Then we can write (see Appendix C)

$$t \approx \left[t_2^{-1} + t_4^{-1} + t_6^{-1} + \cdots\right]^{-1} \qquad (3\text{-}33)$$

where

$$t_{2m} \propto \left|J_{2m}\left(\frac{2\pi b\theta}{\lambda}\right)\right|^{-2} \qquad (3\text{-}34)$$

since for sufficiently large values of Q, $\text{sinc}\left(\frac{2\pi m}{Q}\right) \approx 1$.

The expression

$$\left[J_2^2 + J_4^2 + J_6^2\right]^{-1}$$

is plotted in Fig. 3-7, along with J_2^2, and J_4^2 and J_6^2, as a function of $(2\pi b\theta/\lambda)$. The function has two pronounced minima at $\frac{2\pi b\theta}{\lambda}$ = 3.2 and 6.4. If we choose the baseline b=13m then the minimum at 6.4 falls exactly on θ=2.0 μrad. Therefore, the observation time for the standard planet is minimized. This would also be true for choosing the minimum at 3.2 (which would give b=6.5m). However, the choice of b=13m has these advantages:

1. The AC planet signal is large and contains significant 4th and 6th harmonic. Mispointing the optical axis, which due to a time-varying null error on the star, introduces a significant amount of 2nd harmonic signal (only a very small amount of 4th harmonic signal), has a much smaller deliterious effect, than the minimum at 3.2, which is mostly 2nd harmonic and is thus vulnerable to mispointing.

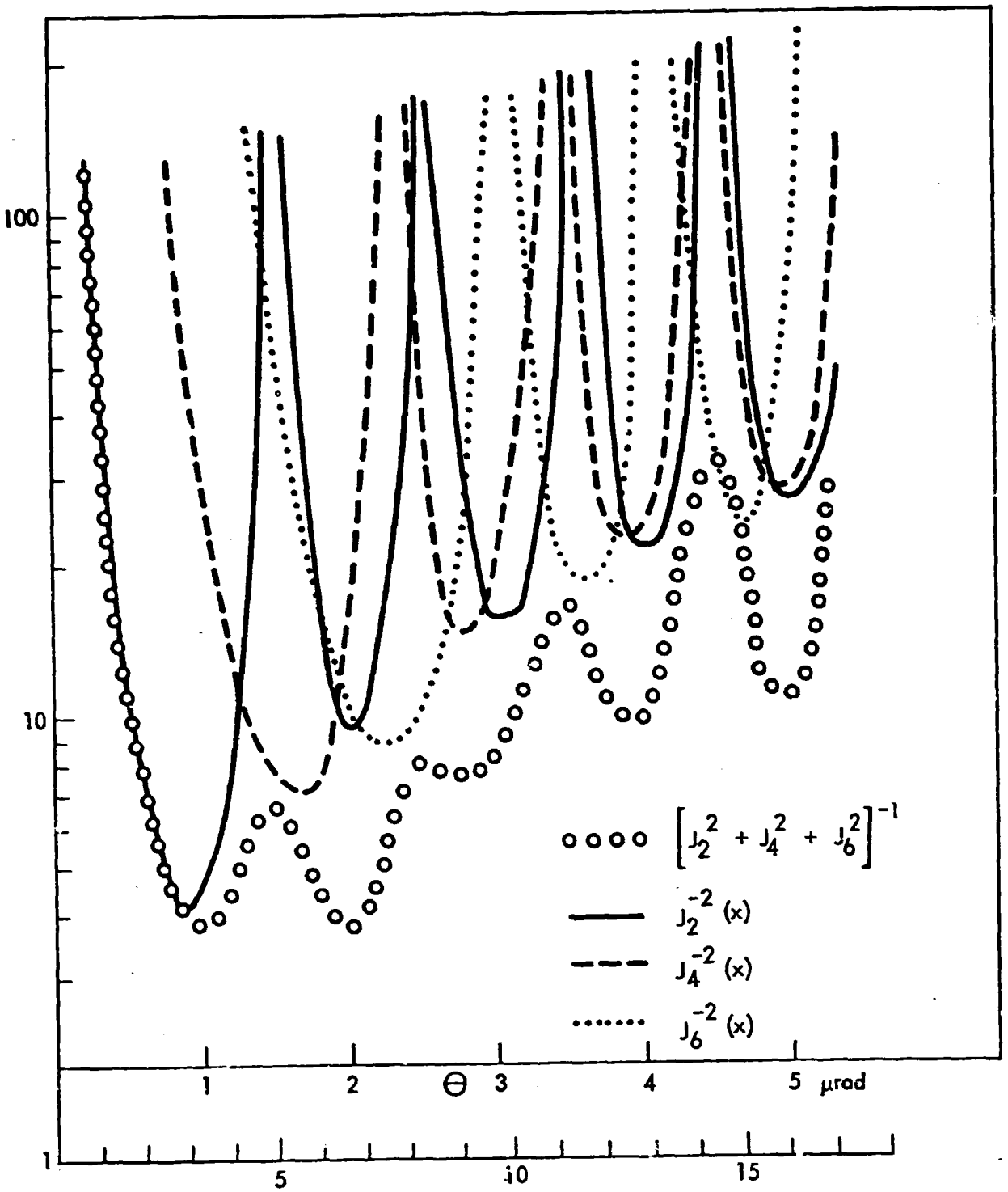

Fig. 3-7 (See Sec. 3-5)

2. If the interferometer is well-pointed, planets half as close to the parent star than the standard planet can still be detected with small observation times. The choice therefore offers a certain amount of flexibility.

3. A baseline length of b=6.5 m would seem to suggest a more managable system as a whole (particularly dynamically). However, the problems of accurate pointing and baseline control are basically the same at 13 m, and we see no obvious advantage in a smaller baseline.

The choice b=26 m would double the resolution capability of IRIS. However, such a system would require telescoping the main structure which could seriously compromise the fesibility .

In conclusion, we see no advantage in choosing a much smaller or larger value for the interferometer baseline. An IRIS with a 13 m baseline also fits the shuttle bay and is thus conveninent.

3.6 Observation Time for Standard Planet

With a nominal (and reasonably realistic) value of

$$T\eta = 0.1 \tag{3-35}$$

the observation time for detection of the standard planet, when using the three lowest harmonics, is

$$t_o = 0.9 \text{ hours} \tag{3-36}$$

which is the same as for the apodized telescope with D=3 m and μ=6 (APOTS 6). However, APOTS 6 is only realizable with a major and unlikely breakthrough in wavefront control (as well as mirror technology). For a more realistic APOTS 2 we have t_o = 100 hours. Therefore, IRIS is by about two orders of magnitude "faster" than a feasible APOTS.

3.7 Parameter Sensitivity of Observation Time

We discuss the dependence of observation time t on the key parameters D (mirror diamater), θ (star-planet separation), d (distance to star), $\acute{d}$ (radius of planet orbit), and stellar magnitude, M.

3.7.1 Dependence on D (Fig. 3-8)

For a background-limited sensor, $S/N \propto D^2$. Since $t \propto (S/N)^{-2}$, we have $t \propto D^{-4}$. By contrast, for APOTS the dependence depends on apodization: for APOTS 2, $t \propto D^{-5}$, and for APOTS 6, $t \propto D^{-9}$.

3.7.2 Dependence on θ (Fig. 3-8)

(We assume that when θ is varied, the planetary and stellar brightnesses remain constant). The resulting variation of t with θ is similar to that shown in Fig. 3-7, but the units of the ordinate in that figure would be different. The undulatory behavior of the variation derives from the Bessel functions.

For $\theta \ll 1$, we have $t \propto J_2^{-2} \propto \theta^{-4}$; and for $0.7 < \theta < 2.0$ μrad, t <1 hour.

3.7.3 Dependence on d (Fig. 3-8)

As d is increased, the brightnes of the planet decreases in proportion to d^{-2}, and θ decreases proportional to d^{-1}. The observation time therefore in= creases propotional to d^8.

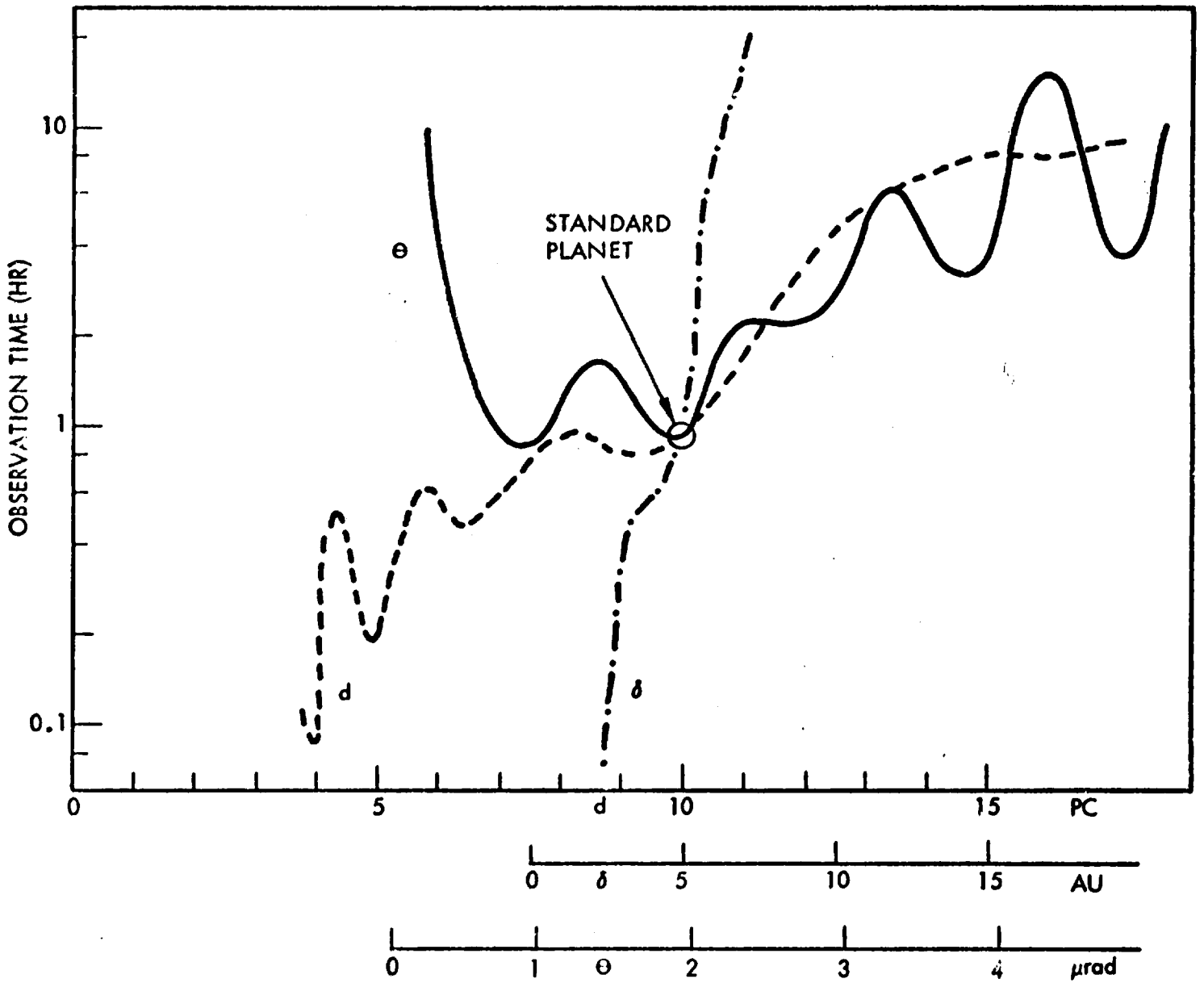

Fig. 3-8 Parameter Dependence of IRIS Observation Time

3.7.4 Dependence on δ (Fig. 3-8)

As δ is increased, the angular separation θ increases in proportion to it. However, the dominant change in t derives from the decrease in planetary temperature if we assume: temperature $\propto \delta^{-1/2}$ (no internal heat source, which may be unrealistic in some cases). The relationship between t and δ is therefore approximately exponential. If internal heat sources determine the planet's temperature, the observation time will vary with δ as in Fig. 3-8 for the variation with θ.

3.7.5 Dependence on M (Fig. 3-9)

In ths parameter variation we hold the values of D, θ, d and δ constant. We assume the relation

$$\text{Brightness} \propto \exp(-\text{const. } M)$$

and then find an exponential variation of t with M.

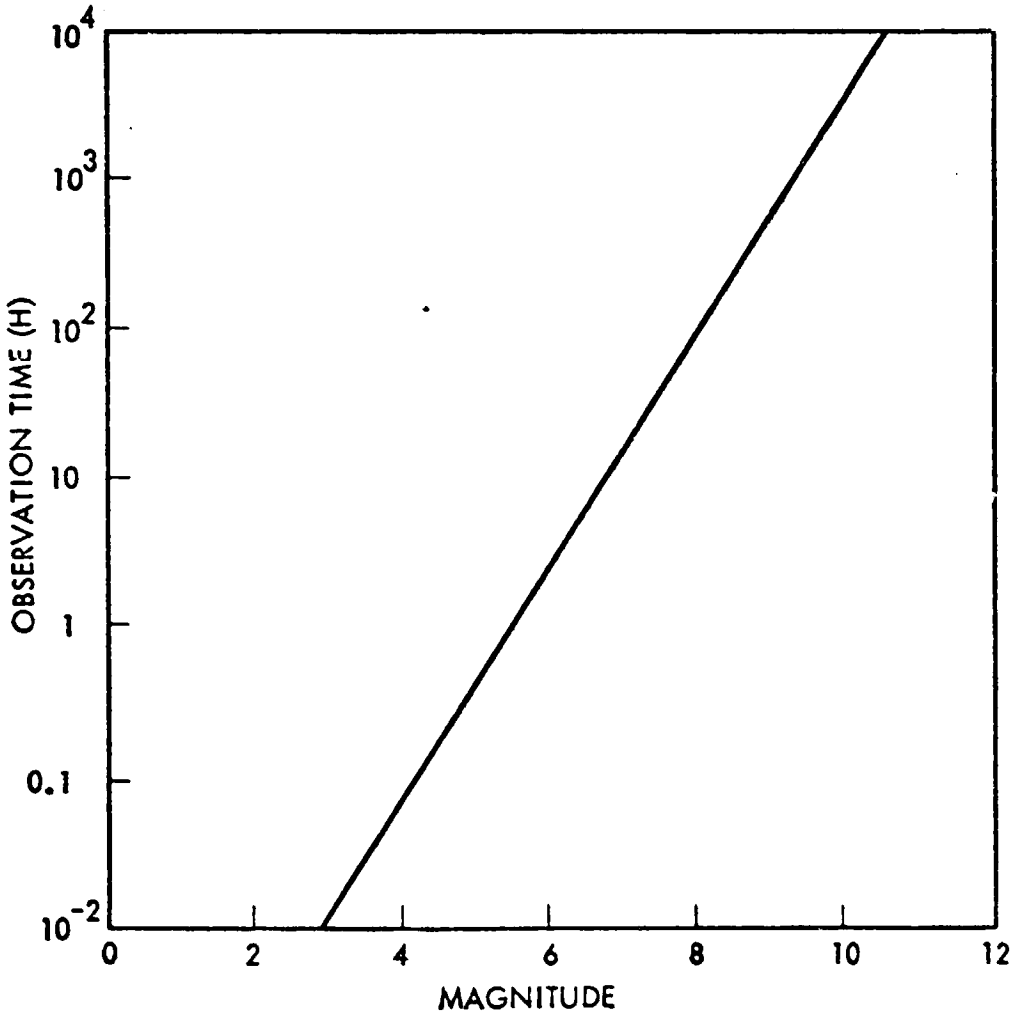

Fig. 3-9 Dependence of Observation Time on Magnitude of Parent Star

Table 3-2

PARAMETER SENSITIVITY OF IRIS OBSERVATION TIME

Angular separation, θ	θ^{-4} for $\theta \ll 1$ μrad
Distance, d	d^{δ} for $d \geq 30$ pc
Orbit radius, $\acute{o}$	exponential
Planet radius, R	R^{-4}
Mirror diameter, D	D^{-4}
Stellar magnitude, M	exponential

3.8 Planet Verification

3.8.1 "Imposter" Star

Following detection as defined earlier, evidence must be obtained to verify that the discovered object near the observed star is indeed a planet of that star. It could also be another point-like IR source, including a faint star. We shall make a simple calculation to estimate the chances that it is indeed another star. The probability is that of having another star within 2 μrad of any one star, with an in-band photon flux to the sensor equal to that from the baseline standard planet. In the following, the subscript s refers to that star, p to the standard planet. Then for a star to be an "imposter" we must have

$$\frac{\Omega_s}{e^{hc/\lambda kT_s}-1} = \frac{\Omega_p}{e^{hc/\lambda kT_p}-1} \tag{3-38}$$

Since $hc/\lambda kT_s \ll 1$,

$$\Omega_s T_s \approx \frac{hc}{\lambda k} \frac{\Omega_p}{e^{hc/\lambda kT_p}-1} \tag{3-39}$$

For λ = 26 μm and $T_p = 125^\circ$ K, the RHS of (3-37) is equal to 1.1×10^{-18} (sr.°K). The apparent (bolometric) brightness of the star, B_s, is

$$\pi B_s = \sigma T_s^4 \Omega_s \tag{3-40}$$

σ being Stefan's constant. Also

$$B_s = 10^{-m_s/2.5}\ 2.6\times10^{-8}\ \frac{\text{watt}}{m^2} \tag{3-41}$$

m_s being the bolometric magnitude of the star. Combining these results we have

$$T_s^3\, 10^{m_s/2.5} = \frac{\pi \cdot 2.6\times10^{-8}\lambda k}{\sigma hc} \frac{e^{hc/\lambda kT_p}-1}{\Omega_p} \tag{3-42}$$

The RHS of the last equation is ~1.3×10^{18}; thus

$$m_s \approx 45 - 7.5 \log(T_s) . \qquad (3\text{-}43)$$

Table 3-3

SPECTRAL DISTRIBUTION OF STARS

Spectral Class	$\log(T_s)$	Bolometric magnitude, m_s	Visual magnitude	%(1)	N(2)	%N(3)
O	(4.7)-4.44	(9.8)-11.7	14.5	-	-	-
B	4.44-4.00	11.7-15.0	14.5-15.5	.10	813	81
A	4.00-3.87	15.0-16.0	15.5-16.0	.22	1200	270
F	3.87-3.78	16.0-16.7	16.0-16.7	.19	1200	230
G	3.78-3.69	16.7-17.3	16.7-17.5	.14	2500	390
K	3.69-3.54	17.3-18.5	17.5-19.7	.31	10^4	3100
M	3.54-(3.3)	18.5-20.2	19.7-(23)	.03	10^5	3000?
					Total	~7000?

(1) fraction of all stars
(2) stars per deg^2, of all types in that magn. range
(3) stars per deg^2, of this type in that magn. range

Eq. (3-43) confirms what seems inevitable - that cool, faint stars simulate a planet best, e.g. faint K and M stars. Table (3-3) gives the estimated number of stars in each spectral class (average between galactic equator and poles) based on data in Allen's Astrophysical Quantities. Due to the uncertainty of the number of cool, faint stars, no firm conclusion can be drawn about the possibility of stellar "imposters". Table (3-3) would seem to suggest it is low.

IRIS has the capability of measuring temperature as well as determining an orbit. In Sec. 2-5 a best value for the observations at a secondary wavelength was derived. Simultaneous measurements at 26 and 18 μm should yield a rough estimate of the object's temperature. This may be surest way of ascertaining a discovered object's nature. We now discuss orbit determination.

3.8.2 Orbit Determination

3.8.2.1 Method

For an orbit determination, IRIS must measure at least three positions of the planet with sufficient accuracy, in a reference frame fixed on the parent star. The assumed experiment life time, 5 years, is insufficient for complete orbit tracing of the standard planet (12 years required). But that should not be necessary.

As a first attempt at determining whether the discovered object is bound to the parent star, we suppose that the measured positions distinguish between a straight-line motion and a curved motion. Suppose that the orbit is perpendicular to the line-of-sight; that the three measurements are made at regular time intervals; and that the arc spanning the three observations subtends an angle $\emptyset$ at the star. Each measurement is uncertain in position by the amount Δ. If arc and straight line are separated by more than $(\theta\Delta)$ at their greatest separation, we conclude that the path is curved and that the object is bound. This requires

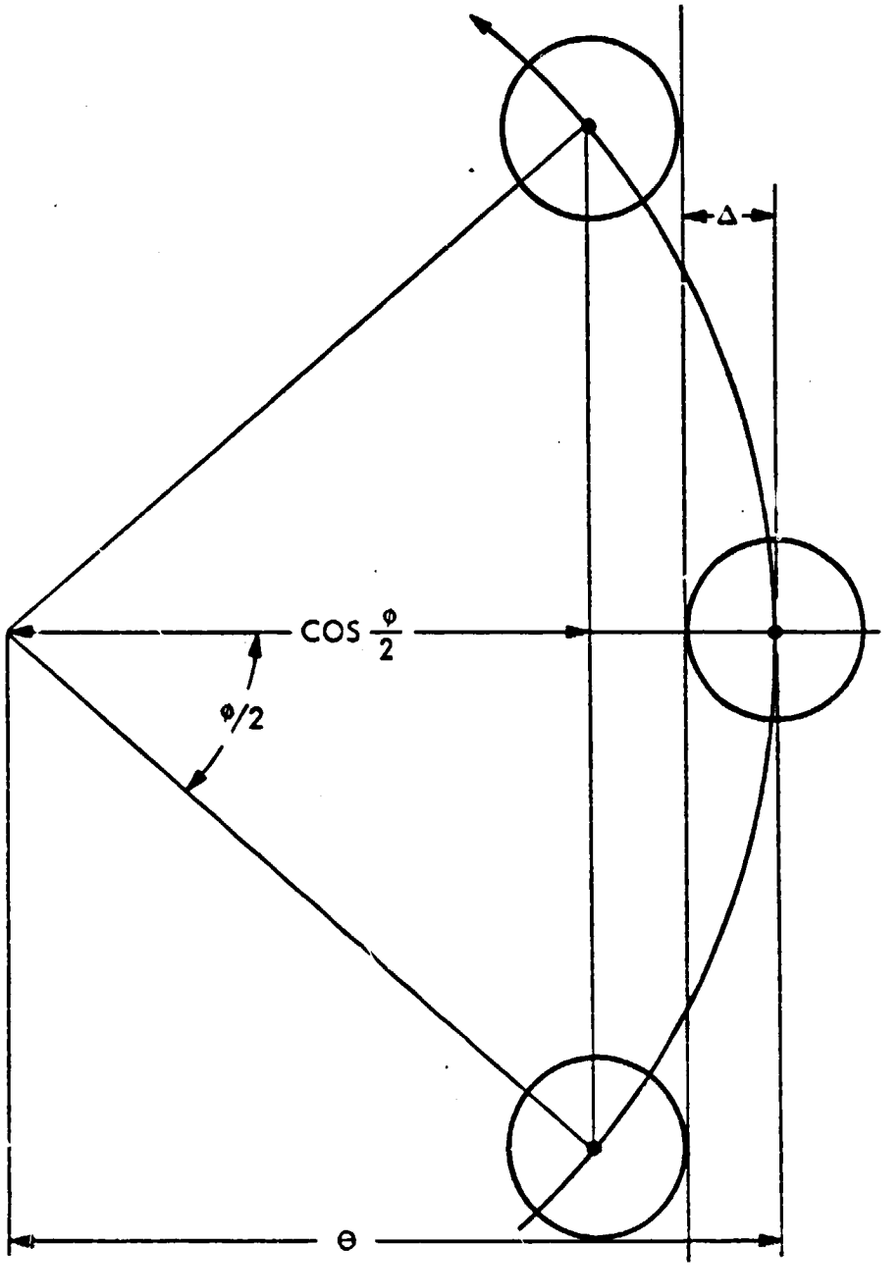

Fig. 3-10 On Orbit Determination

$$\Delta < \frac{\theta}{2}\left[1-\cos(\phi/2)\right]. \qquad (3\text{-}44)$$

For the standard planet, θ = 2.5 μrad. Table 3-4 shows the required accuracy in position, Δ, as a function of ϕ, and the time interval between the first and last observation.

Because of the 180° uncertainty in the determined azimuth (Sec. 3-1), the observations of the standard planet should cover no more than (1/4) of the orbit. Hence, Δ < 0.38 μrad is required.

The calculated uncertainty in position is given by

$$\Delta = \sqrt{(\Delta\theta)^2 + (\theta\,\Delta\phi)^2} \qquad (3\text{-}45)$$

where θ and ϕ are the uncertainties in angular separation (radial coordinate) and azimuth, respectively. (The 180° uncertainty in azimuth discussed in Sec. 3-1 is not included.)

3.8.2.2 Azimuthal Coordinate, ϕ

Suppose the harmonics 2m (m=1, 2, ..) are used to calculate the mean value of ϕ; then

$$\bar{\phi} = \frac{\sum_{(m)} \phi_{2m} \cdot (S/N)_{2m}}{\sum_{(m)} (S/N)_{2m}} \qquad (3\text{-}46)$$

The S/N values for the various measurements are the weights. Therefore, the mean value of $\Delta\phi$ is

$$\overline{\Delta\phi} = \frac{\sqrt{\sum_{(m)} (\Delta\phi)^2_{2m} (S/N)^2_{2m}}}{\sum_{(m)} (S/N)_{2m}} \qquad (3\text{-}47)$$

Now

$$\tan(2m\phi_{2m}) = \bar{S}_{2m}/\bar{C}_{2m} \qquad (3\text{-}48)$$

where $\bar{S}_{2m}$ and $\bar{C}_{2m}$ are the amplitudes of the 2mth harmonic, as discussed in Sec. 3-3.

Differentiation of $\tan(2m\,\phi_{2m})$ gives

$$2m\,\Delta\phi_{2m} = \left|\cos(2m\phi_{2m})\sin(2m\phi_{2m})\right| \cdot \sqrt{\frac{\Delta S_{2m}^2}{S_{2m}^2} + \frac{\Delta C_{2m}^2}{C_{2m}^2}} \qquad (3\text{-}49)$$

Assuming $\Delta S_{2m}^2 = \Delta C_{2m}^2 = \sigma_{2m}^2$ and

$$\sigma_{2m} \Big/ \sqrt{C_{2m}^2 + S_{2m}^2} = (S/N)_{2m} \qquad (3\text{-}50)$$

we find

$$\Delta\phi_{2m} = \frac{1}{2m}\,(S/N)_{2m}^{-1} \qquad (3\text{-}51)$$

Substituting this result into Equ. (3-47) gives

$$\overline{\Delta\phi} = \frac{\sqrt{\sum_{(m)} (1/2m)^2}}{\sum_{(m)} (S/N)_{2m}} \qquad (3\text{-}52)$$

Since $\sum$ S/N≈5, we have $\Delta\phi \approx 6^{\circ}$ (0.1μrad); thus $\Delta\phi \simeq 0.2$ μrad.

Table 3-4

REQUIRED POSITION ACCURACY OF THE STANDARD PLANET

ϕ (deg)	10	30	60	90	152
T (years)	0.33	0.98	2.0	3.0	5.0
Δ (μrad)	0.0049	0.044	0.17	0.38	0.99

3.8.2.3 Radial Coordinate, θ

Analogous to (3-52) we have

$$\overline{\Delta\theta} = \sqrt{\sum_{(m)} (\Delta\theta)_{2m}^2 (S/N)_{2m}^2} \Big/ \sum_{(m)} (S/N)_{2m} \qquad (3\text{-}54)$$

Now differentiation of Eq. (3-16) gives

$$(\Delta\theta)_{2m} = (S/N)_{2m}^{-1} \frac{\lambda}{2\pi b} \left| \frac{J_{2m}\left(\frac{2\pi b\theta}{\lambda}\right)}{J'_{2m}\left(\frac{2\pi b\theta}{\lambda}\right)} \right| \qquad (3\text{-}55)$$

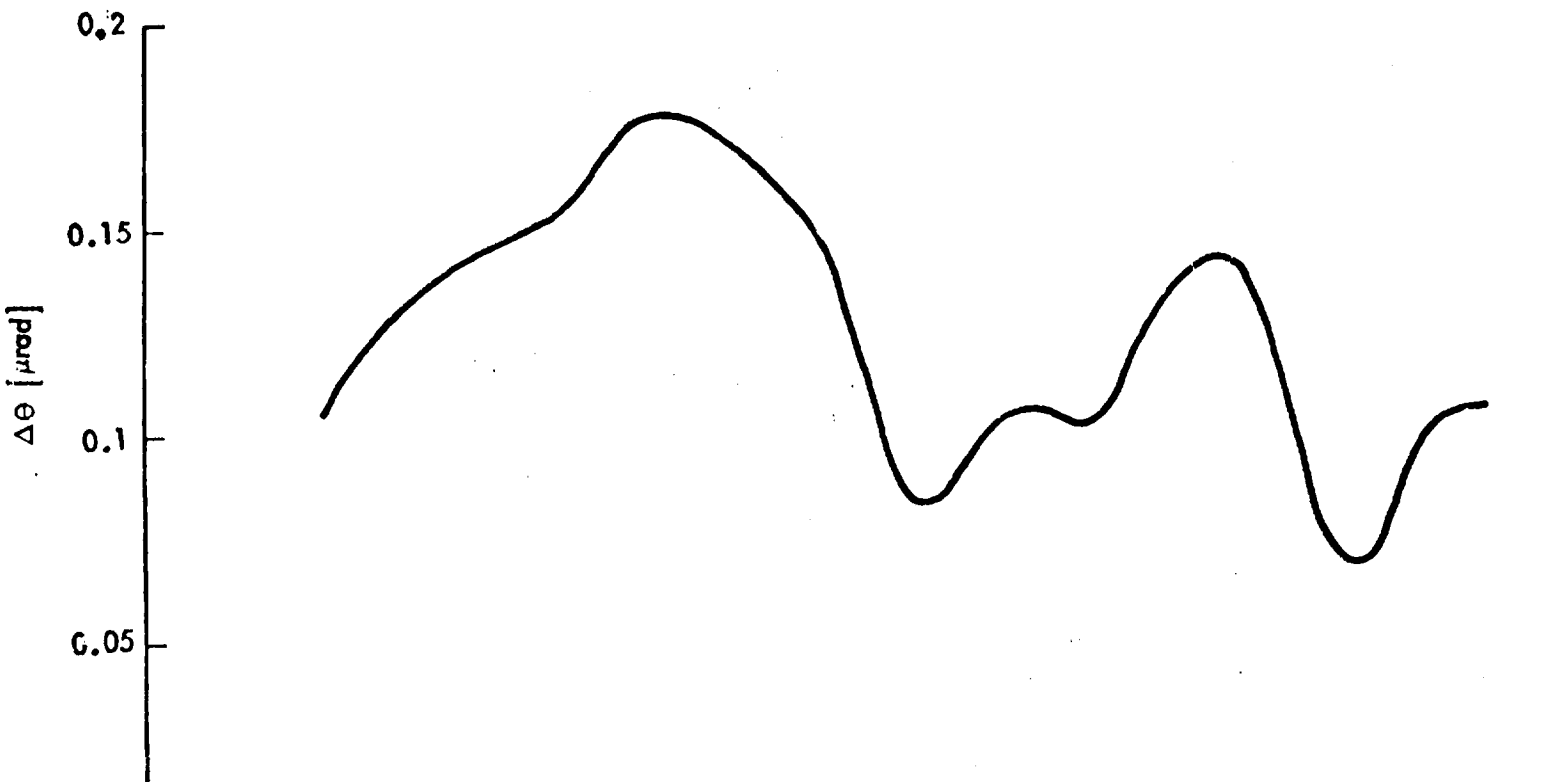

Fig. 3-11 Radial Position Error

but this expression does not present $(\Delta\theta)_{2m}$ when J'_{2m} is small. Clearly a second term in the Taylor expansion of $(\Delta\theta)_{2m}$ must also be used to calculate $(\Delta\theta)_{2m}$. This term alone gives

$$(\Delta\theta)_{2m} = 2\cdot(S/N)^{-1}_{2m}\cdot\sqrt{J_{2m}/J''_{2m}} \qquad (3\text{-}56)$$

Using both terms and letting $m=1$, $(S/N)_2=5$ we obtain the results shown in Fig.3-11. Very approximately, $\Delta\theta\simeq 0.2$ μrad at $\theta=2$ μrad. The total position measurement error for the standard planet is thus

$$\sqrt{(0.2\,\mu\text{rad})^2+(0.2\,\mu\text{rad})^2} \approx 0.3\,\mu\text{rad}. \qquad (3\text{-}57)$$

We conclude that without substantial increase in detection S/N, the measured position of the object is accurate enough to decide whether or not it is bound to the star.

The above estimates are somewhat pessimistic because repeated observations of the same (and already discovered) object will be made at significantly higher S/N (longer observation time) than necessary for detection, therefore the position will be determined with greater precision.

4. Performance Requirements

4.1 Realizability of Background Limited Performance

Extrinsic detectors (e.g., Ge:Cu and Si:Sb) are the only candidates to approach the sensitivity required for this application; neither intrinsic detectors (photovoltaics or photo conductors) nor bolometers can presently even remotely approach the required performance.

To illustrate the performance limitations of extrinsic photoconductors we will assume the three usually dominant noise sources; the background noise on an Airy disc area, the Johnson noise of the load or feedback resistor and the voltage noise of the excess noise component of a MOSFET or JET source follower. The typical operation of a low background detector requires a source follower after the detector for impedance matching followed by a transimpedance amplifier with feedback resistor, R_L, providing the load. Transimpedance operation is usually preferred over voltage mode operation because of increased frequency response (basically determined by the $R_L C_f$ time constant, where C_f is the small stray capacity across the feedback resistor $C_f \sim .1$ pf), constant detector bias and minimization from cross talk. We will illustrate the sensitivity limit, with a voltage mode analysis, which will give the same results but will more simply illustrate the important terms. Without derivation, the NEP'(watt/ Hz) of an extrinsic photoconductor with the three dominant noise sources is

$$NEP' = \frac{1.24}{\lambda_\mu \eta G} \left[4 e^2 \eta G^2 \varphi_{BFP} A_A + \frac{4 kT}{R_L} + \frac{(1+\omega^2 R_L^2 C_s^2)}{R_L^2} V_n^2 \right]^{\frac{1}{2}} \qquad (4\text{-}1)$$

$$NEP' = \frac{2.48 e}{\lambda_\mu \eta^{\frac{1}{2}}} (\varphi_{BFP} A_A)^{\frac{1}{2}} \left\{ 1 + \frac{1}{4 e^2 \eta G^2 \varphi_{BFP} A_A} \left[\frac{4 kT}{R_L} + \frac{(1+\omega^2 R_L^2 C_s^2)}{R_L^2} V_n^2 \right] \right\}^{\frac{1}{2}} \qquad (4\text{-}2)$$

where $\varphi_{BFP} A_A$ is the photon/sec background photon rate on an Airy disc area on the focal plane

λ_μ is the measurement wavelength in μm

η is the detector quantum efficiency

G is the photoconduction gain

T is the focal plane and feedback resistor temperature

R_L is the value of the feedback resistor

$\omega = 2\pi f$ is the radial frequency

C_s is the total input circuit capacitance due to strays, MOSFET, etc.

V_n is the noise voltage spectral density of the MOSFET or JFET $V/\sqrt{Hz}$

$e = 1.6 \times 10^{-19}$ clbs

$k = 1.38 \times 10^{-23}$ joule/K°

The term outside the brackets represents the background limited performance we have previously calculated; what we now want to illustrate are the conditions that must be met to reduce the Johnson and amplifier noise below the background generation-recombination component. Thus we will attempt the condition

$$\frac{1}{4 e^2 \eta G^2 \varphi_{BFP} A_A} \left[\frac{4 kT}{R_L} + \frac{(1 + \omega^2 R_L^2 C_s^2)}{R_L^2} V_n^2 \right] < 1 \quad (4\text{-}3)$$

Simplifying

$$\frac{5.4 \times 10^2}{G^2(\eta \varphi_{BFP} A_A)} \left[\frac{T}{R_{L_{12}}} + \frac{.018}{R_{L_{12}}^2} (1 + 40 R_{L_{12}}^2 C_{s_{pf}}^2 f^2) V_{n_{\mu v}}^2 \right] < 1 \quad (4\text{-}4)$$

where $R_{L_{12}}$ is the feedback resistor in units of $10^{12}\ \Omega$

$C_{s_{pf}}$ is the circuit capacity in pf

$V_{n_{\mu v}}$ is the voltage noise in $\mu v/\sqrt{Hz}$

The excess voltage noise spectral density of a MOSFET or JFET has the form

$$V_{n_{\mu v}} = \frac{\alpha_{uv}}{F^{\frac{1}{2}}} \quad (4\text{-}5)$$

This noise term dominates for f ≥ .01 Hz for both MOSFETS and JFETS up to f < 10^3 Hz and 10^2 Hz for MOSFETS and JFETS respectively - at frequencies higher than this the noise spectral density is white. For the zodiacal background limited condition we have

$$\eta \varphi_{BkP} A_A = (1.22)^2 10^{-8} \eta \eta_o \varphi_{BZ} \lambda_{\mu m}^2 \Delta\lambda_\mu \qquad (4\text{-}6)$$

$$= 1.5 \times 10^3$$

at $\lambda_\mu = 30$ and $\eta\eta_o = .1$, and $\Delta\lambda_\mu = 4$.

Thus we must satisfy $$\left[\frac{T}{R_{L_{12}}} + \frac{.018\,(1 + 40\, f^2 R_{L_{12}}^2 C_{s_{pf}}^2)\,\alpha_{\mu V}^2}{R_{L_{12}}^2 \quad f}\right] < 2.8\, G^2 \qquad (4\text{-}7)$$

The conventional approach is the use of MOSFETS on the focal plane; their noise is considerably higher than that of JFETS but they operate well at low temperatures and because of their proximity to the detectors the circuit capacity can be kept very low. JFETS, although having much lower noise can only be operated at T ≥ 100 K; thus the total circuit capacity will be correspondingly higher due to the long lead lengths required. The JFET approach is somewhat unconventional in current designs but for this application where amplifier noise is an important contribution it should be carefully considered.

To illustrate the magnitude involved in achieving background limited performance we will assume a very good state of the art MOSFET with $\alpha_{\mu V} = 0.3$ and by judicious circuit care a value of $C_{spf} \simeq 3$ should be attainable.

Thus we have for eq. (4-7)

$$\left[\frac{T}{R_{L_{12}}} + \frac{1.6 \times 10^{-3}}{f\, R_{L_{12}}^2}\,(1 + 360\, R_{L_{12}}^2 f^2)\right] < 2.8\, G^2 \qquad (4\text{-}8)$$

Since $R_{L_{12}} \gg 1$ is required to satisfy the Johnson noise term, we have that for f ≥ .03 Hz

$$\left(\frac{T}{R_{L_{12}}} + .58\ f\right) < 2.8\ \sigma^2 \qquad (4\text{-}9)$$

under low background conditions (defined by the condition that the detector dielectric relaxation time $\tau_p >> \frac{1}{2\pi f}$) the maximum photoconductive gain is G = 0.5. Under these conditions we have

$$\frac{T}{R_{L_{12}}} + .58\ f < .7 \qquad (4\text{-}10)$$

which shows that for $f \leq .3$ Hz the Johnson noise term is dominant. For a normal operating temperature of T ≈2 K a value of $R_L \approx 10^{13}\ \Omega$ will thus be required to approach background limited performance. It should be noted that this value of load resister is considerably lower than the detector resistance per se, as it must be. The focal plane backgrounds will be $\leq 10^7$ photon/cm^2 sec; since the detector resistance, R_D background flux, ϕ_B product for Si:XX and Ge:XX detectors is typically

$$R_D\phi_B \simeq 10^{23} \qquad \text{Si:XX}$$
$$\approx 10^{22} \qquad \text{Ge:XX}$$

the condition is satisfied.

Load resistors of this value are unconventional - current focal plane technology uses $R_L \leq 10^{11}\Omega$; larger values are difficult to obtain because of noise and uniformity problems but have been obtained and for this particular application can be fabricated. If necessary another photoconductor irradiated with a controlled background can serve as the load resistor.

In summary we can see a relatively well defined design space to provide a sensor background limited to an Airy disc confined earth orbit zodiacal light.

4.2 Stray Light Suppression

The sensitivity of the IRIS sensor was calculated assuming that the contribution to background from the sensor was equal to the zodiacal light background. We now investigate this assumption to determine the requirements which the assumption places on the sensor design. It will become apparent that these considerations will strongly affect the sensor design and technology issues but will not affect sensor feasibility.

The components of stray light considered are:

1) infrared emission of the optics
2) radiation from the sensor structure scattered non-specularly from the mirrors onto the detector noise is also addressed.

4.2.1 Optics Emission

The infrared emission from the primary optics must not compromise the zodiacal light-limited background performance of IRIS. We assume that the optics is viewed through the same solid angle as is the zodiacal light. If ε_M is the mirror emissivity and N the number of mirrors (primary plus secondary), T_M the mirror temperature, ε_z the zodiacal light emissivity, and

$$\varphi \equiv \frac{1}{e^{hc/\lambda kT} - 1} \tag{4-11}$$

then

$$N\varepsilon_M \varphi_M(\varphi_M + 1) \leq \varepsilon_z \varphi_z(\varphi_z + 1) \tag{4-12}$$

is required. Since

$$\varepsilon_z = 1.2 \times 10^{-7}/\lambda_{\mu m} \tag{4-13}$$

and $T_z = 300^\circ$ K and, furthermore,

$$hc/\lambda kT_M >> 1 \tag{4-14}$$

we can write

$$T_M \leq \frac{1.44\times10^4}{\lambda_{\mu m}} \left\{ \ln \left[\frac{\lambda N \varepsilon_M}{1.2\times10^{-7} \varphi_2(\varphi_2+1)} \right] \right\}^{-1} \quad (4\text{-}15)$$

The reults for T_M are shown in Fig. 4-1. The IR emission by the mirrors decreases very rapidly with decreasing temperature and is fairly insensitive to $(N\varepsilon_M)$. An operating temperature of 30°K or a few degrees less is indicated. Suitable cryogens are solid neon (typical T=14 °K) and solid hydrogen (typical T= 10°K).

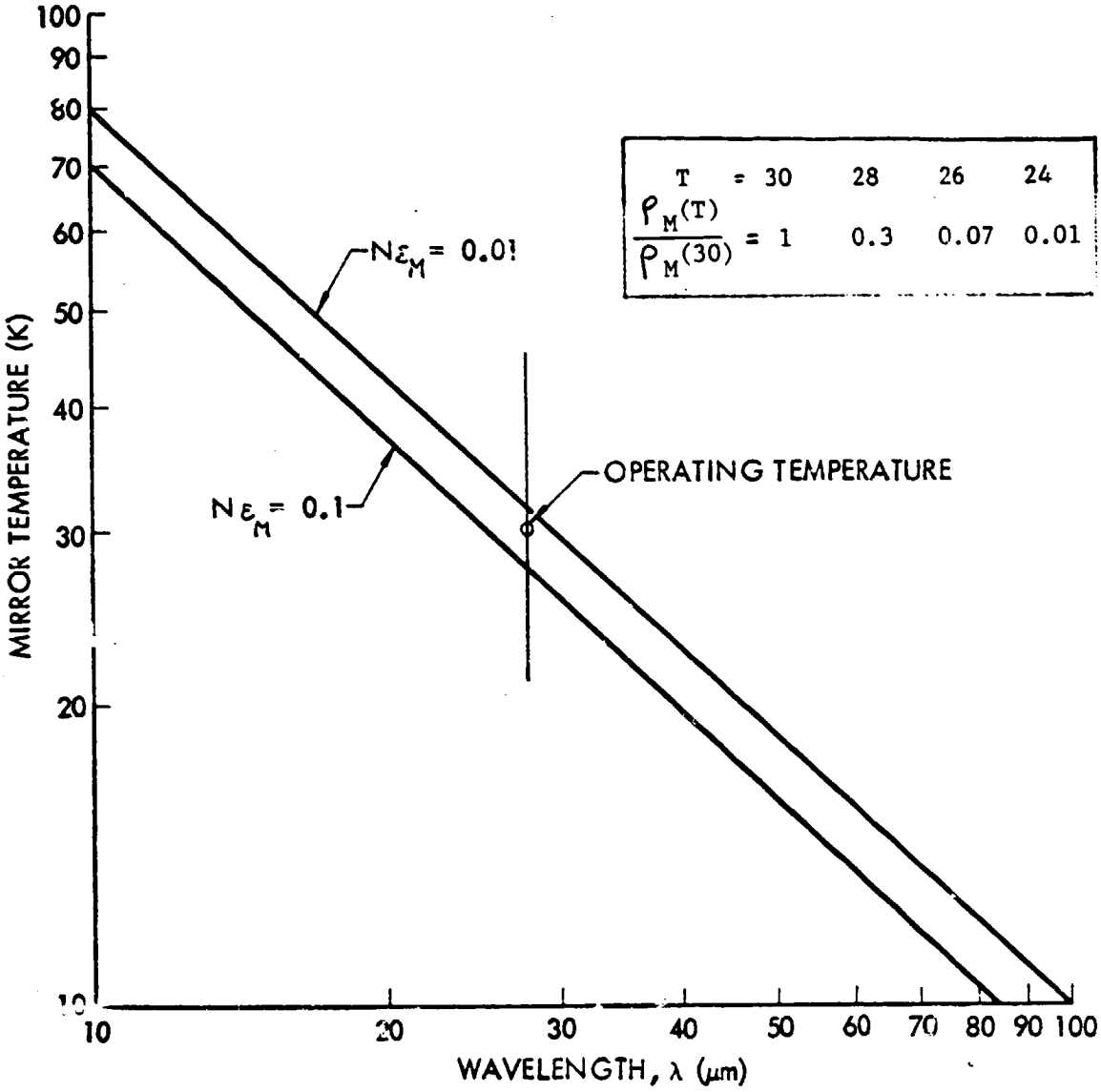

Fig. 4-1 Mirror Temperature

4.2.2 Scattered Light

Unwanted radiation falls onto the detectors by non-specular scattering from the optics. This problem will require particular attention and involve considerable study effort. One problem is the non-specular reflection from the secondary and relay mirrors of thermal radiation from the inside of the collimated beam tube which lead from the secondary mirrors to the focal plane dewar. The mirrors must be superpolished and kept clean to reduce scattering. The tube is assumed to be cooled passively since active cooling over the entire length (approximately 15 m each leg) is impractical and, at the very least, will have a substantial impact on the design of the IRIS cryogenic design. Radiation from the inner surface will be scattered by the mirrors onto the detectors and will be indistinguishable from background radiation entering the apertures. An ROM estimate of the irradiation of the detectors by this radiation is equal to

$$I_s \equiv N \frac{2c}{\lambda^4} \frac{1}{e^{hc/\lambda k T_t} - 1} \left[\frac{4\pi\sigma}{\lambda}\right]^2 \qquad (4\text{-}16)$$

where T_t the inner temperature of the tubes, σ the surface roughness of the mirrors, and N the number of contributing mirros in each interferometer leg (2 in a baseline design). The zodiacal irradiation is

$$I_z = \frac{1.2 \times 10^{-7}}{\lambda_{\mu m}} \frac{2c}{\lambda^4} \frac{1}{e^{hc/\lambda k T_z} - 1} \qquad (4\text{-}17)$$

For $T_t = 150^\circ$ K, $\sigma = 10$ Å we find

$$I_t / I_z \approx 5. \qquad (4\text{-}18)$$

Clearly, the area of the 'hot' (150° K) tube surface seen by the small mirrors must be reduced. This can be accomplished by actively cooling a portion of the tubes near the mirrors. (The mirrors are, incidentally, near the cryogen system for the primary and secondary mirrors; cf. Fig. 5-1) To reduce the unwanted radiation by a factor 1/10 (so that $I_s/I_z = 0.5$) the angle of acceptance

of radiation from 'hot' surfaces should be less than

$$\Phi = \sqrt{\frac{1}{10}\,\frac{4}{\pi}}\ \text{rad} \approx 20\ \text{deg} \qquad (4\text{-}19)$$

For a L=20 cm diameter of the collimated beam tubes, this implies that it would have to be cooled to within

$$L/\Phi \sim 60\ \text{cm} \qquad (4\text{-}20)$$

of the secondary and relay mirrors. This appears feasible.

A second problem is the scattering of sunlight and the thermal emission from the tower structure onto the primary mirrors. Proper design of the structure, detector optics and baffling of the primary mirror and relay optics is required. For our baseline design we have assumed that the detector optics in the dewar form aperture images suitable for elimination, using cold stops, of radiation entering the dewar directly from the surrounding structure. Even so, a detailed study of stray light using programs such as GUERAP and APART (used in stray light analyses of IRAS and ST) should be performed to arrive at a satisfactory optical design.

4.2.3 Detectors

Thermal noise in the detectors must be less than the zodiacal noise on the detectors, i.e.

$$\Omega_z T \varepsilon_z \varphi_z(\varphi_z+1) > 4\pi \varphi_D(\varphi_D+1) \qquad (4\text{-}21)$$

where Ω_z is the solid angle of view of a detector; T, the optics transmission and

$$\left.\begin{aligned} \varphi_z &= \left[e^{hc/\lambda kT_z}-1\right]^{-1} \\ \varphi_D &= \left[e^{hc/\lambda kT_D}-1\right]^{-1} \end{aligned}\right\} \qquad (4\text{-}22)$$

and

$$\varepsilon_2 = 1.2\times10^{-7}/\lambda_{\mu m} \qquad (4\text{-}23)$$

Thus we require

$$T_D < \frac{1.44\times10^4}{\lambda_{\mu m}} \Big/ \ln\left[\frac{4\pi}{T_2\xi_2\Omega_2\varphi_2(\varphi_2+1)}\right] \qquad (4\text{-}24)$$

Taking $\lambda_{\mu m}$ to be the cut-off wavelength, 28, we find $T_D \lesssim 11$ K. Candidate cryogen systems use solid hydrogen (temperatures down to $\simeq 8^\circ$K) or liquid helium (temperatures to $\simeq 4^\circ$ K). The latter is generally preferred because of a better developed technology and for safety reasons.

4.3 Radiation Hazard

High-energy radiation (charge particles - electrons and protons mostly - and Gamma rays) causes false events (photo-conductors respond like conventional counters), loss of observation time and detector deterioration. This hazard can be minimized by (a) proper choice of the orbit, e.g. by avoiding the South Atlantic Anomaly and regions of high particle flux; (b) not operating in the SAA; (c) shielding the focal plane assembly and electronics; (d) reducing the detector size to a minimum; (e) using electronic circuitry to discriminate against false (radiation-induced) signals - for example, pulse-height and rise-time analyzers; and (f) electronic hardening of the detectors.

High energy radiation also affects the mechanical properties of G/e structure, but the extent and long-term effects are not yet well known.

Acceptable rates for charge particle events depend on the processing electronics design. Estimates of the radiation hazard and of the necessary shielding have been made for other sensors, for example IRAS, and the experience gained there will be useful here. For an acceptable rate of 30 sec^{-1}, several cm of Al, Pb Be, or tungsten-nickel alloy suffice. Well outside the SAA, the rate of events due to cosmic background is much smaller.

Activation of certain materials near the detectors by charged particles can be troublesome if these are thorium or potassium or radium. Permanent detector damage occurs after a sufficiently long exposure, for silicon detectors after about 10^5 Rad. For mm size detectors, this dose is well above that expected for IRIS at the designed orbital altitude and during the five year life.

Solar flare events can overload a pulse rejection electronics for a substantial period of time (days). These events cannot be predicted for a given observation period, but the likelihood can be estimated from previous occurrences.

Electronic hardening techniques are well developed for protection against detector deterioration.

4.4 Contamination

As a high-sensitivity instrument, IRIS is susceptible to performance degradation caused by contaminants. The contaminants: dust particles and gas molecules scatter and radiatively emit IR photons into the field-of-view of the detectors and they also degrade the optical surfaces. They can originate in any phase of the construction, assembly, testing, storing, integrating, and loading of systems and subsystems, in the Shuttle bay environment, in rocket exhaust and in the orbital environment itself. Contamination by outgassing from the multi-insulation layers in particular cannot be avoided, and time must be allowed for sufficient outgassing after the final orbit is achieved, before observations can begin. The effect of dust particles in the spacecraft environment can be assessed by the fact that the IR radiation of a single, ≥100 μm diameter particle at the apertures can match the zodiacal background. A careful program of methods and procedures, involving controlled assembly environments is necessary to keep the total level of contamination to a minimum. This problem is clearly recognized in other high-sensitivity programs, e.g. IRAS, and the experience gained there will have a great impact on IRIS.

The scattering and emission of unwanted IR radiation by contaminants can occur anywhere in the optical path, from in front of the main apertures to the optical surfaces themselves. Degradation of the surfaces occurs by deposition of matter via impact, e.g. dust impacts and condensation of gases. Dust impacting at high velocity (e.g. zodiacal dust particles) will crater the surface and deposit fragmentary material (fron the dust and the mirror surface) on the mirror.

We now consider in detail the effect of infrared radiation from dust in front of the mirror, inside and outside the baffle tube.

Let a be a particle radius, T_d its temperature, and d the distance to the mirror. The flux of IR photons emitted by the particle is

$$F_d = \mathcal{I}_d \frac{\pi a^2}{d^2} \qquad \left(\text{photons/area.time.wavelength} \right) \quad (4\text{-}25)$$

where $\mathcal{I}_d$ is the radiance (photons/area.time.sterad.wavelength). The angular

diameter of the image of the particle on the focal plane is

$$\theta_d = D/d \tag{4-26}$$

where D=3m.

If θ_d is greater than the diameter of the FOV of the detector, θ_D, then the detector will be uniformly irradiated by the particle and receives photons at the rate

$$\varphi_d = \frac{F_d (\pi\theta_D^2/4)(\pi D^2/4)}{\frac{\pi}{4}(D/d)^2} \tag{4-27}$$

$$= I_d (\pi a^2)(\pi\theta_D^2/4)$$

If the converse is true, then the rate is

$$\varphi_d = F_d \pi D^2/4 = I_d \left(\frac{\pi a D}{2d}\right)^2 \tag{4-28}$$

The total rate on the detector is obtained from Eq. (4-26) or (4-27) by integrating over particle radii and the volume distribution of the dust. If n(a)da is the concentration of particles with radii between a and (a+da), dV a volume element, then the total rate is

$$\bar{\Phi}_d = \int_{(V)} \int_{(a)} \varphi_d \, n(a) \, da \, dV \tag{4-29}$$

For particle inside the baffle tube, the integration over V yields $L\pi D^2/4$ where L the length of the tube. We obtain from Eq. (4-29)

$$\bar{\Phi}_d^{(1)} = I_d \Omega_D \rho_i \overline{\pi a^2} \frac{\pi D^2}{4} L \tag{4-30}$$

where ρ_i is the total dust concentration inside the tube. For particles outside, we must consider those 'in focus' and out-of-focus' separately. For those which are a distance less than L_i from the mirror and are out-of-focus, Eq. (4-27) applies:

$$\underline{\Phi}_d^{(2)} = \frac{\pi\theta_2^2}{4} \int_{\Delta=L}^{\Delta=L,\ \infty} \int_{a=0} I_d\ \pi a^2 \Omega_D\, n(a)\, \Delta^2 d\Delta da \qquad (4\text{-}31)$$

$$= \Omega_D I_d \cdot \pi a^2 \rho_0 \cdot \frac{\Omega_D}{3} \cdot \left(\frac{D}{\theta_D}\right)^3$$

Finally, for the more distant particles, Eq.(4-28) applies. We shall not work out the corresponding rate and consider it to be included in the total zodiacal light brightness, discussed in Ch. 2.

We compare the rates $\underline{\Phi}^{(1)}$ and $\underline{\Phi}^{(2)}$ to that from the zodiacal light, which is

$$\underline{\Phi}_z = I_z\ \frac{\pi D^2}{4} \Omega_D \qquad (4\text{-}32)$$

We have

$$\underline{\Phi}_d^{(1)} / \underline{\Phi}_z = \frac{I_d \Omega_D \rho_i \overline{\pi a^2} \frac{\pi D^2}{4} L}{I_z \frac{\pi D^2}{4} \Omega_D} \qquad (4\text{-}33)$$

$$= (I_d / I_z)\ \overline{\pi a^2} \rho_i L$$

If the dust particles inside the baffle tube were at 300 °K, i.e. the same temperature as zodiacal dust, then $I_d/I_z = 26/1.2\times10^{-7}$ and we have

$$\underline{\Phi}_d^{(1)} / \underline{\Phi}_z = 6.9\times10^{-4} \alpha_i \overline{a^2} \qquad (4\text{-}34)$$

where $\alpha_i = L\rho_i$ is the areal density (particles/area) of dust in the tube, and a is in μm. From Eq.(4-34), setting $\alpha_i = 4/(\pi D^2)$, we find that one particle with radius $a = \sqrt{a^2} = 100\ \mu$m would flood the detector with photons at a rate equal to that by the zodiacal light.

We may however assume that the temperature of dust inside the baffle tube is close to that of the primary mirror, 30 °K since it must come in contact with it or the baffles. In that case we have $I_d/I_z = 12$. To keep dust emission below the zodiacal light, we need $\pi a^2 \rho_i < 0.1$. Suppose the tube can be kept at a cleanliness level corresponding to that of a Class 100,000 Clean Room. Then $\pi a^2 \rho_i \sim 10^{-3}$; therefore dust emission would be below zodiacal light levels.

For particles outside the tube but out of focus, we have

$$\Phi_d^{(2)}/\Phi_z = \frac{\pi \bar{a}^2 \rho_0}{3} \tag{4-35}$$

For this ratio to be less than one, we must have

$$\pi \bar{a}^2 \rho_0 < \frac{3\Theta_D}{D} \simeq 4 \times 10^{-5} \tag{4-36}$$

if we assume a typical FOV of 40 μrad. We take for $\pi a^2 \rho_c$ the value for zodiacal dust concentration near the earth increased by a factor 2 due to gravitational attraction. A high estimate is 4×10^{-16}/m (*) . Hence Eq.(4-36) is satisfied.

In conclusion, we find that IR radiation from dust inside and outside the baffle tube is small compared to the that of the zodiacal light.

The rate of condensation of atmospheric gas (mostly oxygen) can be high if the low temperature of the primary optics is low (sticking coefficient ≈ 1). It is approximately equal to $f \rho v$, where f is a geometric factor determined by the average angle between the apex of motion and the mirror normal, and the shielding geometry, ρ is the atmospheric density and v the speed of molecules relative to IRIS. For f=1 the build-up rate is 1 μm/200 hours. However, we must assume a random orientation of the mirror normal relative to the apex of motion, and that the mirrors will be carefully shielded and baffled. As a

---

* cf. Table 2-3 in "Properties and Dynamics of Interplanetary Dust," L. Bandermann, Ph.D. Thesis, U. of Maryland, 1968.

consequence we estimate f=0.04, which gives a condensation of only 1 μm/5 months. Such a condensation rate could be effectively counteracted by disconnecting the mirrors from the cryogenic support and letting the condensates evaporate. The disconnection would require a reliable (long-life) heat switch, e.g. a He gas-gap switch. It is expected that a contaminant deposition of about 1/4 μm (λ/100) will perceptibly degrade the optics.

Foreign matter on the mirrors which does not evaporate during the heating of the mirrors could possibly be removed by ion irradiation of the mirror surfaces. A drawback of this approach is that some of the coating material is also removed. Since the ion bombardment theoretically removes only one atom depth at a time, the surface could be cleaned by a short exposure to the ion beam without removing any significant depth of the 1/4 wave thick coating. One other problem might come from the entrapment of ions or some kind of property exchange due to the ion bombardment which could render the coating ineffective. However, this is not considered to be a likely happening.

The methods of contamination control will involve careful material selection, cleanable hardware, devising cleaning processes and careful monitoring of support and test equipment, working environment (clean rooms) and personnel. Purging of all surfaces prior to assembly may be desirable.

4.5 Interferometer Balance

The infrared interferometer uses destructive interference of the two input beams to eliminate the otherwise large number of stellar photons from one of the detectors. The efficiency of the technique depends on the degree to which the two pupil functions to be combined are matched. A mismatch in either the amplitudes or phases of the pupil functions degrades the interferometer null.

Two pupil functions combined by a beamsplitter with a 180° relative phase shift may be written as

$$\mathcal{F}(u,v) = A(u,v)e^{i\alpha(u,v)} - B(u,v)e^{i\beta(u,v)} \qquad (4\text{-}37)$$

where A, B represent the individual pupil amplitude functions of the aperture coordinates (u, v) and (α, β) are phase deviations from an ideal reference wavefront. With manipulation this becomes

$$\mathcal{F}(u,v) = \left\{(A-B)\cos\left(\frac{\alpha-\beta}{2}\right) + i(A+B)\sin\left(\frac{\alpha-\beta}{2}\right)\right\}e^{i\frac{\alpha+\beta}{2}} \qquad (4\text{-}38)$$

The first term in parentheses represents the effects of an amplitude mismatch between the two interferometer legs. Such mismatch could be produced by variations in mirror or beamsplitter reflectivity. The second term represents effects due to wavefront mismatch which might, for example, be caused by unmatched mirror figure error. The exponential term is the average wavefront error at each point in the aperture. The square of the Fourier transform of $\mathcal{F}$, when appropriately normalized, provides the photon distribution at the detector. In the interferometer, we are interested only in the energy in the central disk; therefore, a Strehl ratio calculation (i.e., the square of a normalized pupil function integral over the aperture) is appropriate.

The above procedure will be used to estimate the allowable phase and amplitude mismatch between the interferometer arms. Consider, for example, an interferometer imbalance due to a mismatch in beamsplitter transmission and reflection coefficients, called respectively T and R. Assume equal flux, C, input to both sides of the beamsplitter, and that $\alpha = \beta = 0$ (no wavefront error).

Then

$$\Phi = \sqrt{C}\left\{\sqrt{T} - \sqrt{R}\right\}. \tag{4-39}$$

For a mismatch of $T - R = \varepsilon$,

$$T = M + \varepsilon/2, \tag{4-40}$$

$$R = M - \varepsilon/2, \text{ and} \tag{4-41}$$

$$\Phi = \sqrt{CM}\left\{\frac{\varepsilon}{2M}\right\}. \tag{4-42}$$

Unnulled stellar flux in the aperture (which will fall on the "nulled" detector) is proportional to $\frac{C\varepsilon^2}{4M}$; i.e., the flux at one of the two input beamsplitter ports, C, has been reduced by a factor $\varepsilon^2/4M$ at the beamsplitter null output port due to a mismatch in beamsplitter reflectivity and transmissivity. For the example chosen, this leakage flux will be imaged on the detector as an Airy disk.

The same quadratic expression will occur if the fluxes incident on the beamsplitter differ due to differences in mirror reflectivity between the two interferometer legs. Over a small range, a beamsplitter mismatch may be used to compensate for differences in interferometer leg transmission.

If, in contrast to the above example, the flux across the pupil varies with pupil position, incomplete nulling would also occur. The amount of the unnulled flux to reach the detector will depend on the spatial distribution of the nonuniformity.

Let us now consider the effects of a phase mismatch between the two interferometer arms. We assume an intensity balanced interferometer, a 50% beamsplitter, and phase errors of α and β in the interferometer legs. The pupil function is

$$\Phi = i\,2\sqrt{C/2}\,\sin\left(\frac{\alpha-\beta}{2}\right) e^{i\left(\frac{\alpha+\beta}{2}\right)} \tag{4-43}$$

The flux passing through the null port is

$$\Phi\Phi^* = 2C\sin^2\left(\frac{\alpha-\beta}{2}\right) \tag{4-44}$$

If $(\alpha-\beta)$ differ by some mean phase, ϕ, due to a constant optical path

mismatch in the interferometer, the leakage flux will be imaged on the detector as an Airy disk of strength

$$2C\sin^2(\phi/2).$$

If the phase mismatch is such that its mean is zero across the aperture, the leakage flux will, for the most part, be scattered into the wings of the Airy pattern and, therefore, will not add to the flux on the detector. (The IRIS detector is slightly smaller than the Airy disk.)

These results will be used in the next section to establish component mismatch and pointing and alignment tolerances.

4.6 Pointing and Alignment

Achievement of zodiacal light background limited performance depends on accurately nulling the large numbers of in-band stellar photons. The IRIS interferometric alignment tolerances may be calculated from the criterion that the number of unnulled stellar photons present on the detector in the nulled beamsplitter output is equal to 50% of the zodiacal light background. Since the zodiacal light input is ≈2800 photons/sec/μm/aperture, and the input of stellar photons is $C = 1.2 \times 10^6$ per aperture per sec/μm, the stellar flux must therefore be reduced by a factor of 1.0×10^{-3}.

We define an interferometric null attenuation factor, G, to be the ratio of flux at the null output of the interferometer beam combining element to the flux from one interferometer leg into the beam combiner. As shown in section 4.5, G is a function of the accuracy of both amplitude and phase matching of the wavefronts from the two legs of IRIS. If we divide the allowable maximum null attenuation factor G_{total} into two equal components from phase and amplitude mismatch of $G_{phase} = G_{amplitude} = 5 \times 10^{-4}$ and a residual component, $G_{aberr.}$ for aberration mismatch, we can use the results of section 4.5 to calculate allowable interferometer errors.

For amplitude mismatch,

$$G_{amplitude} = \frac{\varepsilon^2}{4M} = 5 \times 10^{-4}. \qquad (4\text{-}45)$$

For $M = 0.5$, $\varepsilon = 3.2\%$.

Thus the transmission from each interferometer leg (primary, secondary, relay optics, and beamsplitter) may be mismatched by several percent and still reduce the unnulled stellar flux to below 20% of zodiacal light levels.

Likewise, for a constant phase mismatch of ϕ,

$$G_{phase} = 2 \sin^2 \phi/2 = 5 \times 10^{-4}, \qquad (4\text{-}46)$$

leads to a value of $\phi = 0.032$ rad. This implies that optical path differences in the interferometer arms must be matched to $\pm \lambda/200$ or $\pm$ 1300 Å.

Thus far, we have considered only DC terms from a static amplitude or phase mismatch such as would be produced by a static mismatch of beamsplitter transmissivity - reflectivity or of interferometer leg lengths. This type of mismatch

increases the sensor background level. A potentially more damaging error is produced if the interferometer mismatch is time varying at frequencies which fall at the planetary harmonics. Such errors would falsely indicate the presence of a planet through the production of a signal indistinguishable from that expected from the planet. To eliminate these A.C. effects, the interferometric null attenuation factor for A.C. variations at G_{AC} should be small enough so that the resultant A.C. signal is not detectable during the sensor observation time. The flux from a standard planet is 15 photons/sec/um/aperture. If we assume that an A.C. signal of 20% of this will not constitute a detection,

$$G_{AC} \leq \frac{3}{1.2\text{x}10^{6}} = 2.5\text{x}10^{-6} \qquad (4\text{-}47)$$

Therefore, the maximum allowable time varying optical path difference (at frequencies which are even multiples of the IRIS rotation) is ~92 Å.

Phase mismatch due to optical path differences (OPD) may occur anywhere in the path from the emitter in the star through the telescope and relay optics forming each interferometer leg to the beam combiner. Hence equivalent OPD changes may be produced by several mechanisms such as interferometer baseline tilt (i.e., interferometer pointing error), unequal interferometer leg lengths, or slight errors in primary-secondary mirror separation. However, only the total relative OPD matters. Therefore, as long as wavefront tilts and aberrations are sufficiently small so that efficient wavefront cancellation will occur (this will be discussed later), an OPD induced by an interferometer pointing error may be compensated for; for example, by an appropriate time-varying adjustment of the interferometer leg length or by an adjustment of the primary-secondary mirror separation.

The above phase matching considerations and the fact that periodic structural distortions (for example, from gravity gradient stresses) could produce a signal which is indistinguishable from the period signal from a planet. Sensing such errors requires an OPD measurement technique which is independent of any planetary signal. The use of IRIS as an interferometer in the visible ideally fulfills this requirement.

The visible IRIS interferometer sensor uses the visible light from the parent star to provide a strong reference wavefront for measuring OPD and tilts. The visible interferometer also operates in a null-antinull configuration; a small amount of OPD dither is introduced to produce a narrowband A.C. signal.

The most stringent requirement on the visible interferometer is to detect the A.C. OPD variations. Assuming a visible wavelength centroid of 0.55 μm, the ~90 Å allowable OPD mismatch will result in an interferometric null factor in the visible of

$$G_{vis} = 5.28 \times 10^{-3} \qquad (4\text{-}48)$$

From a stellar visible flux of 1.2×10^{6} photons/sec/μm into each interferometer leg, a flux of 2500 photons/sec (in a 0.4 μm band) would be incident upon the detector at maximum allowable OPD mismatch of 90 Å. Such a signal should be detectable in a nulled situation, especially if the signal is made to be time varying by dithering of optical train mirrors. If a smaller central portion of the mirror were to be used for the visible interferometer, the signal would be correspondingly reduced, but the mirror figure requirements could be relaxed over that portion not used for the visible phase measurements. The signal from the visible interferometer would be used to adjust the bias of the dither mirror to preserve equal excursions about the interferometer null.

Wavefront tilts could be detected by stellar image centroiding prior to wavefront combination or, more elegantly, by comparing the efficiency of the interferometer null at the edge of the beamsplitter to that at the center. Accurate centroid measurement of the steller image to 1/200th of a spot diameter (λ/160 rms) is easily possible. Tilt correction is effected by any of the relay mirrors.

We now discuss wavefront errors allowable in the IRIS optics exclusive of phase and tilts which have already been considered. Wavefront errors (from misalignment of optical figure aberrations degrade the interferometer null.

two conditions must be met: 1) at λ=26μm

$$G_{aberr} < 2.5 \times 10^{-4} \qquad (4\text{-}49)$$

and 2)

the dither signal from the visible interferometer should not be masked by excessive DC background. Since the average phase mismatch of the two wavefronts across the aperture is zero little energy passing through the null port will fall on the detector (which subtends the central part of the Airy disk); much of the energy will be scattered into the wings. In the infrared tolerance calculation we assume conservatively that all of the energy through the null port is detected (this guards against the effect of time varying figure errors. Condition 1) results in a mirror figure specification of $\sim \lambda/50$ rms at λ=26 μm. For condition 2), we assume 25% of the energy passed will fall on the detector and that detection of the visible interferometer dither signal can occur in a DC signal ten times its magnitude. These assumptions lead to a mirror figure specification of $\lambda/20$ rms at λ=0.55 μm. over that portion of the mirror to be used for the visible interferometer.

Most of this figure error should occur at the 3 meter primaries because of their size and exposure to the space environment. The other mirrors are small and enclosed.

During the design study of the 3 meter telescope optics, trades should be made as to the difficulty of figuring and maintaining accurate optics in a space environment. Active correction of the optics could be implemented, if required, using the parent star wavefront as a reference. A trade should also be made to determine the primary mirror area monitored by the visible interferometer. The assumption is made that the central 25% of the primary area is used in the visible interferometer.

Alignment criteria may now be calculated. An error budget of $\lambda/40$ rms in the visible for both focus and lateral secondary misalignment results in alignment criteria of ~15 μm focus and 800 μm lateral. (The visible interferometer telescope focal ratio of 6 rather than the IRIS optics focal ratio of 3 was used in this calculation.) These tolerances do not stress state-of-the art technology.

In summary, interferometer amplitude matching and telescope misalignment aberrations, and telescope pointing do not provide any requirement which is beyond state-of-the-art. Interferometer phase matching, however, will require OPD sensing and corrections on the order of 90 Å, at low bandwidths, to compensate for IRIS pointing errors and for periodic stresses which may if not

sensed produce a signal similar to that expected from the planet. The sensor concept and sensor implementation to provide such a measurement of OPD variations seem achievable and should be discussed in detail in the IRIS design study.

Figure requirements on the primary mirror are difficult but achievable. The problem is that the beryllium mirrors must be held to a nearly constant temperature while in orbit to prevent figure changes. Temperature tolerancing and the art of cryofiguring should also be extensively studied in the design phases of mirror construction.

Table 4.1 provides a numerical summary of the above results.

Table 4.1
IRIS OPTICAL SYSTEM REQUIREMENTS

Parameter	Value	Comment
Primary Diameter	3 m	Fits in spacecraft
Primary Focal Ratio	3	Deployable Secondary Struts
Telescope Magnification	30	Small Optical Train
Body Pointing Accuracy	50 μrad	Prevent Beam Walk
Phase Matching Accuracy DC	0.13 μm	20% zodiacal light
AC	0.009 μm	20% standard signal
Optics Figure (visible interferometer constraint)	$\lambda/20$ rms at λ=0.55 μm	Reduce DC signal in visible interferometer null signal. (High spatial WFE frequencies not included)
Optics Figure (26 μm constraint)	$\lambda/50$ rms at λ=26 μm	10% zodiacal light signal
Flux matching; 50% beamsplitter	3%	20% zodiacal light
Primary-Secondary Separation	15 μm	Focus
Primary-Secondary Lateral Misalignment	800 μm	Coma

4.7 On-Orbit Calibration

After deployment, the spinning IRIS is pointed at a bright IR/visible star for alignment and calibration. The pointing and alignment of each telescope are corrected individually by observing the stellar image and by actuation to correct any image defects. Each telescope is body pointed at the star using the criterion of elimination of image motion of the star under IRIS rotation. The IRIS baseline should now be located perpendicular to the line of sight (LOS) to the star. A Strehl ratio or image sharpness measurement is now used to obtain a secondary mirror misalignment signal to drive appropriate secondary mirror actuation. The above two steps are iterated (since secondary motion affects both telescope LOS and misalignment aberrations).

The relay optics are now actuated to align the two stellar images on a centroid detector viewing the null port output (i.e., match the wavefront tilts). Alignment is established when alternate shuttering of the interferometer legs do not produce any jump in the stellar image position. After the shuttering calibration is complete, tilt sensing (and wavefront error sensing for that matter) could be continued if a small portion of the wavefront from each leg were sampled and stabilized independently.

After tilt matching, both legs of the interferometers are unshuttered; coherent interference effects should be apparent. The interferometer path length is varied to produce white light interference fluctuations. Fluctuation contrast is maximized. This procedure establishes equal optical paths in each interferometer leg. The visible interferometer is dithered about a fringe null by actuation of an optical train mirror back and forth along its surface normal by 0.01 μm.

The above procedure results in the correct pointing and aligrment of the visible interferometer. The IR detector viewing the null port is calibrated using alternate shuttering of the interferometer legs. Telescope transmission and detector drift are measured. It is expected that telescope transmission of each interferometer leg has been matched during ground testing; no adjustment should be required. An IR blackbody source illumination of the primary mirror provides radiometric calibration of the two color detectors used for IRIS temperature. With both interferometer legs unshuttered, the IRIS IR interferometer

null output flux is reduced to a minimum (phase matched) allowing if required a small amount of fringe jumping of the visible interferometer.

A small pointing error is introduced; the resultant signal is monitored to establish agreement with that predicted using the known pointing error and the measured total stellar flux through the antinull output port as input parameters. These procedures are repeated periodically for calibration check.

In summary, the IRIS is extremely sensitive to interferometric misalignments so that the majority of the calibration procedure is used to establish and preserve the alignment. The other key area, the periodic drift of detector output at frequencies of the expected planet signal, is addressed in the IR sensor response to constant illumination. Detailed radiometric calibrations are required if it is desired to use the IRIS for quantitative characterization of stellar and planet brightness at the working wavelengths.

5. Baseline Design

5.1 Structure

A conceptual systems design of IRIS is shown in the engineering drawing (fold-out) and in Fig. 5-1. Overall dimensions of the satellite are near Shuttle payload bay dimensions: 17 m x 4 m. The (tubular) truss structure if made of graphite-epoxy, for maximum stiffness-to-weight ratio. The two towers holding the secondary mirrors are each 8.4 m high and are folded onto the main structure while IRIS is inside the Shuttle bay; they are deployed after final orbit is achieved. The primary mirrors (3 m diameter, off-axis, parabolic, f/3), made of beryllium, are inside baffle tubes whose design is yet to be determined. The aperture doors are vacuum tight and remain closed until final orbit. The secondary mirrors at the top of their respective towers are contained within light tight tubes (the collimated beam tubes) which lead to the focal plane dewar. The tube is pierced at the top by a shaded pinhole which admits the radiation reflected from the primary mirror. The diameter of the secondaries will be determined with considerations for minimizing stray-light and is expected to be 10-30 cm. The cryogen tanks (sNe) for the secondary mirrors are at the tops of the towers, and those for the primary mirrors are located inside the main structure, adjacent to the mirrors.

The focal plane instrumentation including folding mirrors and beamsplitters is located in a liquid-helium dewar. Located on the spin of IRIS axis are the spin table and the star trackers. The central structure accommodates a propulsion engine designed to deliver IRIS from Shuttle handoff to baseline orbit, as well as the necessary tanks and fuel.

ACS tanks and batteries can be swung outward from the main structure. By such mass displacements one assures that the spin axis points along the axis of the largest moment of inertia and the satellite can rotate stably about the axis.

Two omni-and high-gain antennas are shown. The solar panels affixed to the bottom of the main structure are shown undeployed. The entire main structures will be covered with multi-layer insulation (MLI). One goal will be to achieve 150° K temperatures inside the collimated beam tube passively, except

C-2

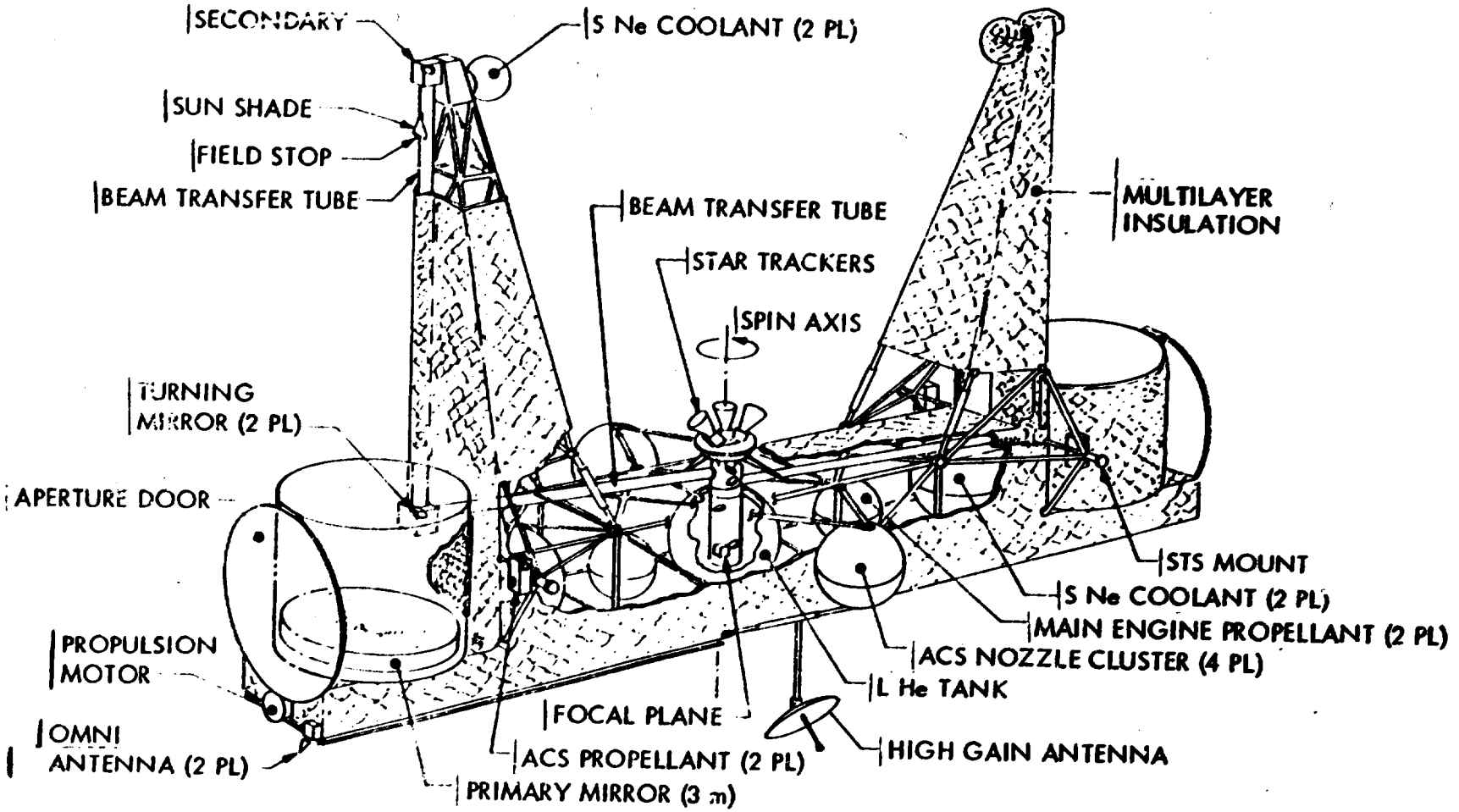

SPINNING INFRARED INTERFEROMETER (IRIS)

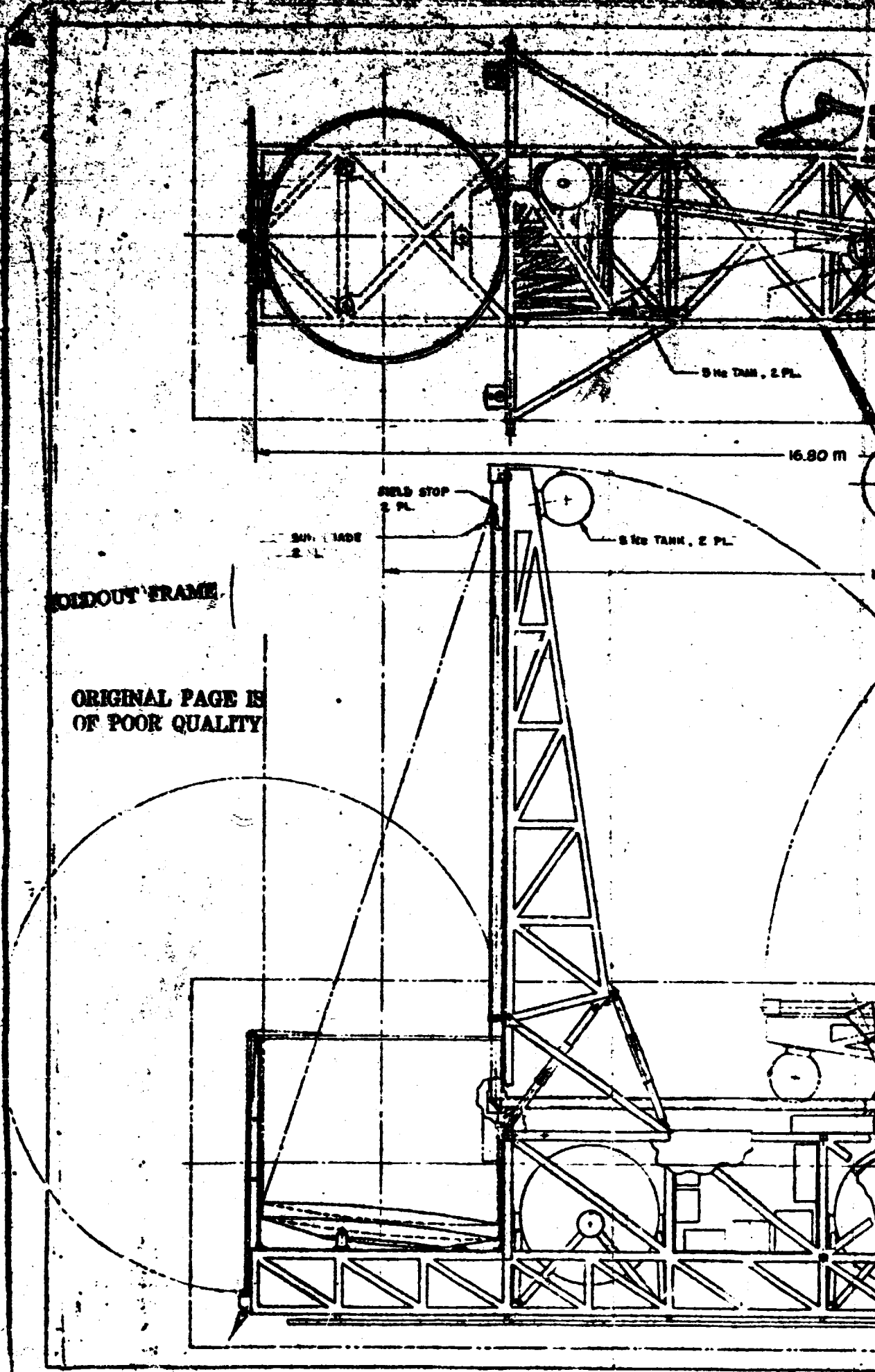

OLDOUT FRAME

ORIGINAL PAGE IS
OF POOR QUALITY

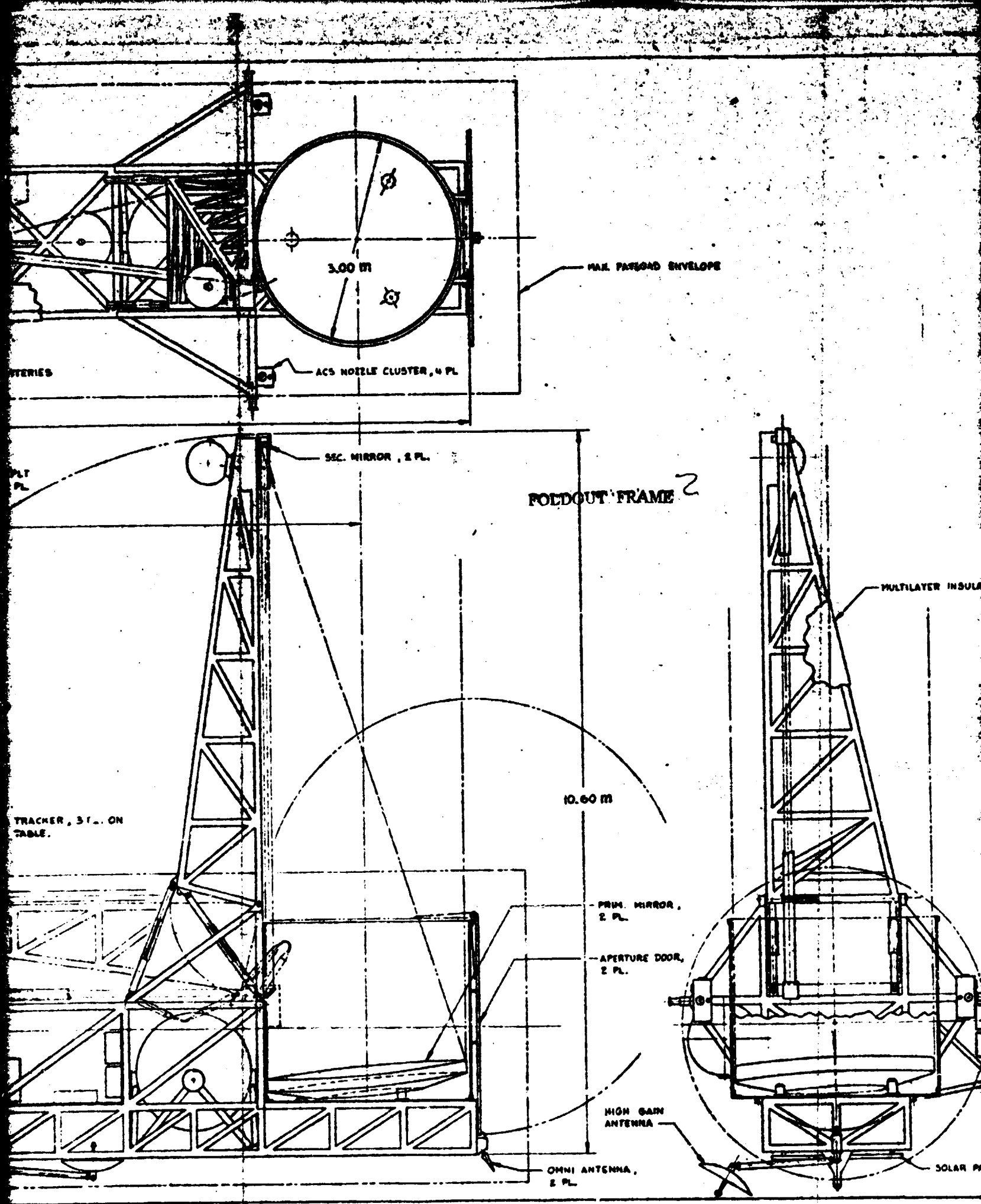
3.00 m
MAX. PAYLOAD ENVELOPE
ACS NOZZLE CLUSTER, 4 PL
SEC. MIRROR, 2 PL.
FOLDOUT FRAME 2
MULTILAYER INSULA
10.60 m
PRIM. MIRROR, 2 PL.
APERTURE DOOR, 2 PL.
HIGH GAIN ANTENNA
OMNI ANTENNA, 2 PL.

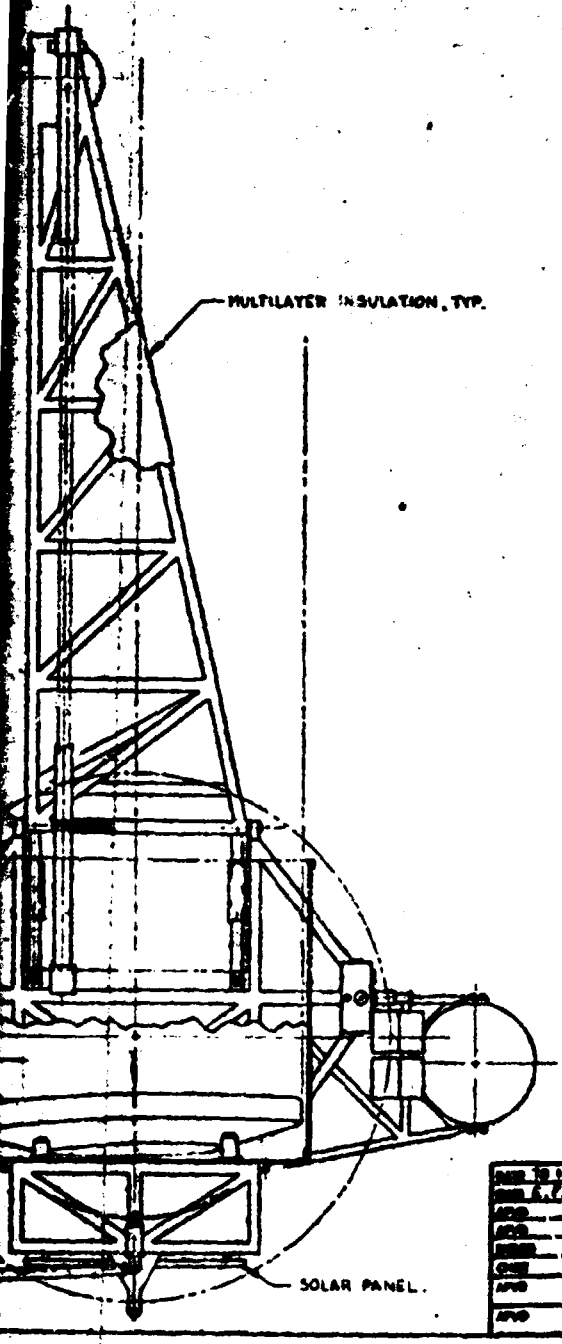

FOLDOUT FRAME 3

DATE 30 NOV 80	LOCKHEED MISSILES & SPACE COMPANY, INC.	
DRAWN A.C. GARY		
APVD	IRIS	
APVD	INFRARED INTERFEROMETER SYSTEM	
APVD	SIZE J	SKC-781120 REV A
APVD		

IRIS
SKC-781120

6-2a

for portions near the secondary and turning mirrors (about 60 cm in each direction) which will be actively cooled to ~30° K.

5.2 Optics

5.2.1 General Layout

A conceptual optical layout is shown in Fig. 5-2. Radiation from the target is reflected by the primary mirror through the pinhole (field stop) onto the secondary mirror inside the collimated beam tube. The optical configuration is afocal Gregorian. The collimated radiation travels down the beam tube, through a pupil stop to a turning mirror and to the FP dewar.

Radiation from the left interferometer leg passes (inside the dewar) through the dichroic 50% beamsplitter, with half the radiation from that leg going to the null port (down in this drawing) and half to the antinull port (to the right). Radiation from the other leg is first reflected by a turning mirror (inside the dewar also) before passing through the beamsplitter. This has the effect of superimposing corresponding parts of the images from the two legs thereby assuring a constant baseline (see Sec. 5.2.2).

Radiation in the antinull port contains the stellar photons from both apertures and half of all background photons. Since the stellar radiation is overwhelming, this port can be used for tracking on and analysis of the star. Radiation in the null port is used for planet detection, temperature measurement and other observations of the planet. Three output legs are shown since at least two different IR wavelength regions will be used, as discussed in Sec. 3, and the third is used for visible interferometry of the star (see Sec. 4-6).

5.2.2 Shearing vs. Folding Interferometer

There is a choice of wavefront-folding or wavefront-shearing geometries for the interferometer. Versions of the two are shown in Fig. 5-3. Basically, with a folding interferometer both beams suffer the same number of reflections when they impinge on the detector. For the shearing interferometer one of the beams has an extra reflection. The result is that the shearing interferometer has a constant baseline, b, across the whole aperture. By contrast, the folding

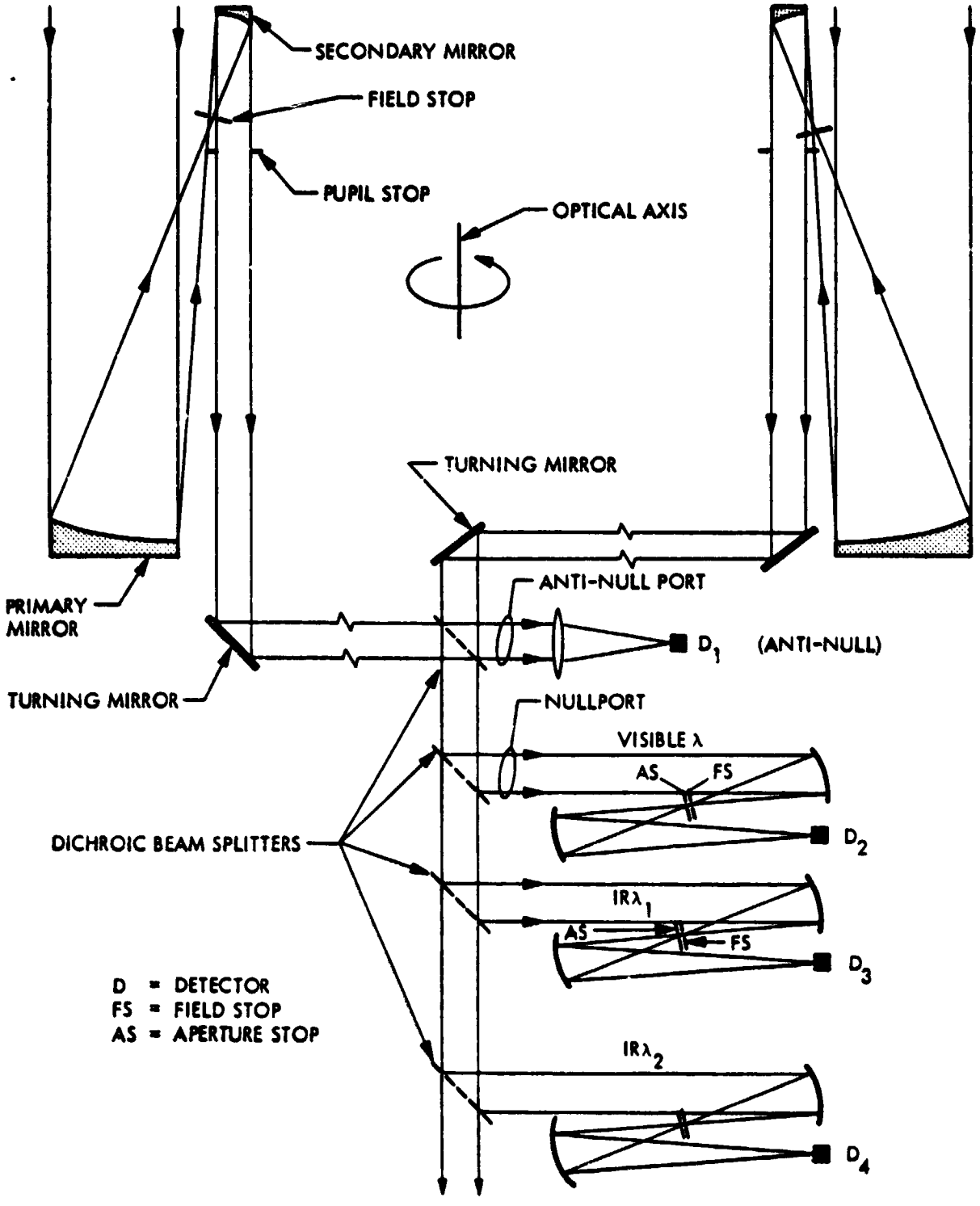

Fig. 5-2 Schematic Optics Layout

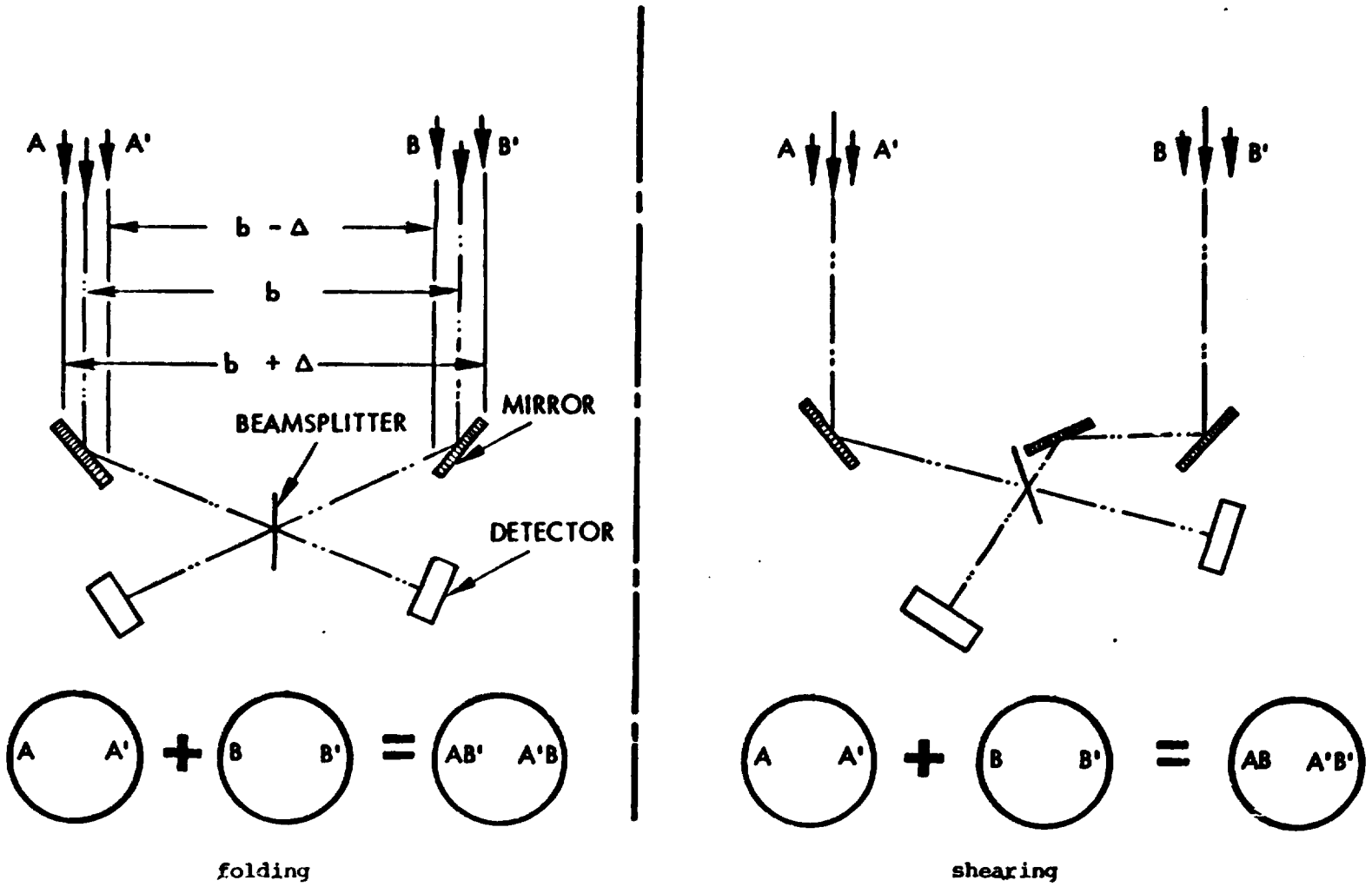

Fig. 5-3 Folding Versus Shearing Interferometer

interferometer has a range of baselines extending from the separation of the innermost parts of the apertures to the separation of the outermost parts. This range of values of b would lead to another envelope similar to that for spectral bandwidth, and only a few fringes near zero path difference would have high contrast.

Since the folding interferometer has no special virtue for the intended application, the shearing interferometer is preferred, especially since the planet may be several fringes from the star.

5.2.3 Beamsplitter

The interferometer fringes are shown schematically in Fig. 5-4. Whatever absorption there is in the beamsplitter is "off the top" and the photons are wasted. Level M is nominally (1/2) (1-A). The envelope of the fringes is the result of finite spectral bandwidth. The fringes within the envelope are well known as the interferogram of Fourier transform spectrometry.

The simplest beamsplitter is a thin metallic film. Unfortunately, for a metallic film of thickness such that transmission equals reflection the absorption is 50%. The fringes have the symmetric form

$$(1/4)-(1/4)\left[\exp-(ax)\right]\cos x \qquad (5\text{-}1)$$

where x is the path difference. The central fringe is black rather than white because of the 180° phase change at reflection. The two outputs of the interferometer are <u>not</u> complementary; both are black at zero path difference.

The simplest <u>dielectric</u> beamsplitter is a pellicle, often used for far infrared Fourier transform spectrometry. Absorption is negligible; therefore, the sum of the output intensities equals the sum of the input intensities. Because of symmetry the outputs must be equal to each other, each being half of the total input intensity, and certainly not null. As the relative path difference of the arms change, one output goes to a dark fringe (null) while the other goes to a bright fringe. The fringes have the antisymmetric form

$$(1/2)+(1/2)\left[\exp-(ax^2)\right]\sin x \qquad (5\text{-}2)$$

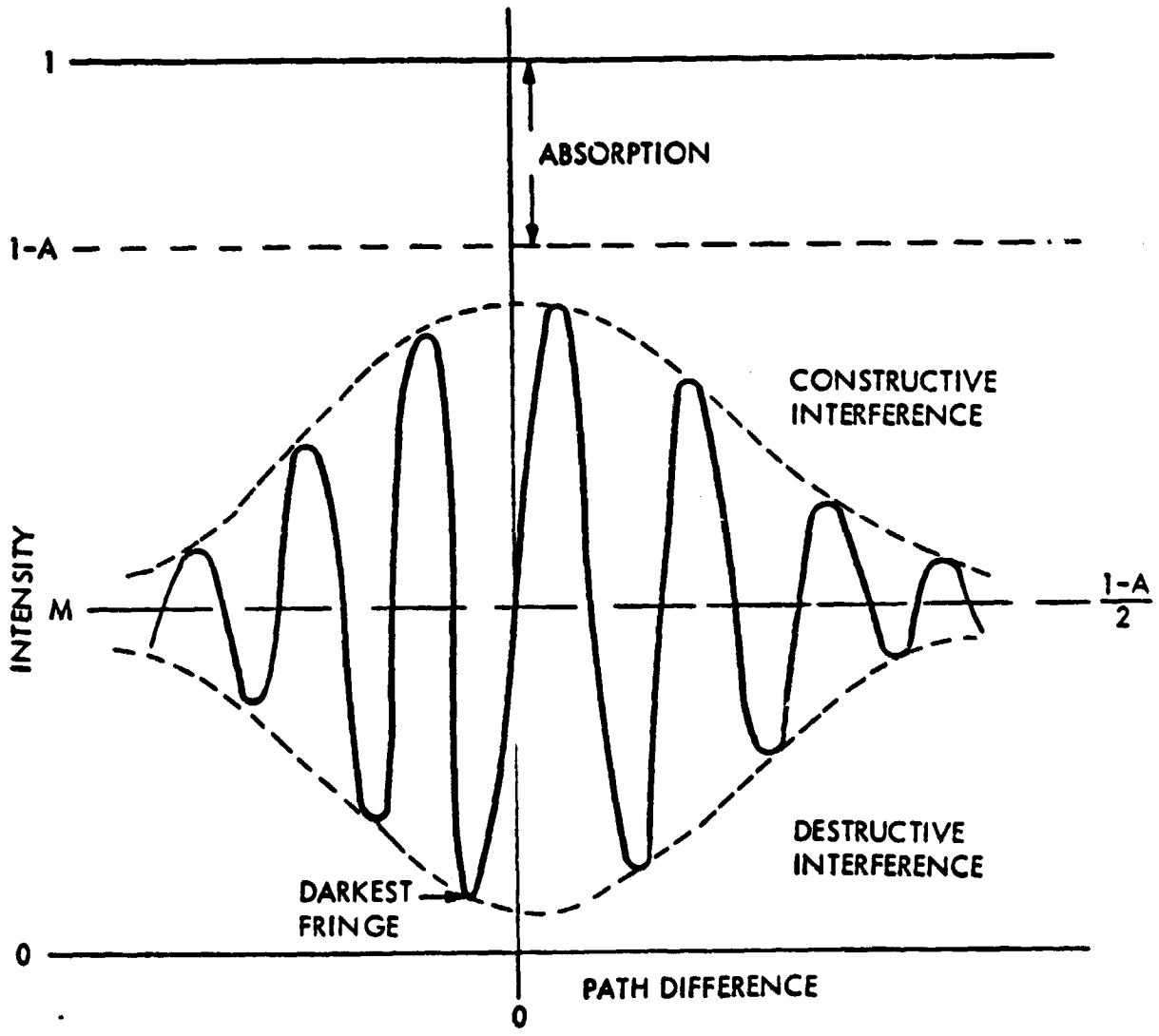

Fig. 5-4 On Beamsplitter Considerations

A non-symmetric beamsplitter may be just the dielectric reflection off a substrate with the rear surface anti-reflection (AR) coated. A compensating plate having both surfaces coated is inserted in the opposite beam. Another version is a quarter wave thickness of low index material next to a quarter wave thickness of a high index material sandwiched between two medium index substrates, which are AR coated on their exterior surfaces. The fringes for this beamsplitter are the same as that for the pellicle.

Because of the antisymmetric form of the fringes for dielectric beamsplitters, the dark fringe is offset from the center of symmetry of the envelope. For wideband systems the envelope is narrow and an offset means that full black is not attained by an adjustment of path difference. However, we may note that the fringes not only look like a wave packet, they also behave like one. Placing a dispersive dielectric in one arm of the interferometer shifts the underlying fringes according to the customary phase velocity index of refraction. The envelope shifts according to the group velocity index of refraction. The underlying fringes therefore shift with respect to the envelope according to the difference of those indices. It is desirable to insert a different dielectric material into the other arm to return the fringes to being on-axis.

5.2.4 Phase Information Retrieval

By inserting a relative phase shift, δ, into the sky projected interferometer response, fringe pattern of the interferometer may be shifted. For example, a net $\delta = 180^\circ$ relative phase shift in the pupils results in a star centered ($\theta = 0$) interferometer response to the star of

$$V_1 = \sin^2\left[\frac{\pi b \theta}{\lambda}\right] = \frac{1}{2}\left[1 - \cos\frac{2\pi b \theta}{\lambda}\right] \qquad (5\text{-}3)$$

on one detector (star nulled), and

$$V_2 = \cos^2\left[\frac{\pi b \theta}{\lambda}\right] = \frac{1}{2}\left[1 + \cos\frac{2\pi b \theta}{\lambda}\right] \qquad (5\text{-}4)$$

on the other (star antinulled). The signal in both detectors contains only cosine functions of θ. It is therefore impossible to remove an ambiguity of $\pm\pi$ in the planet position angle around the star.

A suggestion has been made for a polarization separation interferometer in which one polarization is used in a stellar null-antinull configuration described above while the other polarization component is given a relative phase shift to provide an interferometer response of

$$V_3 = \frac{1}{2}\left[1 - \sin\left(\frac{2\pi b\theta}{\lambda}\right)\right] \qquad (5\text{-}5)$$

one one detector and

$$V_4 = \frac{1}{2}\left[1 + \sin\left(\frac{2\pi b\theta}{\lambda}\right)\right] \qquad (5\text{-}6)$$

on the other detector. (A star at $\theta = 0$ is equally distributed on either detector.) The extra information provided by the sine term allows for the elimination of the Π ambiguity in planet position angle.

The disadvantage of this approach is that signal to noise of the detection system against the baseline star-planet system is reduced up to 24% (depending on the ratio of parent star photons to Zodiacal light photons on the central Airy disk). This loss in signal to noise is to be expected since in this mode of operation more of the signal photons from the planet are competing against unnulled stellar photons.

5.3 Orbit

The selection of suitable baseline orbit is influenced by the simultaneous considerations for

1. the required minimum 5 year orbital life;
2. target viewing time (per orbit and percent of orbit);
3. shadow time (per orbit and percent of orbit);
4. the radiation environment including the South Atlantic Anomaly;
5. opportunities for spacecraft communications: householding and data dump.

1. The orbit lifetime depends on the spacecraft drag coefficient, the orbital parameters (apogee, perigee, inclunation, node, etc.) and the launch date. The date enters because upper atmospheric conditions are influenced by the solar activity which has an 11-year cycle. Fig. 5-5 illustrates the effect for circular orbits of various radii and with an inclination $i=28.5^{\circ}$, and a drag coefficient of 0.01 m^2/kg. For an 11-year cycle, a launch date of 1/89 would require a minimum altitude of about 300 n.m. for a 5-year lifetime. However, conditions improve for some time after that date. Thus a 550 km altitude seems adequate for a 5-year orbit life.

2. The target viewing time is influenced by (a) its visibility and (b) background and stray light requirements. The simultaneous requirements for shadow viewing, lunar and solar avoidance and background requirements substantially reduce the availability of targets for observation. The scheduling of various targets (candidate stars) will therefore not be trivial even though sufficient total experiment time may be available.

3. Total shadow time per orbit depends on the orbit parameters. For circular orbits the time is greater for low inclinations than for high inclinations. For equatorial orbits it is ~35 min. The continuous shadow viewing time can be greater for elliptical orbits (apogee at anti-solar point). This requires the line of apsides to rotate such as to follow the sun. Such orbits have the advantage of requiring fewer target re-acquisitions than for circular orbits. However, the percentage of shadow time <u>per total time</u> is smaller than for circular orbits.

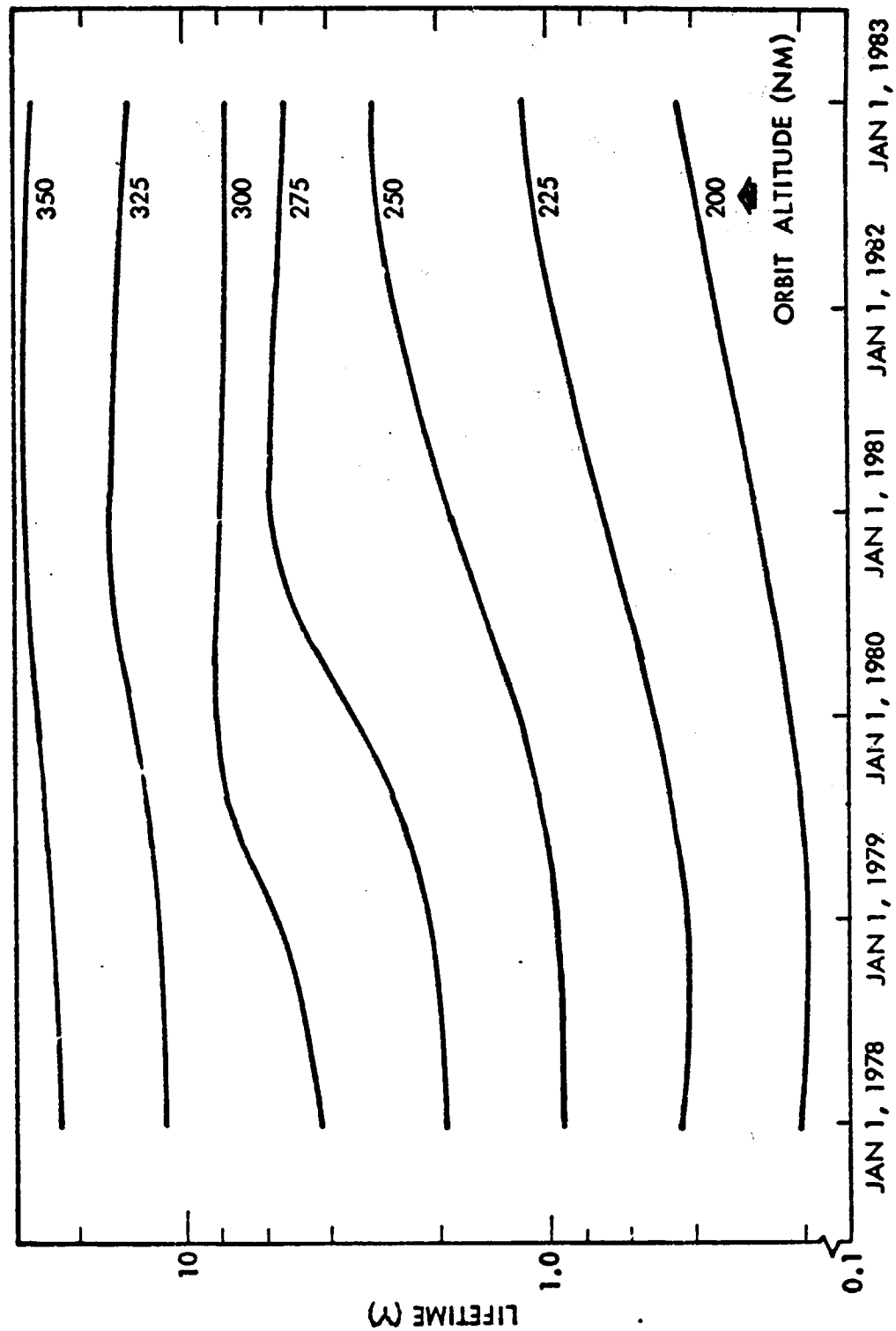

Fig. 5-5 Orbit Life Time

4. Higher altitude orbits entail a greater radiation exposure than lower orbit, and higher inclination orbits involve greater exposure to the SSA than low-inclination orbits, and a corresponding greater loss of observation time. Very low inclinations ($i < 28.5^{\circ}$) cannot be attained except using a space tug, at the expense of reduced payload and increased cost.
5. Spacecraft communication is not a driving factor for this experiment because the data dump rate is expected to be low (long integration time!).

Above considerations led us to choosing a circular, 550 km altitude, minimum inclination orbit ($i=28.5^{\circ}$, ELS launch) which has the necessary lifetime and satisfies all other experiment requirements with a minimum of expense.

IR in-band radiation from above the atmosphere is small compared with minimum zodiacal light (Fig. 5-6).

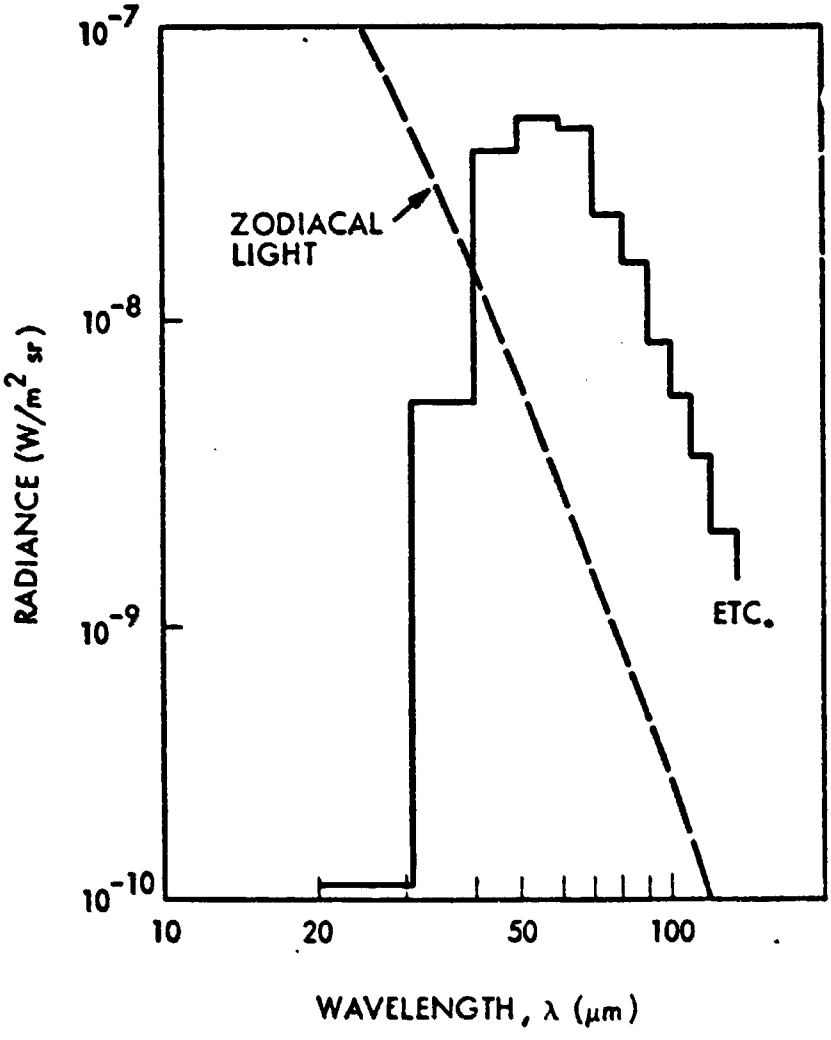

Fig. 5-6 Infrared Radiation From Atmosphere Above 350 Km

Ref.: Simpson, J. P, and Wittenborn, F. C., Appl. Opt. 16, 2051, 1977

5.4 Propulsion

The mass of the IRIS sensor system without propulsion is 12,500 kg (Table 5-2). To achieve the baseline orbit (550 km circular, 28.5° inclination) a separate propulsion system is required to add to the boost capability of the Shuttle itself (cf. Fig. 5-7). These choices exist: (i) IUS, (ii) OMS kit, (iii) tailored solid propellant rockets, (iv) liquid propellant rockets.

(i) The IUS is too large for this application: The smallest design has two stages, weighs 32,500 lb and is 16 ft long. It would therefore require a separate launch and subsequent rendezvous and docking.

(ii) An OMS kit provides approximately 500 ft/sec to the Shuttle performance, but this translates into a trade of a decreased cargo-carrying capacity of 5,500 kg, for an increase in altitude of 200 km. An advantage of using an OMS kit is that OMS is already part of the planned STS development program, although an OMS does not exist yet. Disadvantages are: (a) the available cargo space is reduced; (b) the entire Shuttle is boosted, which appears unnecessary and wasteful.

(iii) Some flexibility exists with solids. Fig. 5-8 shows that the required propellant load is about 2200 kg.

(iv) The choices for liquid propellant rockets are given in Table 5-1. We exclude electric propulsion as a choice because of the large inherent cost of such a system, the fact that it would be used only once, and because a satisfactory engine has not been developed. Nitrogen is also excluded because it lacks a developed engine and has a high fuel weight requirement. Of the remaining choices, only hydrazine has a developed technology (engine) and has an acceptable thrust value. The fuel requirements are moderate. This is our first choice for a sensor system to be designed now. Our second choice is nitrogen for less spacecraft contamination; but it requires a development program for a suitable engine.

NASA-S-77-3157

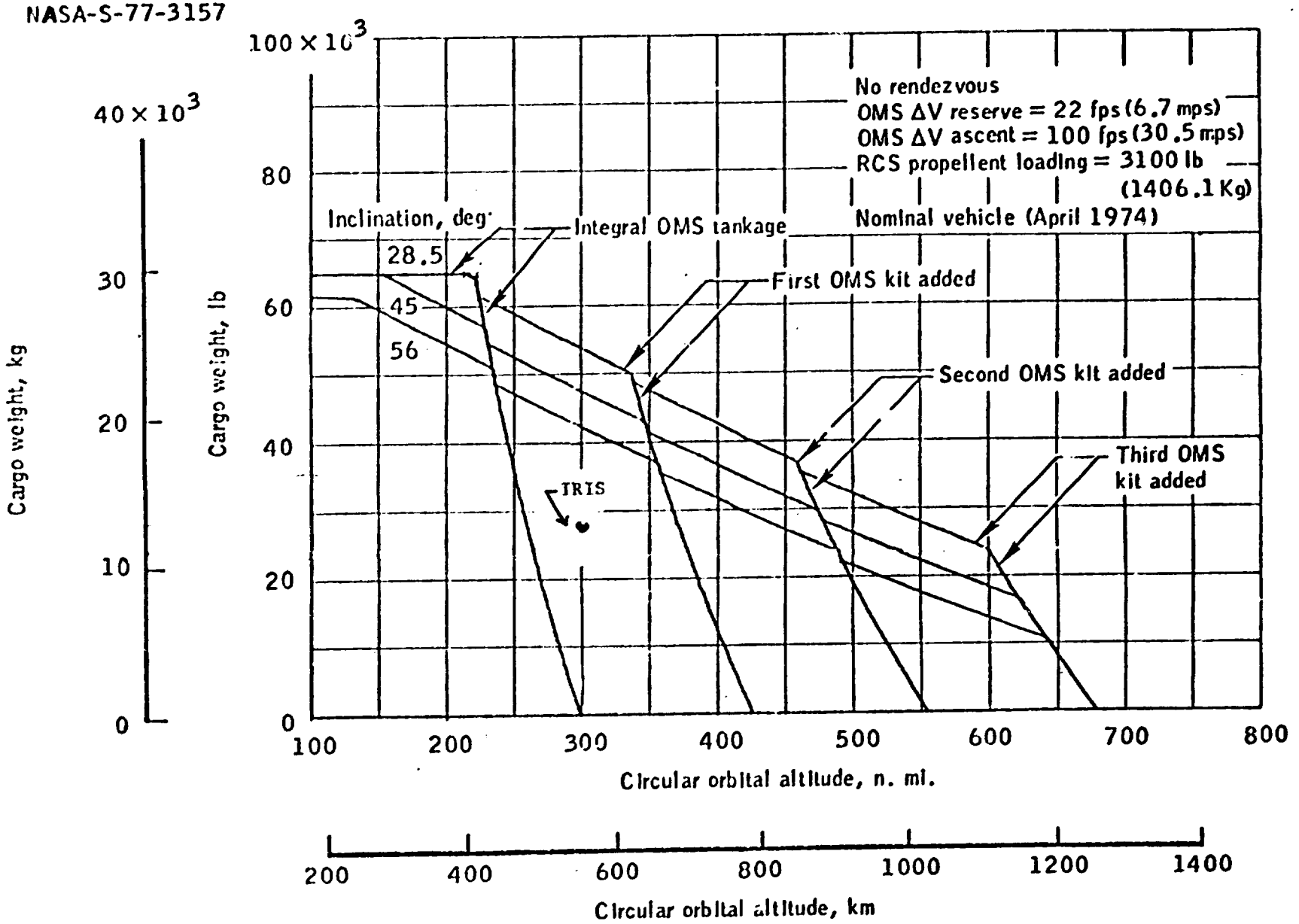

Fig. 5-7 Shuttle Orbit Capabilities

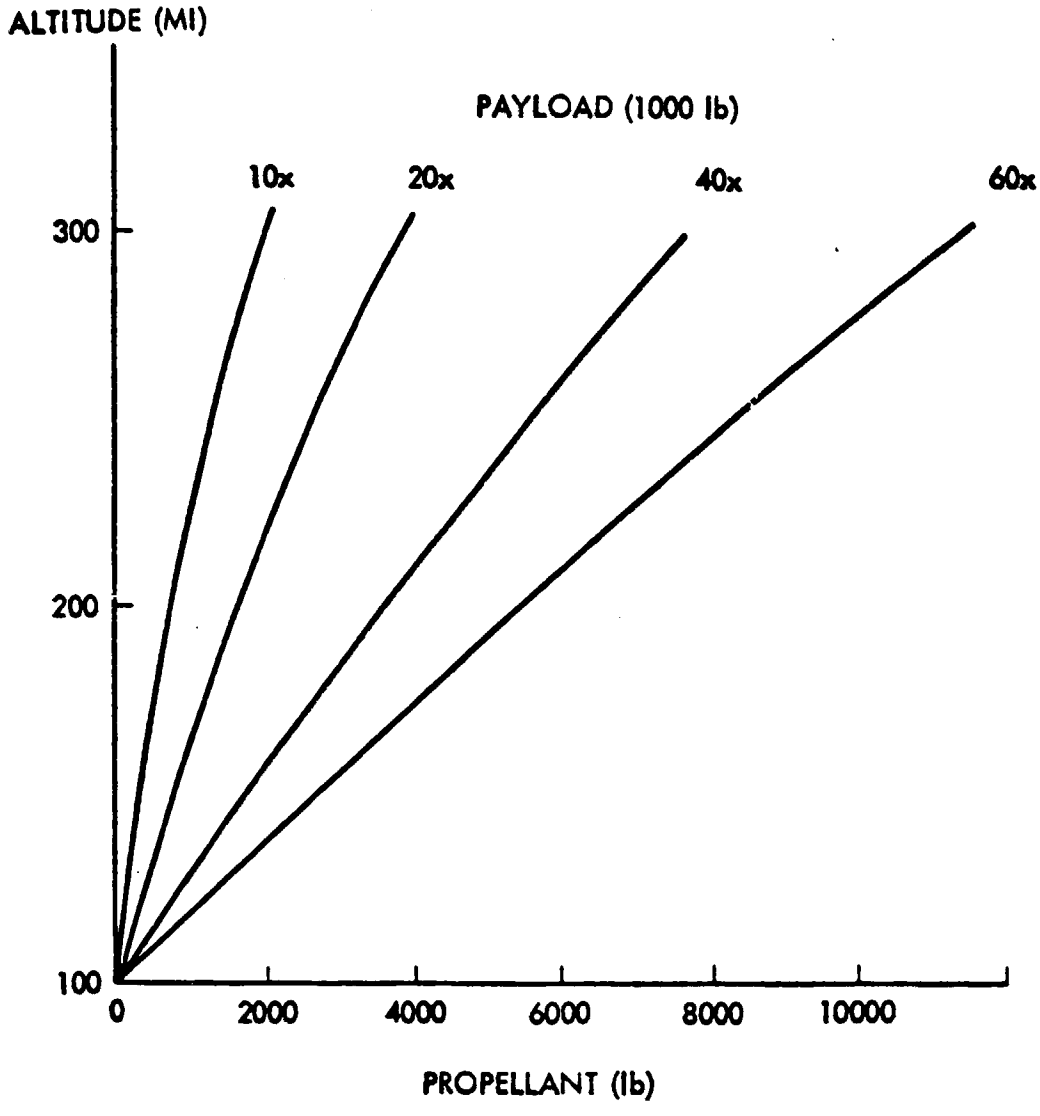

Fig. 5-8 Solid Fuel Requirements

Table 5-1

PROPULSION

Propellant	Specific Impulse (sec)	Desired Thrust (lb.)	Amount Required (kg)	Exhaust	Avail. Engines (lb. thrust)	Technology
Nitrogen (Cold gas)	60	370	5720	N_2	None	Poor
Hydrazine	220	278	1240	N_2, H_2, NH_3	100	Good
					300	Good
Bi-Propellant	320	260	830	CO_2, H_2O, N_2O	25	Good
					200	Good
					800	Good
Oxygen/Hydrogen	454	250	580	H_2, H_2O	15,000	Good
Electric	3000	--	83	Hg,Ce,Ar	0.03	Poor

5.5 Weight

ROM weight estimates of the subsystems were carried our. The results are based partially on direct calculations of component weights and partically on comparisons with the Space Telescope. They are summarized in Table 6-2.

The total dry weight, i.e. excluding propellants and cryogens, is 6574 kg. With 3,395 kg cryogen (sNe and ℓ He), 2700 kg cold gas for ACS, and 1265 kg hydrazine for propulsion (shuttle handoff to operational orbit), we have an all up weight of about 14,000 kg. If hydrazine proves to be a satisfactory choice for ACS propellant, there would be a small weight savings and an all-up weight of about 12,500 kg.

Table 5-2

IRIS WEIGHT BREAKDOWN

ITEM	MASS (KG)	CLASS EST.	CLASS CALC.	COMMENTS
STRUCTURE	1,181		X	GRAPHITE/EPOXY
MIRRORS	640		X	BERYLLIUM 3M DIA.
MIRROR ELECTRONICS	100	X		
SENSOR ASSEMBLY	100	X		
INSULATION	417		X	1.5" MLI*
EQUIPMENT SECTION	200	X		50% SPACE TELESCOPE (ST)
MECHANISMS	230	X		150% ST
SOLAR ARRAYS	243	X		100% ST
BATTERIES	765	X		100% ST
Ne TANKS, 2 LARGE	610		X	21% OF S NEON
Ne TANKS, 2 SMALL	45		X	21% OF S NEON
He TANKS	1,020		X	330% OF L HELIUM
COMMUNICATIONS	84	X		100% ST
DATA MANAGEMENT	163	X		100% ST
POINTING CONTROL (STAR TRACKERS)	29	X		100% ST
ACS - DRY	300		X	E.M. 7752, SCS
CABLES	225	X		SPACE TELESCOPE
COLD GAS (ACS PROPELLANT)	2,700		X	100 90° SLEWS
NEON	3,086		X	PRIMARY OPTICS CRYOGEN
HELIUM	309		X	FOCAL PLANE CRYOGEN
PROPULSION (300 km - 500 km)	1,490		X	HYDRAZINE PROPELLANT
TOTAL	13,937			

*MULTI-LAYER INSULATION

5.6 Cost

Our cost estimate of IRIS is based on the following assumptions:

1. A Space Telescope type of approach to the design, construction, test and operation phases of the experiment.

2. The design, development, component qualification and fabrication of one flight unit, i.e. prototype (full-scale qualification unit not to be required).

3. An SSM type derivative spacecraft. (The SSM subsystems were modified and additional spacecraft development cost estimated.) An SSC type propulsion system, supplemented with a cold gas attitude control system.

4. Sufficient propellant for achieving the 550 km orbit following Shuttle hand-off.

5. A five year operation, at (1/3) of the cost of a Space Telescope operation over the same time interval.

We further assumed for

the focal plane:
1. three discrete detectors;
2. cryogenic focal plane cooling;
3. signal pre-processing;

the optics:
1. two 3m diameter Beryllium primary mirrors, adaptive and cryogenically cooled;
2. two 10 cm diameter secondary mirrors, also Be and cooled;
3. Six high-quality relay mirrors.

Table 5-3

ROM COST ESTIMATES FOR IRIS (1978 $M)

ITEM	COST	COMMENT
SENSOR ASSEMBLY	7.5	
TELESCOPE ASSEMBLY	106.5	SIMILAR TO ST OTA
SUPPORT STRUCTURE AND MECHANISMS	12.0	
PAYLOAD INTEGRATION, TEST AND SUPPORT	11.8	
PAYLOAD	137.8	
SPACECRAFT	66.4	SSM DERIVATIVE
SYSTEMS ENGINEERING, INTEGRATION & TEST	34.5	SIMILAR TO ST
OPERATIONS MISSIONS OP. CENTER	6.5	
5 YEAR OPERATION	17.5	1/3 ST COST RATE
SHUTTLE LAUNCH	26.3	SEE SECTION ON SHUTTLE COST
TECHNOLOGY DEVELOPMENT (CRYOGENICS MIRRORS)	TBD	SEE SECTION 6
PROGRAM TOTAL	289.0 + TECHNOLOGY DEV'T, FACILITIES	

Space Shuttle user costs depend on user category, service level, and weight/volume. Users are divided into standard users and special users. This program falls into the standard user class since it involves civilian U.S. Government payload. The price charged to standard users depends on the estimated costs accrued over a 12 year period. This price will be fixed (except for adjustments due to inflation) for flights during the first three full fiscal years of operation. Beginning with fiscal year 1984 the price may be adjusted annually to ensure that total operating costs are recovered over a 12-year period.

The basic dedicated Shuttle user price is $26.3M 1978 dollars. Escalation for inflation will be computed according to a Bureau of Labor Statistics Index for hourly compensation in the private sector. There is also a sliding scale that adjusts partial loads. The maximum allowable payload length is 60 feet and the maximum allowable payload is 65,000 pounds for a 28.5° inclined orbit. For a payload of 30 foot length weighing no more than 32,500 pounds, the cost factor is .65 which generates a basic cost of $11.7M.

6. Technology Issues

6.1 Cryogenics

6.1.1 Requirements

The cooling requirements for this instrument are summarized below:

Focal Plane	5 - 10° K
Primary Mirror	30 - 40° K
Secondary Mirror	30 - 40° K
Collimated Beam Tube	Cooling requirements to be established

The desired mission lifetime is five years.

The reliability and lifetime capability of closed cycle mechanical refrigerators has clearly not been established for durations of this magnitude so that open cycle coolers utilizing expendable cryogens are the obvious choice for these cooling requirements.

6.1.2 Candidate Cryogens

Of the possible choices of coolants for this application, both solid and liquid cryogens are candidates. The solid cryogens offer advantages over the liquids in terms of density, heat absorption and low g fluid management. In addition, they have been utilized in several orbital programs of long duration (Nimbus 6 and 7, and HEAO instruments).

For the focal plane cooling the following cryogens can meet the temperature requirements:

- o Liquid Helium (≤4° K)
- o Supercritical Helium (5-10° K)
- o Superfluid Helium (1.5-2° K)
- o Solid Hydrogen (8-10° K)

Supercritical fluids have been used rather extensively in orbit for manned missions in connection with fuel cell operations, so that the technology for operation with supercritical helium has been demonstrated and is state of the art. The long mission duration leads to larger, heavier systems than utilized in the past, and therefore a much higher premium is placed on thermal techniques to minimize parasitic heat load to the dewar, in terms of more efficient multilayer insulation and support schemes.

Superfluid helium has not been utilized on orbital missions to date, however, the IRAS Program is well under way and is designed for use with superfluid helium for a one-year orbital mission.

Solid hydrogen has had very little development either on the ground or in space, however, it represents a substantial advantage over helium in terms of weight and volume, and also leads to better temperature stability and simpler fluid management. Its disadvantage is its flammable nature which leads to more extensive safety provisions than for the helium; however, both supercritical hydrogen (Apollo) and liquid hydrogen for engines have been utilized in the space program and safety programs have been successfully developed for it.

If the use of helium is required because of detector temperature requirements (below $\simeq 7^{\circ}$ K attained with solid hydrogen) then reduced weight and volume may be attained with a dual stage approach; for example shielding the helium container with a more efficient but higher temperature cryogen, for example, solid neon or solid hydrogen. These dual stage approaches have been developed and utilized on flight hardware.

It is possible to utilize the cryogen required for cooling of the optics as a shield cryogen for the focal plane, however, more study of the layout and packaging will be required to determine if this is feasible. In the present layout, the substantial distances between the focal plane and primary mirror make this approach infeasible.

A more extensive trade study will be required to determine the optimum combinations of cryogens for this sytem and to choose between single and dual stage approaches.

For the purpose of determining a baseline configuration, a relatively straightforward approach was selected. It was assumed that a single stage helium container is utilized for the detector cooling. The weight and volume of such a system are approximately the same for the three storage modes of helium, i.e. supercritical, superfluid or normal liquid. Other approaches, i.e. dual stage or solid hydrogen lead to lower weights and volume, but somewhat greater complexity.

For cooling of the primary mirrors and the secondary and relay optics to 30 - 40° K, solid cryogens are the clear choice. The candidates for this are

1) Solid neon (13 - 24° K)
2) Solid hydrogen (8 - 13° K)
3) Solid nitrogen (43 - 60° K)

All of these cryogens will allow the optics to run at temperatures higher than indicated, of course. The solid nitrogen represents the best choice in terms of weight, volume, and safety but appears to be marginal because of its operating temperature. If the optics could operate at 45 - 50° K, then solid nitrogen would be the best choice.

For determination of the baseline configuration, a conservative approach was taken, and solid neon was selected as the coolant.

6.1.3 Baseline Cryogenic Systems

In the baseline approach it is assumed that the external structure is radiatively cooled to approximately 200°K by a favorable orientation. Calculations indicate that for the assumed orbit this temperature can be achieved in a relatively straightforward manner. Temperatures lower than this may be achieved by proper shielding and favorable attitude control, and further study will be required to determine the minimum temperatures achievable. This reduced boundary temperature will reduce the heat input to the cryogen tanks, and therefore reduce the cryogen heat loads and boil-off/sublimation rates.

For the focal plane the heat dissipation due to the detectors was assumed to be 10 mw. In addition, 30 mW additional heat load was estimated for the support, lead wires, and radiation coupling with the environment. As previously mentioned, liquid helium was chosen as the cryogen and the mass and volume calculated is applicable to either liquid helium (≈4° K) or superfluid helium (≈2° K). Calculations indicate that helium vapor cooling in combination with the 200° K external swell temperature will essentially eliminate the parasitic heat loads into the dewar itself.

For a 5-year mission duration the calculated mass of liquid helium is 309 KG.

The primary mirrors are 3 meters in diameter and are mounted on fiberglas tube supports and are placed in a cylindrical cavity which acts as a shield against external radiant inputs. This cylindrical shield incorporates a vapor cooled shield utilizing the sublimed neon to reduce heat inputs to the mirror. The external structure runs at 200° K. The cavity containing the primary mirrors is evacuated prior to launch and a vacuum door covers the top of the cavity prior to and after launch. When orbit is attained and the environment is considered sufficiently clean to avoid contamination of the mirror, this door will be rotated out of the way. This mirror is cooled by the large solid neon container off to the side of the mirror. The mirror is assumed to be constructed from Berrylium and the thermal conductivity at 30° K is sufficiently high to make conductive coupling between the coolant and the mirror feasible. Preliminary calculations indicate the heat input to the mirror can be removed through the edge by conduction and that the resulting temperature gradient across the mirror surface will be on the order of 1° K or less. Other packaging concepts are possible, of course, and it may be desirable to store the solid neon in a torus structure located near the base of the mirror for more intimate contact. Although it does not presently appear necessary, heat pipes could be incorporated to provide a more isothermal system.

In the present layout of the system, the primary mirror has a view of the erection tower on which the secondary mirrors are located. It may be necessary to change the configuration of these towers so that the view factor between primary mirror and tower is reduced, which will minimize the heat input to the mirror. Additional analysis is needed in this area to determine the radiant heat input from the towers which is a function of their temperature and geometry. Since it appears necessary to cool a portion of the "collimated beam tubes" for optical reasons, additional cryogen will be required for this cooling, which will interact with the radiant heat load from the towers to the primary mirrors.

Detailed thermal analysis of the mirrors was not performed due to the limited scope of the contract. The heat load to the primary mirrors was based upon heat rate measurements from other programs utilizing scaling

factors to account for differences in surface area and weight. For the purpose of this scaling, it was assumed that the weight of the mirrors established the heat loads attendant with the fiberglas tube support system. The calculations are based upon a fixed support system. It appears that the large, heavy primary mirrors are excellent candidates for a removable support scheme, which provides support during the high g launch loading, but is retracted for the low g orbital operation. Minimal supports would be required for orbital operation of course. The heat loads could be substantially reduced by this means.

For the more conservative, fixed supports the total heat load due to supports, multi-layer insulation and radiant input was estimated to be approximately 1 watt based upon the scaling data.

The cryogen weight associated with this heat load is 1440 KG and its volume is 1050 L. The contaminant and tankage weights associated with the cryogen storage are presented in section 5-5.

The heat input to the secondary mirrors which are assumed to be cooled to 30° K was calculated to be 70 mw, and the coolant for the baseline was assumed to be solid neon.

A summary of the heat loads, cryogen selection and required weight and volume of cryogen is summarized in Table 6-1. Also included in this table are the results for alternate approaches.

Table 6-1

SUMMARY OF CRYOGENIC COOLING SYSTEMS

ASSUMES: 5 YEAR LIFE, 200° K EXTERNAL STRUCTURE TEMPERATURE

COMPONENT	Q, W	T, °K	CRYOGEN	CRYOGEN WT, KG	CRYOGEN VOLUME, L
BASELINE APPROACH					
DETECTORS	0.040	2-4	LIQUID OR SUPERFLUID He	309	2800
PRIMARY MIRROR (300 cm D)	1.0	30	SOLID Ne	1440	1184
SECONDARY MIRROR (10 cm D)	0.070	30	SOLID Ne	103	80
ALTERNATE APPROACHES					
DETECTORS	0.040	8-10	SOLID H_2	13.9	155
PRIMARY MIRROR	1.0	30	SOLID H_2	348	4350
		45	SOLID N_2	627	736
SECONDARY MIRROR	0.070	30	SOLID H_2	24.3	272
		45	SOLID N_2	44	51.6

Direct Detection of Extra-Solar Planets From an Earth Orbit

Technology Requirement:

Long-Life Cryogenic System for IRIS Focal Plane Package

Justification:

Cooling of the focal plane system of IRIS to $\leq$11 K for five years without reservicing on-orbit is required. Several choices of suitable cryogens exist but are unproven for the long mission duration. Careful analysis of the particular needs of this system and the inter-comparison of the level of safety, efficiency, effectiveness and reliability of these choices is necessary. The long mission duration leads to heavier systems than utilized in the past and the possibility of dual systems needs to be investigated.

Objective:

To determine the design requirements and critical technology issues for a focal plane cryogenic system and to develop the necessary technology. Particular emphasis will be laid on helium systems, but small-scale experimental work on hydrogen systems will be initiated.

Approach:

Perform systems trade studies including computer modeling of the system. Perform experimental studies and safety analysis of a solid hydrogen cooler system.

Milestones:

Systems trade studies start + 6 mos; computer modeling start + 6 mos; identify key technology items start + 6 mos; demonstrate solid hydrogen technology, start + 2 yrs. Additional key technology TBD.

Resources:

Years from Go-Ahead						
0	1	2	3	4	5	6
200K		TBD				

Direct Detection of Extra-Solar Planets From an Earth Orbit

Technology Requirement:

Long-Life Cryogenic System for IRIS Telescope Optics

Justification:

Cooling of the optics (two 3 m diameter Primary and two small secondary Be mirrors) to $\leq 30^{\circ}$ K for 5 years without servicing on-orbit is required. No space qualified cryogenic system has yet been operated for longer than seven months, and a design goal for the He system of IRAS is only one year. Several systems options exist but require careful analysis and comparisons (e.g. sNe vs. sH_2) for their levels of safety, economy, effectiveness and reliability. The special geometry and size of the sensor requires thorough thermal modeling. Detailed packaging layouts are required to adequately assess the cooling problems of the sensor.

Objective:

To determine the design requirements and critical technology for the main cryogenic system by detailed thermal analysis and to develop the required technology.

Approach:

Perform systems trade studies followed by detailed computer thermal modeling of the system.

Milestones:

Systems Trade Studies start + 6 mos.
Detailed Computer Modeling start + 6 mos.
Identify Key Technology items start + 2 mos.
Key Technology Demonstration TBD.

Resources:

Years from Go-Ahead					
1	2	3	4	5	6
100K		TBD			

6.2 Structure and Dynamics

6.2.1 System Requirements

As a large, complex, moderately flexible and slowly rotating structure, IRIS is subjected to various torques and stresses (e.g. gravity-gradient, gyroscopic). At the same time, optical & alignment tolerances will be high. These characteristics imply that, even though in principle no feasibility hurdles may exist for the design of such a system, it must be carefully modeled to determine critical technology or design domains.

Precision stabilization of a large spinning spacecraft such as IRIS requires detailed analysis of the effects of vehicle nutation and structural flexibility-induced jitter on star-planet imaging and signal detection. Previous NASA research by Lovell and others has produced methods for active alignment of spacecraft spin axis with the parent star direction using mass-trim systems, reacting wheels, and mass-expulsion systems. The spacecraft considered, however, were not large flexible structures and pointing stability and lifetime requirements were less stringent. Therefore, a detailed system performance analysis for the IRIS sensor system to determine detailed attitude stabilization requirements followed by detailed control system synthesis is needed to ensure that structural flexibility/controller interactions and vibration propagation within the structure are adequately managed. Vibration isolation of point sources such as focal plane coolers* and stability augmentation to reduce vibration propagation might be necessary. No flight experience and very little laboratory data are currently available for such systems, although research is currently being conducted under the DARPA ACOSS Program. To achieve correct IRIS geometry and satisfactory weight along with adequately stiff structural dynamics, some structural optimization using Gr-Ep or other structural materials will be necessary. Gr-Ep structures can be made sufficiently rigid so that vehicle bending modes will be outside the attitude controller bandwidth. Thus stability considerations due to flexible-vehicle interaction modes should not be significant issues. Vibration management will, however, require careful study.

---

*If required

6.2.2 Technical Approach

A detailed tolerances analysis must be performed including the effects of errors in imaging and signal processing and the role of spacecraft nutation, spin rate, vibration propagation, structural flexibility, and attitude control in producing these errors. With this analysis complete, a structural design for IRIS may be performed which attempts to satisfy both weight and dynamics constraints. Structural optimization using software like SPAR can produce a selection of designs which can meet system requirements. The attitude control and stabilization system is then synthesized using a combination of time and frequency-domain techniques to treat both the large-angle maneuvering and the small angle steering problems. Maneuvering is most efficiently performed using mass expulsion and, for example, posi-cast type steering. Small angle stability might be maintained with a combination of low bandwidth mass-trim to align spacecraft optical and principal axes and higher bandwidth momentum storage to compensate disturbance inputs.

Direct Detection of Extra-Solar Planets From an Earth Orbit

Technology Requirement:

Attitude Control and Pointing Stabilization of IRIS

Justification:

The precision pointing, stabilization and attitude control of a large, flexible and rotating structure, to the accuracy required by an IRIS system are demanding problems for which little laboratory data and no flight experience exist. The methods of attack on these problems are well developed, but their application in this case may involve novel approaches and extensive dynamical modeling.

Objective:

To determine a structural design of IRIS satisfying dynamical and weight constraints of the system.

Approach:

Determine detailed pointing control requirements and synthesize, based on these requirements, a preliminary control system which includes structural dynamics interactions from both attitude control and on-board vibration sources. Laboratory test key items in brassboard form.

Milestones:

1. Determination of effects of vehicle dynamics on optical performance.
2. Optimization of structure and dynamical control techniques.

Resources:

$100 K + 6 months for structural analysis

$300 K + 1 year for lab test of key technology

6.3 Mirror Technology

6.3.1 Choice of Material

The IRIS mirror specifications briefly stated are: (1) $\frac{\lambda}{50}$ figure in the IR at 26 μm over the entire mirror surface, (2) $\frac{\lambda}{20}$ in the visible over the center 25% of the mirror area, (3) a constant operating temperature of 30° K, (4) 3-m diameter off-axis f/3 parabola. Several candidate materials were considered for this mirror, among them beryllium, fused silica, and ULE. Beryllium was selected as the preferred material because of its extremely good, low temperature thermal expansion and conductivity properties. The 30° K operating temperature beryllium is many orders of magnitude better in terms of its $\frac{\alpha}{k}$ ratio than either of the candidate glass materials. Other metals could be considered down at this low temperature, but again beryllium is 10-20 times better than Al and five times better than copper at 30° K.

6.3.2 Fabrication

The technology to fabricate large beryllium mirrors has been improving steadily over the past years. Lightweight mirrors of 1 m in diameter have been fabricated. Improvements in beryllium deposition methods will be pursued under an LMSC contract from BMDATC. It appears that large diameter beryllium faceplates can be produced quickly with a very fine surface finish. Considerable technology development is required in this area, however, to ensure that the resulting faceplate can be properly mounted and annealed to relieve any stress formed during the deposition process. If the process does not prove workable at the 3 m diameter, a vapor deposited beryllium or sputtered beryllium coating can be put on an existing beryllium faceplate and the fine grain beryllium material on the face can be polished by conventional means. Problems which have been encountered in the past of orange peel roughness appearing on the beryllium faceplate surface have been conquered by the use of the new deposition and finishing techniques. Since deposition takes place at elevated temperatures, cooling to 30° K will cause some figure distortion. This can be corrected by one of three methods

1) figuring the mirror at elevated temperatures in such a way that it will have the proper figure at 30° K;
2) polishing the Be to the correct figure after deposition; this step is made possible by the small grain size and uniformity of the vapor deposited Be;
3) applying corrective edge moments to control the figure at 30° K.

6.3.3 Coatings

Coatings for the beryllium mirror are required primarily to preserve its surface condition without degradation due to contamination. Bare beryllium has a reflectivity of 95-95% in the IR and approximately 50% in the visible wavelength, which is adequate for this mission.

6.3.4 Cost

Cost of a finished 3 m diameter beryllium mirror is estimated to be the same as for a ULE mirror in a similar configuration. Although the beryllium material is quite expensive, so is ULE, and the majority of the cost comes in the finishing and polishing operations required to produce the mirror figure. If the vapor deposition technique is used, the cost of the mirror is not large but an expensive master must be produced before the faceplate can be manufactured.

Direct Detection of Extra-Solar Planets From an Earth Orbit

Technology Requirement:

Large High-Quality Beryllium Mirrors

Justification:

Currently available mirror manufacturing techniques do not allow production of beryllium mirrors in 3 m diameter using pressed and rolled beryllium sheets. The development of either electron beam vapor deposition or sputtered beryllium techniques to produce a fine grain size beryllium surface either replicating a master or allowing a very smooth polish with a conventional technique is imperative if the high performance beryllium mirror is to be produced.

As an alternative, a copper or aluminum mirror could be produced using conventional techniques, but there would be a corresponding degradation in performance.

Objective:

The objective of this technology development program is to produce a beryllium mirror at 3 m diameter by vapor deposition on a master or by polishing of a sputter beryllium faceplate deposited on a beryllium substrate.

Approach:

The technology being developed by LMSC ongoing programs will be scaled up to the 3 m diameter. The vacuum tanks of this size and the electron beam guns and sputtering machines to perform this scale-up are available once the thickness control, uniformity control and correct parameters are developed.

Milestones:

1. Successful completion of a 1 m diameter beryllium faceplate
2. Successful completion of a 3 m diameter faceplate

Resources:

$200K + 1 year for 1 m demo development

$5M + 3 to 4 years for full-scale mirror

6.4 Beamsplitter

Two major design drivers for the IRIS beamsplitter are the low temperature of operation (30 ^{o}K) and the wide wavelength range of operation (0.5 to 30 m). The material properties of many candidate substrates and coatings are unknown or poorly known for such conditions. Some substrates for example will be waxy or hygroscopic. The operational wavelengths are too short for metal coatings and too long for wire mesh designs. The indexes of refraction at the long wavelength end are unknown for many candidate films.

Possible coating designs are spatially shared $\lambda/4$ stacks and single, non-$\lambda/4$ films, for which computer codes are necessary and also available.

Direct Detection of Extra-Solar Planets From an Earth Orbit

Technology Requirement:

Dielectric Beamsplitter

Justification:

Low operational temperature (30°K) and large wavelength range (~0.5 to ~ 30 μm) of IRIS requires special development of the 50% beamsplitter. particularly careful selection and/or development of substrate material.

Objective:

To determine suitable candidate substrate, develop a workable design build and test dielectric 30 °K beamsplitter for operation between 0.5 and 30 μm.

Approach:

Survey substrate candidates and coating methods. Develop new materials/ methods where necessary. Design, built and test beamsplitter at 30°K.

Resources:

$20-30 K
1-2 years.

6.5 Minor Issues and Summary

A number of technical issues in our sensor design are recognized, whose individual impact on the feasibility, design and performance is either known to be minor or else, if potentially major, for which definitive statements cannot be made within the scope of this study. The issues are problems of either design, or technology development and sometimes of both.

Problems of proper design are: on-orbit calibration systems; on-orbit data processing (relatively small data rate!); contamination and straylight control; figure sensing and wavefront correction; a high-efficiency propulsion and ACS system (e.g. hydrazine; as discussed earlier); spacecraft communication; cooling of the beam collimator tube near the secondary and turning mirrors; tracking and pointing control.

Problems of technology development are: on-orbit mirror cleaning; efficient cooling of the entire beam collimator tubes, if that is afterall found to be necessary; and a cold-gas propulsion system.

Table 6-1 summarizes our assessment of the technical issues which have surfaced in this study, in terms of impact on sensor (feasibility or performance) (parameter a) and state-of-the-art (parameter b). The latter includes an assessment also of the risk and level of effort. The total systems import of an item is given as c = a x b.

None of the issues requires major breakthroughs in design or technology development, but the reliability for operation in space over long periods of time needs to be demonstrated. Furthermore, no issue stands out as the overriding for this sensor. These conclusions are in contrast to the APOTS sensor, for whose full realization one major breakthrough, namely in mirror technology (ripple control) is required and is therefore a very high risk issue. On the other hand, IRIS faces greater number of high-risk issues (c=28 for a "realizable" APOTS 2, 31 for APOTS with perfect ripple control).

Table 6-1

TECHNOLOGY SUMMARY*

	Systems Impact $1 \leq a \leq 3$	State of the Art $1 \leq b \leq 3$	Total Import $1 \leq c = axb \leq 9$
Cryogenics	3	2	6
Dynamical Control	3	2	6
Alignment and Pointing	3	2	6
Beamsplitter	3	2	6
Mirror Manufacturing	2	2	4
Straylight Control	2	2	4
Contamination	2	2	4
Focal Plane	3	1	3
Data Handling	1	1	1
Propulsion	1	1	1
Mirror Figure Control	1	1	1
			Total=42

*Rating System:

a = 1 moderate
2 substantial
3 critical

b = 1 present/low risk
2 advanced/moderate risk
3 much beyond/high risk

7. Schedule

A top-level schedule for an IRIS development program is shown in Fig. 7-1. It has the following characteristics: (i) broad division into preliminary and technology development, definition, design, construction and operational stages; (ii) sufficient time for resolution of critical issues already known or likely to surface in any stage; (iii) ample opportunity for program review. The nine-year development includes 2 1/2 years of detailed definition of concept, system and program. The projected launch date is early 1989, assuming the availability of the launch vehicle.

Schedules for individual technologies are given in Section 6.

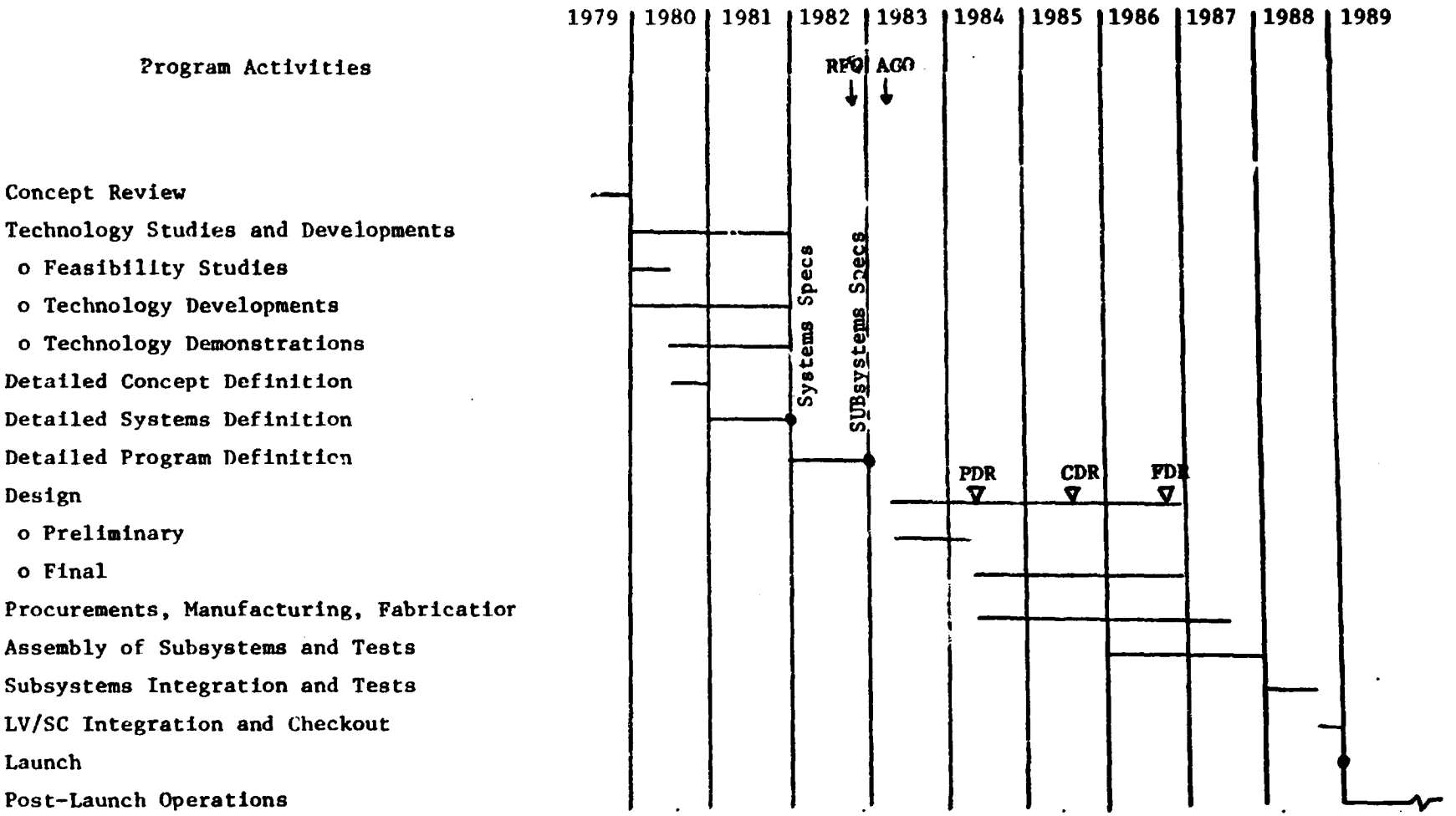

Table 7-1. IRIS Development Program

8. Conclusions

The Stanford concept of a spinning, infrared interferometer (IRIS) for the detection of extra-solar planets from an earth orbit can be realized and operational by the end of this decade, given moderately strong technology advance.

8.1 Performance

Against minimum sky background, IRIS can detect with reasonable confidence in less than one hour a Jupiter-like planet around a Sun-like star at 10 parsecs. In terms of system parameters such as distance, angular separation, etc., the detection space of IRIS has an interesting topology with several sharply defined boundaries. It has been explored only partially and deserves further attention in conjunction with a careful look at the types and distribution of candidate stars. While the problem of detecting multiple planets was not addressed, it should also receive attention in the program downstream. (It was discussed to some extent in NCA2-OR-745-716). Multiple systems after all may be the exception and not the rule.

The observation time of one hour is for a nominal sensor with 3 m diameter apertures and a baseline of 13 m, cryogenically cooled optics and focal plane. It assumes reasonable values for detector efficiency and residual noise. The optical path difference between the two interferometer legs must be controlled to about 90 Å.

Without significant increase in S/N threshold, IRIS can measure temperature and determine if the object is bound to the star: therefore it is unlikely that objects would mistakenly be taken for planets when they are not. Nevertheless, this problem also should receive attention later on.

8.2 Technology

The size, physical complexity and the close optical, thermal and dynamical tolerances of IRIS require advanced technologies. They are: long-life cryogenic systems (optics and focal plane); dynamical control of the large, flexible, slowly rotating structure with varying mass distribution during its life time; large, off-axis, high quality cryogenically figured beryllium mirrors; on-orbit contami-

nation control; stray-light control; closed-loop wavefront sensing and actuating systems.

An important technology challenge derives from the size of the system, e.g. because of its impact on the cryogenic system. The cost, risk and time requirements of some technologies are uncertain - not because fundamental difficulties exist or because methods have not been discovered - but because little previous experience exists with lab or with flight hardware.

8.3 Comparison with Apodized Telescope (APOTS)

Key performance characteristics of APOTS and IRIS are compared in Table 8-1. We distinguish between a now realizable APOTS, APOTS 2, and APOTS 6 which would require a presently unfeasible wavefront control. The detection times differ by a factor of 100.

If built now, IRIS would clearly be the superior system (although it is more expensive): it is faster by orders of magnitude, has a greater range (factor 3) and is more versatile (e.g. can measure temperature).

APOTS performance is limited by diffraction or scattering - i.e. sensor-limited while IRIS is background limited. The capability of measuring temperature is an advantage even if not needed to establish that the discovered object is indeed a planet. Since IRIS does not directly image but reconstructs the object space in a complicated way, there is an apparent disadvantage compared with APOTS. However, APOTS data reduction is also complicated because of the complex spatial structure of the focal plane irradiation, which includes diffracted and scattered light from the parent star as well as stray and background radiation.

Because APOTS is a simpler system than IRIS (dynamically, optically, etc.) there are fewer critical technology areas and the total technical effort for IRIS is greater. This conclusion, however, ignores the one great technology hurdle faced by APOTS - mirror figure - if it is to match IRIS in performance.

Table 8-I

IRIS/APOTS SYSTEMS COMPARISON

	IRIS	APOTS 2
Overall dimensions	-------shuttle bay limits-------	
All-up weight, kg	13,900	6,900
Dry weight	6,600	6,300
Baseline orbit	--550 km, circular, 28.5° inc.--	
Delivery	--shuttle plus orbit transfer by built-in engine--------	
Experiment life	--5 years, no re-servicing------	
Environment	--free-flying, no reservicing---	
ROM Cost, $M	300	200
Development time, yrs	9	
Detection scheme	interferometry, suppress stellar disk	apodization, suppress stellar rings
Detectors	extrinsic photoconductors cryogen cooled(He)	CCD mosaic radiatively cooled
Detection wavelength, μm	26±2	.6±.2
Other wavelengths, μm	18 (temperature) .6 (baseline control)	- -
Mirrors: primary	two 3 m dia., Be, f/3, off-axis parabolic, cryo-figured 30° K	one 3 m dia. ULE, f/5, off-axis, ambient, adaptive
secondary	two 10-30 cm dia., Be, 30° K	one 10-30 cm dia., ULE, ambient
configuration	afocal off-axis Gregorian	focal off-axis Gregorian
wavefront	λ/50	λ/200
Alignment (μm) axial	15	23
lateral	800	1,100
	baseline control 90Å	N.A.
Pointing: accuracy	ST	ST
stability	ST	ST

Table 8-1 (Cont'd)

	IRIS	APOTS 2
Background limited?	Yes	No
Photon rate to Airy disk ($sec^{-1} \mu m^{-1}$)		
planet	1.2×10^6	1.3×10^6
parent star	15	7
minimum zodiacal light	2300	3
Observation time for standard planet	~1 hr	~100 hrs
Range, light years	100	30
Parameter sensitivity:		
Mirror diameter, D	D^{-4}	D^{-5}
Distance to planet d	d^8	d^7
Orbit radius, δ	exponential	δ^{-1}
Magnitude of parent star	exp.	exp.
Angular separation, θ	θ^{-4}	θ^{-5}
Orbit phase	none	yes
Planet verification:		
Means	temperature meas't	N.A.
	------orbit determination-------	
Detection S/N adequate?	yes	yes
Data rate	moderate	moderate
Technology development areas	cryogenic mirror manuf. dynamic control beamsplitter straylinght control	Mirror Manuf. Apodizer Figure Sensing & Actuating
Basic operating limitations	180° uncertainty of planet azimuth (removable)	mirror ripple caused scatter of parent star light
Imaging mode	reconstruction by harmonic analysis	direct imaging

8.4 Recommendations

We suggest the following immediate activities:

(i) A closer look at the scientific objectives of the sensor including a comprehensive analysis of the target space;

(ii) An end-to-end analysis of signal processing and data interpretation, for a baseline design given here or a similar one.

(iii) Advances of the technology in the critical IRIS technology areas, which would be beneficial also for other scheduled or planned infrared space programs.

Appendix A

STELLAR POPULATION OF SOLAR NEIGHBORHOOD

Of the 280 stars within 10 parsecs of the Sun, approximately 85% are components of known or suspected double or multiple systems. Singles would be primary candidates for a planet search, in particular those of solar type because: for want of better knowledge, we are forced to assume the familiar as typical. The solar magnitude at 10 pc, i.e., the absolute visual magnitude, M_v, is 4.83. Single stars within 10 parsecs with visual magnitude less than 5.0 are listed in Table A-1. There are only 17; of these, 13 are main sequence stars. Thus there are a dozen primary candidates for a planetary search - not a large number indeed! In any case, the total number of suitable targets (candidate stars) is relatively small, a few dozen at most. This is an important conclusion for the sensor mission: a small number of suitable targets implies that long or multiple (as are needed for orbit determination) observations of a star are possible within the mission life of the sensor (5 years). It also implies that there is more freedom in choosing the observation period with regarding to achieving best background conditions (i.e., zodiacal light and stray light environment of sensor).

From Fig. 2.3 of the Project Cyclops report, we obtain for an approximate relationship between the volume density of stars and their absolute magnitudes

---

(1) C. W. Allen, Astrophysical Quantities, 3rd Ed., The Athlone Press, 1973

$$\frac{d^2 N}{d M_v \, dV} \approx 7 \times 10^{-4} \exp (0.21 M_v) \qquad \text{(A-1)}$$

($.5 \leq M_v \leq 15$). Since the apparent magnitude, m_v, is related to the absolute magnitude, M_v, and distance d in parsecs

$$m_v = M_v + 2.5 \log d^2 - 5, \qquad \text{(A-2)}$$

we can calculate the approximate number of stars within D and with apparent magnitude less than m_v. We obtain

$$N \simeq 0.015 \, d^{2.55} \exp (0.21 m_v) \qquad \text{(A-3)}$$

which is plotted in Fig. A-1.

Table A-1

SINGLE STARS WITH $m_V < 5$ WITHIN d = 10 pc
(Ref.: Yale University Observatory Catalogue of Bright Stars)

Cat. No.	Name	m_V	Distance (pc)	Type	RA (*)	Dec (*)
77	ζ TUC	4.22	7.5	G2V	20 4	-64 53
98	β HYI	2.79	6.5	G2IV	26 17	-77 15
509	52τ CET	3.50	3.6	G8Vp	1 44 04	-15 56
996	96κ CET	4.82	9.5	G5V	3 19 22	3 22
1008	-	4.26	6.4	G5V	3 19 56	-43 04
1084	18ϵ ERI	3.73	3.3	K2V	3 32 56	-9 28
1136	23δ ERI	3.55	9.2	K0IV	3 43 14	-9 46
1543	1π^3 ORI	3.19	8.0	F6V	4 49 51	6 57
2047	54χ ORI	4.41	9.9	G0V	5 54 23	20 16
4785	8β CVN	4.29	9.3	G0V	12 33 45	41 21
5019	61 VIR	4.75	8.7	G6V	13 18 24	-18 18
5235	8η BOO	2.69	9.8	G0IV	13 54 41	18 24
6927	44χ DRA	3.58	8.3	F7V	18 21 4	72 44
7462	61σ DRA	4.68	5.6	K0S	19 32 21	69 39
7665	δ PAV	3.55	5.9	G8V	20 8 43	66 11
8181	γ PAV	4.22	9.0	F8V	21 26 27	-65 22
8728	24α PSA	1.16	6.9	A3V	22 57 39	-29 37

*Year 2000

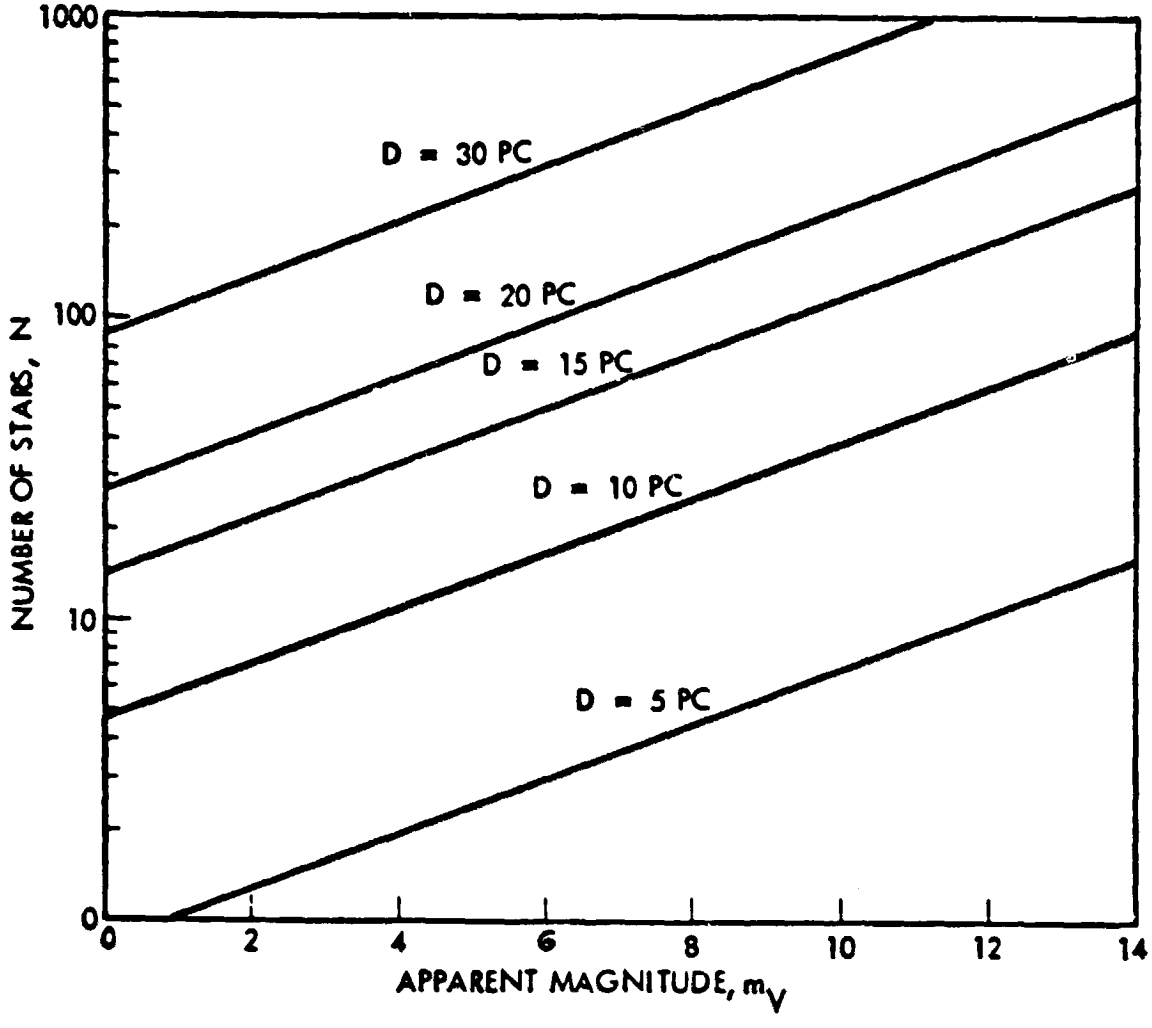

Fig. A-1 Distribution of Stellar Magnitudes Within Distance D (theoretical)

Appendix B

AVERAGE ANGULAR SEPARATION OF STAR AND PLANET

For a random orientation of the planet's orbit relative to us, the planet can be found with equal likelihood anywhere on a surface with radius δ about the parent star, where δ is the orbit radius (orbit assumed circular). The average star-planet separation is therefore given by the average value of the angular distance of points on that sphere from the star-earth line, ρ.

Consult Fig. D-1 for the geometry and definition of parameters. Since

$$\rho \approx \delta \frac{\sin\alpha}{d} \tag{B-1}$$

where d is the star-earth distance, and α the phase angle. We have

$$\rho_{av} = \frac{\int_0^{\pi} \frac{\delta \sin\alpha}{d} \sin\alpha \cdot d\alpha}{\int_0^{\pi} \sin\alpha \cdot d\alpha} \tag{B-2}$$

Thus

$$\rho_{av} = \frac{\pi}{4} \rho_{max} \tag{B-3}$$

where

$$\rho_{max} = \frac{\delta}{d} = 2.5 \mu rad. \tag{B-4}$$

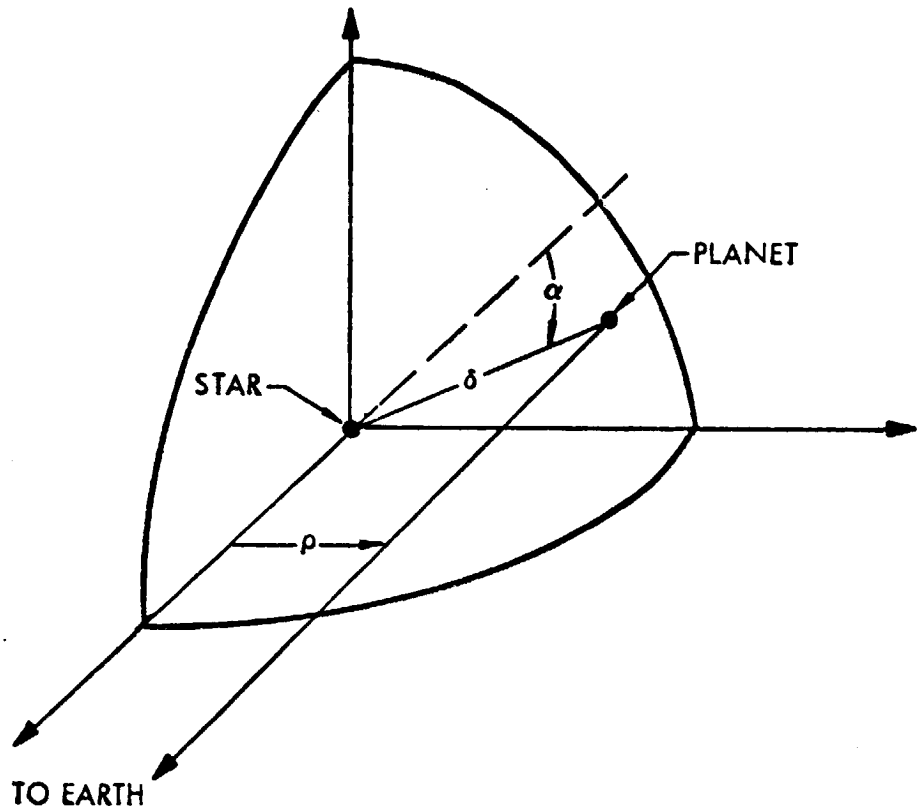

Fig. B-1 Geometry For Calculating Average Planet-Star Separation

Appendix C

OBSERVATION TIME FOR DETECTION USING SEVERAL HARMONICS

If a single sensor channel (harmonic of the planet signal) is used for detection, the observation time is

$$t \propto (S/N)^2_{2m} \left| J_{2m}\left(\frac{2\pi b\theta}{\lambda}\right) \operatorname{sinc}\left(\frac{2\pi m}{Q}\right) \right|^2 \qquad \text{(C-1)}$$

(cf. Sec. 3). The signal to noise value is set by the simultaneous requirements for the probability of false alarm, P_{FA}, and missed detection, P_{MD}. For P_{FA}=0.1 and P_{MD}=0.01, we have $(S/N)_{2m}$=4.3. When two channels are used over the same observation interval, t, the ratio of their respective (S/N)'s is determined as in Fig. 3-6. Here, overall P_{FA}=0.1 and P_{MD}=0.01 are assumed.

To calculate the observation time when two channels are used we note that

$$(S/N)_2 \propto \left| J_2\left(\frac{2\pi b\theta}{\lambda}\right) \right| \sqrt{t} \text{ , etc.} \qquad \text{(C-2)}$$

Thus the ratio of the two (S/N)'s is equal to the ratio of the J's, which only depends on θ. Therefore, the ratio of the (S/N)'s depends only on θ and the respective values of $(S/N)_2$ and $(S/N)_4$ can easily be determined. Once $(S/N)_2$ or $(S/N)_4$ is found, the observation time can be calculated from Equ. (C-1).

A simple approximation of t, given by

$$\frac{1}{t} = \frac{1}{t_2} + \frac{1}{t_4} + \cdots \qquad \text{(C-3)}$$

works quite well, as a comparison of the exact calculations and (C-3) shows (Fig. C-1). (The resulting value of t is somewhat low, but not significantly.) We therefore used this approximation in Sec. (3-6).

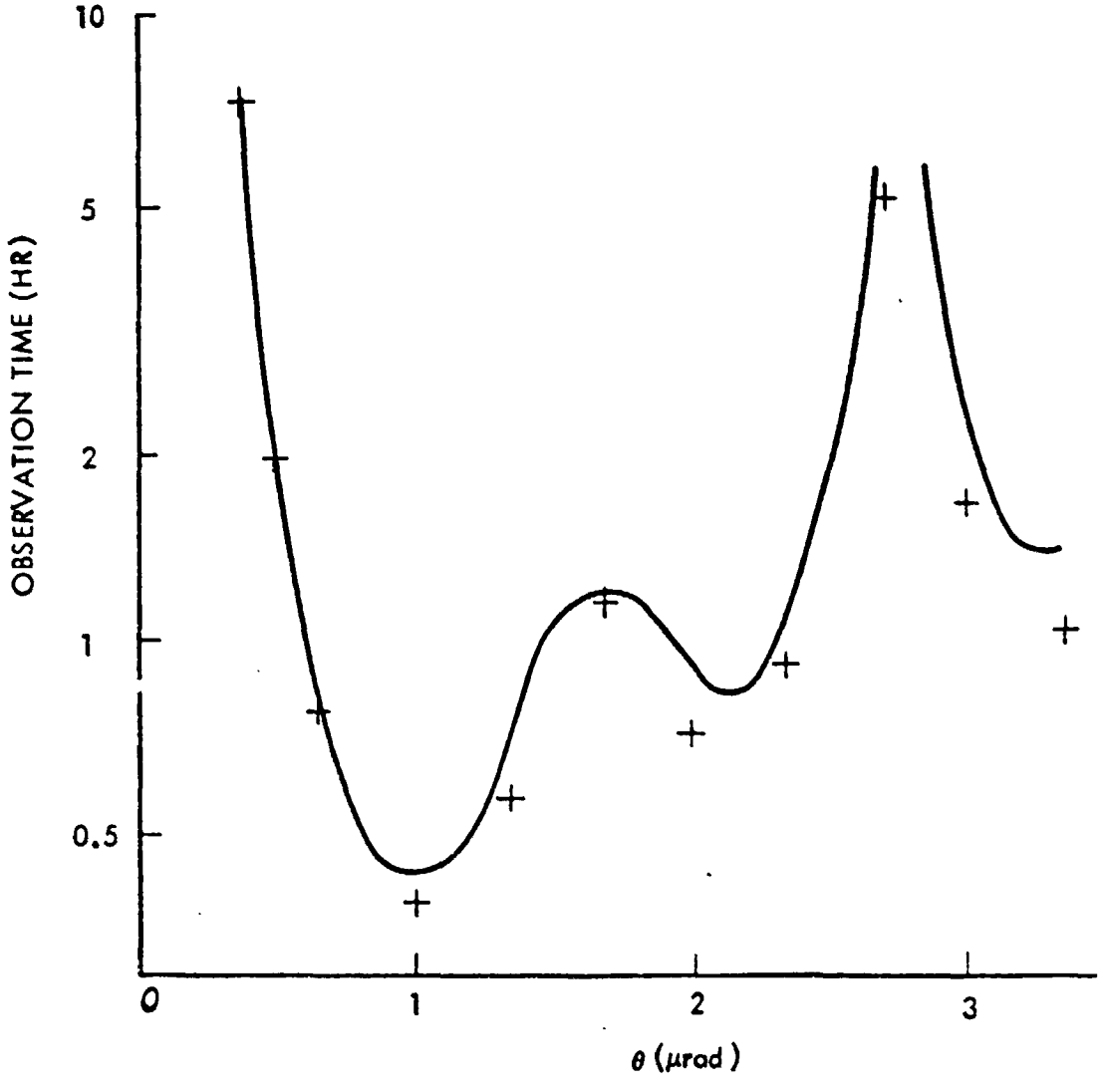

Fig. C-1 On Observation Time using Two Harmonics

· exact results
—— Eq. (C-3)